ICES REPORT 11-29

September 2011

Isogeometric Analysis for topology optimization with a phase field model

by

L. Dede', M.J. Borden, T.J.R. Hughes

The Institute for Computational Engineering and Sciences
The University of Texas at Austin
Austin, Texas 78712

Reference: L. Dede', M.J. Borden, T.J.R. Hughes, "Isogeometric Analysis for topology optimization with a phase field model", ICES REPORT 11-29, The Institute for Computational Engineering and Sciences, The University of Texas at Austin, September 2011.

Isogeometric Analysis for Topology Optimization with a Phase Field Model

Luca Dedè*[†], Michael J. Borden, Thomas J.R. Hughes

20^{th} September 2011

Institute for Computational Engineering and Sciences,
The University of Texas at Austin,
1 University Station C0200, Austin, Texas 78712, USA.

Abstract

We consider a phase field model for the formulation and solution of topology optimization problems in the minimum compliance case. In this model, the optimal topology is obtained as the steady state of the phase transition described by the generalized Cahn–Hilliard equation which naturally embeds the volume constraint on the amount of material available for distribution in the design domain. We reformulate the model as a coupled system and we highlight the dependency of the optimal topologies on dimensionless parameters; also, we discuss the issue of mesh dependency of the solution. We consider Isogeometric Analysis for the spatial approximation which facilitates encapsulating the exactness of the representation of the design domain in the topology optimization and is particularly suitable for the analysis of phase field problems. We demonstrate the validity of the approach and numerical approximation by solving two and three–dimensional topology optimization problems.

Keywords: *Topology optimization; minimum compliance; phase field model; Isogeometric Analysis.*

1 Introduction

In engineering it is often desired to apply some optimization techniques to the design of a structure, component or device. Other than sizing [9, 108] and shape optimization techniques [52, 69, 96], a significant contribution is given by *topology optimization* [10, 12, 14, 84, 86], which represents the fundamental form of optimization; indeed, topology optimization aims at finding the optimal distribution of a material in a design domain such that an objective functional is minimized under certain constraints. The *minimum compliance* case represents the most common topology optimization problem, for which the goal is to generate the globally stiffest structure by distributing only a limited amount of material in the design domain [10, 12]; additionally, another interesting problem consists in generating the lightest structure under stress constraints, see among

---

[*] Current address: SB–MATHICSE–CMCS, École Polytechnique Fédérale de Lausanne, Station 8, CH–1015 Lausanne, Switzerland.

[†] Corresponding author. E-mail: luca.dede@epfl.ch, Tel.: +41 (0)216930318, Fax: +41 (0)216935510.

the others e.g. [23, 36, 75]. Historically, topology optimization has been used principally for structural static problems based on a linear elastic model, but many other cases have also been successfully considered. For example, this is the case for applications in fluid dynamics [1], heat conduction [45], vibration [58], multiphysics [92] and bioengineering [110]; also topology optimization has been used for shell structures [65, 84] and with different material models as in [88] for elastoplastic structures.

In most cases, topology optimization problems are defined in simplified geometries, typically rectangles, representing the design domain. Even if this is a reasonable starting point, in many cases it would be interesting to perform topology optimization for a part or component of a structure for which an initial design already exists. Since it is common practice in engineering to represent geometries with *Computer Aided Design* (CAD) technologies, which are based on NURBS [80] or, more recently, T–splines [89], it is desirable to include the exact representation of the design domain in the topology optimization procedure. However, in current practice, the numerical approximation scheme used for topology optimization, typically the Finite Element Method (e.g. [32, 54, 83]), requires the approximation of the design domain and disconnects the analysis, and hence, the optimization from its geometrical representation.

In general, the capability to embed the CAD geometric representation in the analysis and optimization provides not only accuracy advantages, but also has the potential to considerably improve the efficiency of the overall design procedure. The importance of establishing a suitable link between the optimization and the CAD representation is recognized and discussed in [15] for shape optimization, in particular for shells structures; the authors propose a procedure combining design modeling, structural analysis and optimization, for which these tasks are coordinated by means of a program system named Computer Aided Research Analysis Tool [16] made available to the designer. In [84] shape optimization problems are solved by considering the position of the control points of B–spline [80] as design variables together with adaptive refinement strategies; a similar procedure is extended to topology optimization problems, combining repeated optimization steps with B–spline approximations of the optimal topologies and adaptive refinement. In [69] the relation between CAD and shape parametrization is discussed for shape optimization, especially for fluid dynamics; additionally, in [109] manipulation of the splines is used to generate optimal geometries. Also, in [63] topology optimization problems have been solved by using control points of B–spline curves as design variables in an approach combing shape optimization and hole nucleation.

Isogeometric Analysis, a generalization of Finite Element Analysis for which basis functions are defined by NURBS or T–splines [33, 55], provides the possibility to embed the exact CAD representation of the design domain in topology optimization, in addition to exhibiting several other advantages [8, 34, 39, 46]. Isogeometric Analysis has already been introduced successfully and discussed for shape optimization in [29, 50, 70, 105] and we believe that it also represents a potentially effective numerical approximation method for topology optimization problems. Recently, Isogeometric Analysis has been used in [91] to solve design optimization problems to generate optimal two–dimensional structures by means of a procedure based on trimmed curves; this concept is further extended in [90] for topology optimization problems. In this manner the final optimal structure is represented by NURBS and T–splines and directly linked to the CAD representation without the need of additional postprocessing of the topology optimization result. However, even if this represents a great advantage and ideal situation, the topology optimization results appear to be strongly dependent on the specific approach used to generate the trimmed curves and surfaces. Additionally, B–spline bases are considered in [61] for two–dimensional topology optimization problems. Ideally, a comprehensive design optimization procedure based on Isogeometric Analysis could be used to provide an optimized structure from an initial design domain passing through topology optimization, geometry generation and shape optimization, while maintaining the centrality of the geometry in the overall procedure.

In its original formulation, topology optimization is a distributed and discrete valued problem [12], for which only areas of material and void are allowed without intermediate states. However, this formulation leads to many difficulties both from the analysis and the numerical points of view, and it requires efficient discrete optimizers, see e.g. [98]. The most popular approach to overcome this difficulty is based on the material distribution concept, for which the design variable corresponds to a density function smoothly representing the distribution of the material in the design domain, with intermediate values between the pure material and void states allowed. In this framework a possible approach is the homogenization method [4], for which the macroscopic properties of the material are deduced from the microscopic properties of the porous material represented by the density function; the first numerical approximation for an homogenized material was presented in [10]. However, in this approach solutions appear to have an elevated number of microscopic holes and microstructures which are undesired from a manufacturability point of view, when pure material and void states are required. In order to obtain these kinds of optimal topologies, the intermediate states can be penalized by choosing suitable interpolation schemes for the dependency of macroscopic material properties on the density function; in the case of isotropic materials, the *Solid Isotropic Material Penalization* (SIMP) model is the most successfully used [11, 12, 67, 87]. Typically, topology optimization problems in this approach are solved with suitable constrained optimization techniques and with low–order Finite Element approximation for the density function, often piecewise constant over the elements. However, additional stabilization and filtering techniques need to be introduced at the level of the numerical approximation in order to remove or reduce the well–known mesh dependency and checkerboard phenomena [12, 59] which affect the topology optimization results. Different techniques have been considered to solve topology optimization problems, among these are Evolutionary Structural Optimization (ESO) [111] and Bidirectional ESO methods [113], heuristic procedures based on the identification of regions of material with high and low contributions to the stiffness of the structure; also, other optimization strategies based on the removal of material by the evaluation of topological derivatives have been adopted [71]. However, in general, among the drawbacks of these formulations there is the strong dependence of the optimal solution on the particular optimizer utilized and its settings.

Recently, the use of the level set method [74] has been proposed to solve topology optimization problems [3, 5, 35, 106]. In this approach, the introduction of a level set function, which is associated with the density function, avoids directly tracking the boundaries between the material and the void; the optimal solution is then obtained as the evolution in time of the level set function, for which an optimizer is no longer needed. However, topological changes are uni–directional, in the sense that holes can only be removed in the design domain and inner front creation requires additional numerical techniques [76, 112]; also, similar to other level set methods, repeated reinitializations of the level set function are required while numerically solving the problem.

An alternative approach to topology optimization is provided by the *multiphase* formulation, where the distribution of two phases, representing the material and void, inside the design domain is described by a smooth function which coincides with the density function. The geometrical information associated with the optimal topology is then deduced from the sharp interfaces between the two phases, which are represented by thin layers. The definition of topology optimization problems in a multiphase approach has recently been introduced for design dependent loads in [20] (and [21]), for problems with stress constraints in [23] and for the minimum compliance case in [107, 115]; further extensions are also considered in [102]. The concept at the basis of this approach is that the objective functional to be minimized is penalized by means of additional terms controlling the interfaces and the decomposition of the pure phases, which are typical of multiphase problems [6, 25, 40]. In particular, the introduction of the interface term for penalization allows the definition of a well–posed topology optimization problem [23], and it provides at the discrete level optimal solutions not affected by mesh dependency and checkerboard phenomena. Still the problem is formulated as an optimization one, for which the optimal topology depends in general on the optimizer used.

Further, the topology optimization problem in the multiphase approach can be transformed into a *phase field* problem for which the optimal topology is obtained as the steady state of the phase transition; at the basis of this formulation there is the reinterpretation of the penalized objective functional introduced for the multiphase approach as a total free energy. Traditional phase field models are represented by the Cahn–Hilliard [25, 26, 27] and Cahn–Allen [6] equations, which have been introduced in metallurgy to describe phase segregation in binary alloy systems. More recently, phase field approaches have been successfully considered to provide mathematical models for problems in different disciplines; for example, there are models for crack propagation [18, 66], also with Cahn–Hilliard equation [97], image segmentation [104] and cancer and tumor growth [41, 72]. The role of the phase field approach for topology optimization consists in obtaining separated phases, material and void, divided by thin and sharp interfaces for which the distribution of the material in the design domain is determined by the optimization considerations. In this sense, this resembles the case of the Cahn–Hilliard equation with elastic misfit, for which the distribution of the phases partially takes into account the elastic properties of the materials; see e.g. [42]. In topology optimization, this effect has to assume a leading role, and the distribution of the material depends on the objective function of the topology optimization problem. Phase field models for topology optimization have been considered firstly in [107, 114, 115] for the minimum compliance case, also for multimaterials problems; a nonlinear fourth–order *generalized Cahn–Hilliard* equation is derived and successfully solved for two and three–dimensional problems by using a multigrid algorithm [114, 115] and with an approach which partially decouples the phase and elasticity equations. The mass conservation property of the Cahn–Hilliard equation is conveniently used to naturally take into account the mass/volume constraint associated with the minimum compliance problem. More recently, a similar approach based on the Cahn–Allen equation has been proposed in [102] for shape and topology optimization, even if without the capability to introduce topological changes. In [30] a model based on the diffusion–reaction equation, with analogies with the Cahn–Allen equation, is introduced for minimum compliance problems with an augmented Lagrangian approach to take into account the mass/volume constraint.

Phase field models show many similarities with the level set approach, however, they allow to naturally include hole nucleation in the formulation and avoid reinitializations of level set functions while numerically solving the problem.

In this work we formulate the topology optimization problem for the minimum compliance case by using a phase field approach following [114], since we feel that this kind of formulation provides several advantages. Namely, it has the ability to naturally deal with topological changes, to provide geometrical information, and to completely describe the topology optimization problem at the continuous level, without the necessity of introducing any ad hoc numerical techniques at the discretization stage; also, since the problem of optimization is converted to a phase transition problem, the need to use an optimizer, and hence the dependence of the solution on its settings, is eliminated and replaced with the choice of a suitable time approximation scheme. We rederive the generalized Cahn–Hilliard equation starting from the SIMP and multiphase approaches on the basis of energy considerations, following the usual procedure for the derivation of phase field models, and we highlight the parametric dependency of the problem introduced by the penalization of the objective functional. Also, we rewrite the phase field model as a coupled system of phase and elasticity equations, we provide its dimensionless form, and we characterize it in terms of dimensionless parameters. We discuss the choice of the parameters used to penalize the objective functional and the mesh dependence of the optimal solution, and we extend the continuation method [20, 23, 71], an optimization strategy based on the sequential solution of optimization subproblems, to the phase field case.

For the numerical solution of the topology optimization problem in the phase field approach we consider Isogeometric Analysis for the spatial approximation, since we believe that it provides several benefits for the solution of this kind of problem in analogy with [46, 48] for phase field problems. Firstly, Isogeometric Analysis encapsulates the CAD representation of the design domain in the topology optimization while providing geometric flexibility; also, it ensures robustness, high–order accuracy, and the capability to easily use compactly supported high–order basis functions for the approximation of the nonlinear fourth–order generalized Cahn–Hilliard equation, whose numerical solution necessitates spatially C^1–continuous functions. For the time approximation we use the generalized–α method [31] together with a time–adaptive scheme that allows a very efficient solution of the problem, which, in analogy to other phase field models, exhibits fast and intermittent variations in time. We show the effectiveness of the proposed procedure by solving two and three–dimensional topology optimization problems in design domains defined by NURBS geometries.

This work is organized as follows. In Sec. 2 the SIMP and multiphase approaches for topology optimization in the minimum compliance case are recalled. In Sec. 3 the derivation of the standard Cahn–Hilliard phase field model is recalled in anticipation of the presentation in Sec. 4 of the phase field model for topology optimization. In Sec. 4 the generalized Cahn–Hilliard equation is derived, the coupled system presented, and a dimensional analysis performed in order to highlight the dependency of the problem on dimensionless parameters. In Sec. 5 we present the numerical approximation scheme based on Isogeometric Analysis and the generalized–α method with time adaptivity. In Sec. 6 we discuss the dependency of the optimal solution on the initial distribution of material and the choice of the parameters upon which solutions depend; also, we present the continuation method in the context of the phase field approach. In Sec. 7 we provide and discuss numerical results for two and three–dimensional topology optimization problems. Finally, conclusions are presented in Sec. 8.

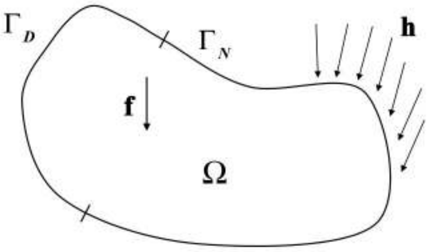

Figure 1: Representation of a two–dimensional design domain Ω, boundaries Γ_D, Γ_N, surface force $\mathbf{h}$ and body force $\mathbf{f}$.

2 Topology Optimization in the Minimum Compliance Case

In this section we introduce the topology optimization problem in the minimum compliance case by means of the SIMP and the multiphase approaches, which represent the basis for the definition of the phase transition model of Sec. 4. Standard notation is used through this work to denote the Sobolev spaces of functions with Lebesgue measurable derivatives and norms; see e.g. [2].

2.1 The SIMP approach

Let us start by introducing a material density function $\rho = \rho(\mathbf{x})$ to represent the distribution of a given material at any generic point $\mathbf{x}$ in a design domain $\Omega \subset \mathbb{R}^d$ of dimension $d = 2, 3$. By convention, $\rho = 1$ indicates the presence of the material, while $\rho = 0$ corresponds to regions of Ω where the material is absent, which we will refer to as void; intermediate states of ρ between 0 and 1 are allowed and indicate regions of "soft" material. Also, we require that $0 \leq \rho \leq 1$, since values outside this range do not correspond to meaningful representations of the material distribution. We adopt a formulation based on the linear elastic theory for small displacements with an isotropic material [54], whose properties are fully described by the symmetric elastic tensor $\mathbb{C}_0$ which depends on the Young's modulus E_0, the Poisson ratio ν_0 and the dimension d of the problem (for $d = 2$, both the plane–stress and plane–strain cases can be considered).

The SIMP approach is based on the concept that the properties of the material depend on the density function ρ for which the elastic tensor $\mathbb{C}(\rho)$ is a function of ρ; in particular, we can write:

$$\mathbb{C}(\rho) = g(\rho)\mathbb{C}_0, \tag{1}$$

with $g(\rho)$ a suitable function introducing the homogenization of the elastic properties depending on the distribution of the material in Ω. The function $g(\rho)$ assumes a crucial role in the definition of the SIMP method, since the quality of the topology optimization results strongly depend on it; we will return on this point later. It follows that the stress tensor is dependent on ρ as:

$$\widetilde{\sigma}(\rho, \mathbf{u}) := \mathbb{C}(\rho)\varepsilon(\mathbf{u}), \tag{2}$$

where $\varepsilon(\mathbf{u})$ is the strain tensor associated to a given displacement $\mathbf{u}$. We observe that the stress tensor $\widetilde{\sigma}(\rho, \mathbf{u})$ is symmetric and linearly dependent on $\mathbf{u}$; the superscript "$\sim$" is used to indicate the dependency on both ρ and $\mathbf{u}$ as independent variables.

The elastic problem in strong form consists in finding the displacement $\mathbf{u}$, for a given material density function ρ, such that:

$$\begin{aligned} & -\nabla \cdot \widetilde{\sigma}(\rho, \mathbf{u}) = \mathbf{f} && \text{in } \Omega, \\ & \mathbf{u} = \mathbf{0} && \text{on } \Gamma_D, \\ & \widetilde{\sigma}(\rho, \mathbf{u})\hat{\mathbf{n}} = \mathbf{h} && \text{on } \Gamma_N, \\ & \rho \text{ given}, \end{aligned} \tag{3}$$

where $\Gamma_D \subset \partial\Omega$ is the Dirichlet partition of the design domain boundary $\partial\Omega$ where the displacement is imposed, while $\Gamma_N := \partial\Omega \backslash \Gamma_D$ is the part of the boundary where the surface force $\mathbf{h}$ is applied (traction or pressure); for the sake of simplicity we assume a null displacement on Γ_D. Also, $\mathbf{f}$ is the body force acting in the domain Ω which we consider independent on ρ. An example is presented in Fig. 1 for a two–dimensional design domain.

Let us introduce, in view of the weak form of the elastic problem (3), the function spaces $\mathcal{V} := \left\{ \mathbf{v} \in \left[H^1(\Omega)\right]^d \ : \ \mathbf{v}|_{\Gamma_D} = \mathbf{0} \right\}$ and $\mathcal{H} := \{\phi \in L^\infty(\Omega) \ : g(\rho) \in L^\infty(\Omega)\}$; moreover, we define the residual $R_{\mathbf{u}}(\mathbf{u};\rho)(\mathbf{v}) \in \mathbb{R}$ such that:

$$R_{\mathbf{u}}(\mathbf{u};\rho)(\mathbf{v}) := \int_\Omega \widetilde{\sigma}(\rho, \mathbf{u}) : \varepsilon(\mathbf{v})\, d\Omega - \int_\Omega \mathbf{f} \cdot \mathbf{v}\, d\Omega - \oint_{\Gamma_N} \mathbf{h} \cdot \mathbf{v}\, d\Gamma_N, \tag{4}$$

where we assume that all the Lebesgue integrals are well defined (this hypothesis holds true for $\rho \in \mathcal{H}$, $\mathbf{u}$, $\mathbf{v} \in \mathcal{V}$, $\mathbf{h} \in \left[L^2(\Gamma_N)\right]^{d-1}$ and $\mathbf{f} \in \left[L^2(\Omega)\right]^d$). Then, the elastic problem (3) in weak form reads, for a given material distribution $\rho \in \mathcal{H}$:

$$\text{find } \mathbf{u} \in \mathcal{V} \ : \ R_{\mathbf{u}}(\mathbf{u};\rho)(\mathbf{v}) = 0 \qquad \forall \mathbf{v} \in \mathcal{V}, \ \rho \in \mathcal{H}. \tag{5}$$

We observe that the displacement $\mathbf{u} \in \mathcal{V}$ solving Eqs. (3) and (5) depends on the prescribed ρ, for which $\mathbf{u} = \mathbf{u}(\rho)$. In this manner the stress tensor of Eq. (2) associated to the solution of Eq. (5) reads:

$$\sigma(\rho) := \widetilde{\sigma}(\rho, \mathbf{u}(\rho)) = \mathbb{C}(\rho)\varepsilon(\mathbf{u}(\rho)). \tag{6}$$

We introduce the compliance energy of the system (5), say $J_E(\rho)$, as:

$$J_E(\rho) := \int_\Omega \psi_E(\rho)\, d\Omega, \tag{7}$$

where $\psi_E(\rho)$ is the strain energy function:

$$\psi_E(\rho) := \widetilde{\psi}_E(\rho, \mathbf{u}(\rho)), \tag{8}$$

with:

$$\widetilde{\psi}_E(\rho, \mathbf{u}) := \widetilde{\sigma}(\rho, \mathbf{u}) : \varepsilon(\mathbf{u}). \tag{9}$$

We observe that the standard definition of the strain energy involves a factor of 1/2 which is neglected to maintain the formulation consistent with the typical one of the topology optimization framework. Also, we notice that following from Eqs. (5) and (7),

$J_E(\rho) \equiv \int_\Omega \mathbf{f} \cdot \mathbf{u}(\rho)\, d\Omega + \oint_{\Gamma_N} \mathbf{h} \cdot \mathbf{u}(\rho)\, d\Gamma_N$. Moreover, Eq. (7) can equivalently be written as $J_E(\rho) = \widetilde{J}_E(\rho, \mathbf{u}(\rho))$, where from Eq. (9):

$$\widetilde{J}_E(\rho, \mathbf{u}) := \int_\Omega \widetilde{\psi}_E(\rho, \mathbf{u})\, d\Omega. \tag{10}$$

In order to introduce the topology optimization problem in the minimum compliance case, we recall that only a limited amount of material can be used, which means that only a limited area/volume of Ω, say $V < |\Omega|$, can be covered by the material, with V defined as:

$$V := \int_\Omega \rho\, d\Omega. \tag{11}$$

In this sense, the topology optimization problem is constrained and the space of admissible controls, say $\mathcal{H}_{ad} \subset \mathcal{H}$, in which we look for the optimal solution ρ^* is defined as $\mathcal{H}_{ad} := \left\{ \phi \in \mathcal{H} \;:\; 0 \leq \phi \leq 1 \text{ and } \int_\Omega \phi = V \right\}$ [1]. Then, the problem of topology optimization in the minimum compliance case corresponds to

$$\text{find } \rho^* \in \mathcal{H}_{ad} \;:\; \rho^* = \operatorname{argmin}\,(\, J_E(\rho)\,) \tag{12}$$

where $J_E(\rho)$ is the compliance energy (7) of the elastic system (5).

We recall that the elastic properties of the material are introduced in the topology optimization problem by means of the interpolation function $g(\rho)$ of Eq. (1). In general, the topology optimization procedure allows "soft" regions of material in the design domain, since ρ can assume intermediate values between 0 (void) and 1 (material). However, these situations, even if consistent with the mathematical formulation, are in general not desired as output of the optimization problem. Indeed, the goal is to distribute a given material with its full elastic properties for which the desired values of ρ are possibly only 0 (void) and 1 (material). In order to reduce or avoid these situations, the function $g(\rho)$ of Eq. (1) plays a crucial role. In the material interpolation formulation, this function is typically chosen such that intermediate distributions of material correspond to a material with poor stiffness properties; in this manner, due to the area/volume constraint, the material is located to minimize the compliance energy of the system. A typical choice for $g(\rho)$ is based on the SIMP model, for which:

$$g(\rho) = \rho^P, \tag{13}$$

with $P \geq \max\left\{ \frac{2}{1-\nu_0}, \frac{4}{1+\nu_0} \right\}$ if $d = 2$ or $P \geq \max\left\{ 15\frac{1-\nu_0}{7-5\nu_0}, \frac{3}{2}\frac{1-\nu_0}{1-2\nu_0} \right\}$ if $d = 3$; the condition on the power P is to guarantee that the interpolation model represents a material model [11, 12, 67]. Typically, since materials with $\nu_0 = 1/3$ are often considered, the power is chosen such that $P \geq 3$ for both $d = 2, 3$; also this value is reasonable even when a minimum value for ρ, say $\rho_{min} > 0$, is introduced. We observe that other choices of $g(\rho)$ can be made, among these are rational functions [99] and B-splines [77], which can be useful for vibration problems; see [12] for a wider discussion.

---

[1] In the standard definition of topology optimization problems in the minimum compliance case, the area/volume constraint is an inequality one, $\int_\Omega \rho\, d\Omega \leq V$; see e.g. [12]. However, typically, the optimal solution ρ^* is such that $V^* := \int_\Omega \rho^*\, d\Omega \equiv V$ in order to maximize the stiffness of the structure.

The continuous topology optimization problem (12) does not admit, in general, the existence of optimal solutions as pointed out and discussed in [12, 60]; moreover, the uniqueness of the solution is also an issue, since multiple minima can be detected due to the non–convex nature of the problem. However, even if in general ill–posed [60, 64, 95], the topology optimization problem is discretized and then solved numerically. Typically, see e.g. [11, 12, 99], low order Finite Element approximations are used to approximate the density function ρ, even if other choices are possible (see [45] for a Finite Volume Method). Then, the problem is solved by means of a suitable optimization method; in this sense, the Method of Moving Asymptotes (MMA) represents one of the most effective optimizers for the solution of topology optimization problems [100, 101]. The fact that the continuous problem is ill–posed reflects on the numerical solution, even if the discrete problem admits the existence of optimal solutions. This is revealed by the so called mesh dependency effect, for which different optimal solutions are obtained with different discretizations of the problem, specifically for different Finite Element meshes. There are several techniques to contain or eliminate this effect, which are introduced as global or local constraints; the most used ones are [12, 95]: local constraints on the density gradient [79], local density and sensitivity filters [19, 79, 93, 94], global control of the minimum length scale [49, 81], perimeter control or limitation, for which a global constraint:

$$\int_\Omega \nabla\rho \cdot \nabla\rho \, d\Omega \leq P_L, \tag{14}$$

with $P_L > 0$, is imposed [78]. The imposition of a perimeter constraint limits the number of holes that a solution could exhibit. In practice, the constraint (14) is introduced to make the topology optimization problem well posed, as shown in [7] for the continuous case. An alternative approach to the inequality constraint on the perimeter has been proposed in [51] and consists in perturbing the objective functional (7) with a smooth penalty term for the perimeter P_L.

Another undesired, but common, feature that optimal topologies can exhibit is the so called checkerboard phenomenon, which indicates a numerical solution with patterns of alternate 0–1 values (void–material) [12, 95]. As discussed in [59], this represents a form of numerical instability associated with the approximation of the topology optimization problem, which is a nonlinear mixed variational problem in the independent density and displacement variables. Similarly to the case of linear mixed problems [22], stability issues could arise at the discrete level even if the continuous problem is well posed. Even if a comprehensive analysis of the stability properties has not been performed due to the nonlinear nature of the problem, it has been shown in [59] for some particular topology optimization problems, that using suitable pairs of Finite Element spaces for the density and displacement variables eliminates the checkerboard issues [2]. In general, as pointed out in [12], any of the numerical techniques introduced to limit the mesh dependency effect could be effectively used to avoid this phenomenon.

As a final remark, we observe that in order to properly solve the topology optimization problem (12) in the SIMP approach, it is necessary to introduce additional numerical techniques, which in general depend on the discretization chosen, with respect to the original continuous formulation of the problem; also a suitable constrained optimizer needs to be used.

---

[2] Other possibilities are the introduction of an augmented Lagrangian functional or the postprocessing filtering of the numerical solution.

2.2 The multiphase approach

In order to introduce the topology optimization problem in the multiphase approach, we observe that the distribution of the phases, material and void, inside the design domain Ω is represented by the material density function ρ. Also, we define the parameters $\boldsymbol{\mu} = (\gamma, \lambda) \in \mathcal{D}$, with γ and λ positive and the parameter set $\mathcal{D} \subset \mathbb{R}^2$, in order to introduce a parametrization on the topology optimization problem. We define the following penalized objective functional which depends on the parameters $\boldsymbol{\mu} \in \mathcal{D}$:

$$J(\rho; \boldsymbol{\mu}) := \int_\Omega \psi(\rho; \boldsymbol{\mu})\, d\Omega, \tag{15}$$

with the function $\psi(\rho; \boldsymbol{\mu})$ defined as:

$$\psi(\rho; \boldsymbol{\mu}) := \gamma \psi_E(\rho) + E_0 \left(\psi_B(\rho) + \lambda \psi_I(\rho) \right), \tag{16}$$

where the strain energy function $\psi_E(\rho)$ is defined in Eq. (8), $\psi_B(\rho)$ is a suitable bulk energy function and $\psi_I(\rho)$ is the interface energy function:

$$\psi_I(\rho) := \frac{1}{2} \nabla\rho \cdot \nabla\rho. \tag{17}$$

The constant E_0 is introduced to ensure that all the terms in Eq. (16) have the dimension of an energy density [3]. The objective functional $J(\rho; \boldsymbol{\mu})$ (15) can be rewritten as:

$$J(\rho; \boldsymbol{\mu}) = J_E(\rho; \gamma) + J_B(\rho; E_0) + J_I(\rho; \lambda; E_0), \tag{18}$$

where:

$$J_E(\rho; \gamma) := \gamma \int_\Omega \psi_E(\rho)\, d\Omega, \tag{19}$$

$$J_B(\rho; E_0) := E_0 \int_\Omega \psi_B(\rho)\, d\Omega, \tag{20}$$

$$J_I(\rho; \lambda; E_0) := E_0\, \lambda \int_\Omega \psi_I(\rho)\, d\Omega. \tag{21}$$

We observe that the objective functional (15) is penalized in the sense that two terms proportional to $\psi_B(\rho)$ and $\psi_I(\rho)$ are added to the strain energy function $\psi_E(\rho)$. In particular, the bulk energy $\psi_B(\rho)$ is a non–convex smooth function chosen in the form of a double–well in the pure phases $\rho = 0$ and $\rho = 1$, for example, as $\psi_B(\rho) = \rho(1-\rho)$ or $\psi_B(\rho) = \rho^2(1-\rho)^2$ [23]; in this manner, the values assumed by $\psi_B(\rho)$ for intermediate values of ρ are larger than for the pure phases, which are preferred in the optimization context. Also, further penalization terms can be added to $\psi_B(\rho)$ in proximity of the pure phases $\rho = 0$ and 1 in order to remove the inequality constraints $0 \leq \rho \leq 1$ from the formulation of the optimization problem; a possibility is to consider $\psi_B(\rho)$ a logarithm–type function with singularities in the pure phases. The interface energy function $\psi_I(\rho)$ plays an important role in the penalization of the compliance energy, since it represents a measure of the perimeter of the interfaces between the phases; in this sense, it is the relaxed version of the global perimeter limitation constraint (14) often introduced in the SIMP method to remove the mesh dependency effect in the discretized problem.

---

[3] Eventually, the constant E_0 could be included among the parameters $\boldsymbol{\mu} \in \mathcal{D}$; however, the parametric dependence of the objective functional $J(\rho; \boldsymbol{\mu})$ (15) would still be completely represented by only two parameters by means of suitable scalings.

Also, this term assumes the role of controlling the thickness of the interfaces through the parameter λ and thus the capability to capture the geometrical informations from the optimal topology.

Finally, we notice that the objective functional (15) can be rewritten as $J(\rho;\boldsymbol{\mu}) = \widetilde{J}(\rho,\mathbf{u}(\rho);\boldsymbol{\mu})$, where:

$$\widetilde{J}(\rho,\mathbf{u};\boldsymbol{\mu}) := \int_\Omega \widetilde{\psi}(\rho,\mathbf{u};\boldsymbol{\mu})\, d\Omega, \tag{22}$$

with, following from Eq. (9):

$$\widetilde{\psi}(\rho,\mathbf{u};\boldsymbol{\mu}) := \gamma\widetilde{\psi}_E(\rho,\mathbf{u}) + E_0\left(\psi_B(\rho) + \lambda\psi_I(\rho)\right). \tag{23}$$

Similarly to Eqs. (18)–(21) we can write:

$$\widetilde{J}(\rho,\mathbf{u};\boldsymbol{\mu}) = \widetilde{J}_E(\rho,\mathbf{u};\gamma) + J_B(\rho;E_0) + J(\rho;\lambda;E_0), \tag{24}$$

with:

$$\widetilde{J}_E(\rho,\mathbf{u};\gamma) := \gamma\int_\Omega \widetilde{\psi}_E(\rho,\mathbf{u})\, d\Omega. \tag{25}$$

If we consider the penalized objective functional $J(\rho;\boldsymbol{\mu})$ (15) with the bulk energy function $\psi_B(\rho)$ embedding the penalization terms for the inequality constrains $0 \leq \rho \leq 1$, we can take the space of admissible controls as $\mathcal{H}_{ad} = \left\{\phi \in \mathcal{H} \ :\ \int_\Omega \phi = V\right\}$, where only the area/volume constraint is explicitly imposed and $\mathcal{H} = \{\phi \in L^\infty(\Omega) \cap H^1(\Omega) \ :\ g(\phi) \in L^\infty(\Omega)\}$; the extra regularity of $\mathcal{H}$ with respect to the SIMP approach is due to the presence of the interface energy $\psi_I(\rho)$ in the formulation. The topology optimization problem in the multiphase approach corresponds to:

$$\text{find } \rho^* \in \mathcal{H}_{ad} \ :\ \rho^* = \operatorname{argmin}\left(\, J(\rho;\boldsymbol{\mu})\,\right), \tag{26}$$

for any given parameter $\boldsymbol{\mu} \in \mathcal{D}$. We observe that the optimal distribution of material in the design domain is $\rho^* = \rho^*(\mathrm{x};\boldsymbol{\mu})$ in the sense that it depends on the parametrization introduced in the penalized objective functional (15).

The parameters $\boldsymbol{\mu} = (\gamma,\lambda) \in \mathcal{D}$ in Eq. (16) play a crucial role in the optimization problem, since they regulate the balance of the different terms contributing to the penalized objective functional $J(\rho;\boldsymbol{\mu})$. For example, if γ is very large, the optimization problem assumes a similar behavior to the SIMP approach. Conversely, if $\gamma = 0$, then the optimal result ρ^* is dominated by the bulk and interfaces terms only; this last case corresponds to a pure multiphase problem, where the total free energy of the system is minimized [26, 40] (see Sec. 3 for the Cahn–Hilliard equations).

Remark 2.1 *A third positive parameter, say $\kappa \in \mathbb{R}$, can be added to the parameter vector $\boldsymbol{\mu} \in \mathcal{D}$, such that $\boldsymbol{\mu}_\kappa := (\gamma,\lambda,\kappa) \in \mathcal{D}_\kappa$, with $\mathcal{D}_\kappa \subset \mathbb{R}^3$. In this case, the penalized objective functional (15) is redefined as:*

$$J_\kappa(\rho;\boldsymbol{\mu}_\kappa) := \int_\Omega \psi_\kappa(\rho;\boldsymbol{\mu}_\kappa)\, d\Omega, \tag{27}$$

with the function $\psi_\kappa(\rho;\boldsymbol{\mu}_\kappa)$:

$$\psi_\kappa(\rho;\boldsymbol{\mu}_\kappa) := \gamma\psi_E(\rho) + E_0\left(\frac{1}{k}\psi_B(\rho) + k\lambda\psi_I(\rho)\right). \tag{28}$$

Then, the formulation of the topology optimization problem follows similarly to the previous case. The role of κ is twofold. Firstly, it ensures that the penalized objective functional is convex for κ "sufficiently" large and the topology optimization problem (26) is well–posed, as shown in [23] for a minimum weight topology optimization problem with stress constraints in a relaxed approach. Secondly, it ensures that the optimal topology converges to the pure phases 0 *and* 1 *for $\kappa \to 0$ [23], according to the properties of Γ–convergence (see e.g. [68]) for functionals with interface terms [20]. On this basis the parameter κ introduces the possibility to solve the topology optimization problem (26) by means of the continuation method [12, 20, 23, 71]. In this procedure, the optimal topology ρ^* is obtained as the last step of a sequence of minimizers of locally convex (or quasi–convex) optimization problems parametrized for decreasing values of κ and initialized with the optimal solution of the previous step; this means that a non–convex topology optimization problem without interface term, which corresponds to the ideal formulation, is obtained as the limit for $\kappa \to 0$.*

Finally, we observe that the topology optimization problem in the multiphase approach is completely defined at the continuous level and, eventually, for suitable choices of the parameters, also well–posed. This is not the case of the SIMP formulation, which is in general ill–posed at the continuous level and it requires the introduction of additional numerical techniques at the discrete level. However, a non–convex optimizer is still required to solve the topology optimization problem in the multiphase context.

3 Phase Field Model: the Cahn–Hilliard Equation

In Sec. 2.2 we have considered the topology optimization problem as a multiphase approach for which a penalized objective functional is minimized; the formulation is however still set in an optimal control context, for which an optimization problem needs to be solved to find ρ^*. However, the penalized objective functional can be interpreted as a total free energy and the topology optimization problem recast in a phase transition setting. Indeed, in this case, the evolution of the phases is such that an energy is minimized in time with respect to the initial configuration. In this section we provide the derivation of the standard Cahn–Hilliard phase field model [25, 26, 27, 28] and we highlight its properties in view of the phase field model for topology optimization in Sec. 4. For further details in the analysis of the Cahn–Hilliard equation we refer the interested reader to [24, 37, 38, 40, 85], while e.g. to [37, 46, 103] for its numerical solution.

Let us consider a two phase problem, for which the phase transition is described by the variable $\rho = \rho(t, \mathbf{x})$, which corresponds to the concentration of one of the phases in the domain Ω (the other one is obtained as $1 - \rho$ in the 0–1 binary representation). The total free energy (Ginzburg–Landau free energy), which we indicate with $F(\rho; \lambda)$ [26, 27, 40], is expressed in the case of interest as:

$$F(\rho; \lambda) := \int_\Omega \psi_F(\rho; \lambda)\, d\Omega, \tag{29}$$

with the total free energy function $\psi_F(\rho; \lambda)$ defined as:

$$\psi_F(\rho; \lambda) := C_0 \left(\psi_B(\rho) + \lambda \psi_I(\rho) \right), \tag{30}$$

for a positive parameter $\lambda \in \mathcal{D} \subset \mathbb{R}$ and the bulk and interface energies given in Sec. 2.2; the parameter C_0 is introduced to ensures that the function $\psi_F(\rho; \lambda)$ assumes the dimension of an energy density. Typically, a double–well logarithm or quartic function is chosen for $\psi_B(\rho)$ [26, 38, 40, 103], even if other type of functions can be conveniently used.

The definition of the phase transition model is based on the concept of gradient flow $\operatorname{grad} F(\rho,\lambda)$ of the functional $F(\rho;\lambda)$ in the norm of a Hilbert space $\mathcal{Z}$ [28, 40], for which the corresponding equation in strong form reads:

$$\frac{\partial\rho}{\partial t} = -\operatorname{grad} F(\rho;\lambda) \qquad \text{in } \Omega,\ \forall t \in [0,T), \tag{31}$$

with $\rho = \rho_0$ for $t = 0$ in Ω. Depending on the choice of the function space $\mathcal{Z}$, different phase transition models can be obtained; if $\mathcal{Z} = \left\{\varphi \in \left(H^1(\Omega)\right)' \,:\, \langle\varphi, 1\rangle = 0\right\}$ [40], the Cahn–Hilliard gradient flow and the corresponding equation are obtained [25, 26, 27], otherwise, if $\mathcal{Z} = L^2(\Omega)$, the Cahn–Allen equation is derived [6]. In particular, in the Cahn–Hilliard case, the gradient flow $\operatorname{grad} F(\rho,\lambda)$ reads:

$$\operatorname{grad} F(\rho;\lambda) = -\nabla\cdot\left(M(\rho)\nabla z_F(\rho;\lambda)\right), \tag{32}$$

where $M(\rho) \geq 0$ is a sufficiently regular function called the mobility, which is typically a constant M_0 or degenerate $M(\rho) = M_0\rho(1-\rho)$, and $z_F(\rho;\lambda)$ is the potential associated to the total free energy function $\psi_F(\rho;\lambda)$; in the Cahn–Allen case, the gradient flow would read $\operatorname{grad} F(\rho;\lambda) = M(\rho) z_F(\rho;\lambda)$. The potential $z_F(\rho;\lambda)$, which we introduce for the sake of simplicity, depends specifically on the choice made for the functional (29) and in this case is obtained as the Gâteaux derivative in $L^2(\Omega)$ of the total free energy (29):

$$\left(z_F(\rho;\lambda),\, \phi\right)_{L^2(\Omega)} = \frac{1}{C_0}\frac{dF}{d\rho}(\rho;\lambda)[\phi] \qquad \forall\phi \in H^1(\Omega), \tag{33}$$

for some $\lambda \in \mathcal{D}$; if further we assume that the boundary condition $\nabla\rho\cdot\hat{\mathbf{n}} = 0$ is imposed on $\partial\Omega$, the potential $z_F(\rho;\lambda)$ simply reads:

$$z_F(\rho;\lambda) = z_B(\rho) + \lambda z_I(\rho), \tag{34}$$

where:

$$z_B(\rho) := \frac{d\psi_B}{d\rho}(\rho), \tag{35}$$

$$z_I(\rho) := -\Delta\rho, \tag{36}$$

for ρ sufficiently regular.

A standard formulation of the Cahn–Hilliard equation in strong form is:

$$\begin{aligned}
&\frac{\partial\rho}{\partial t} = \nabla\cdot\left(M(\rho)\nabla z_F(\rho;\lambda)\right) && \text{in } \Omega,\ \forall t \in [0,T),\\
&M(\rho)\nabla z_F(\rho;\lambda)\cdot\hat{\mathbf{n}} = 0 && \text{on } \partial\Omega,\ \forall t \in [0,T),\\
&\nabla\rho\cdot\hat{\mathbf{n}} = 0 && \text{on } \partial\Omega,\ \forall t \in [0,T),\\
&\rho = \rho_0, && \text{in } \Omega,\ t = 0,
\end{aligned} \tag{37}$$

for some $\lambda \in \mathcal{D}$. We define the function space $\mathcal{H} := \left\{\phi \in H^2(\Omega) \,:\, \nabla\phi\cdot\hat{\mathbf{n}} = 0\right\}$. Let us assume that $\rho \in C^1\left([0,T);\mathcal{H}\right)$ and so $\frac{\partial\rho}{\partial t} \in \mathcal{C}^0\left([0,T);\mathcal{H}\right)$. That is, ρ is a C^1–continuous mapping from the time interval $[0,T)$ into $\mathcal{H}$ and $\frac{\partial\rho}{\partial t}$ is a C^0–continuous mapping from

$[0,T)$ into $\mathcal{H}$. Consequently, for each $t \in [0,T)$, $\rho \in \mathcal{H}$ and $\dfrac{\partial \rho}{\partial t} \in \mathcal{H}$. From Eq. (37), for each $t \in [0,T)$, the residual $R_{CH}(\rho;\boldsymbol{\mu})(\phi) \in \mathbb{R}$ is given by:

$$R_{CH}(\rho;\lambda)(\phi) := \int_\Omega \frac{\partial \rho}{\partial t}\phi \, d\Omega + \int_\Omega M(\rho)\nabla z_F(\rho;\lambda)\cdot\nabla\phi\, d\Omega. \tag{38}$$

Then, the Cahn–Hilliard equation in weak form reads:

$$\begin{aligned} &\text{find } \rho \in \mathcal{W} \ : \ R_{CH}(\rho;\lambda)(\phi) = 0 \qquad \forall \phi \in \mathcal{H}, \ \forall t \in [0,T), \\ &\text{with } \rho = \rho_0 \qquad \text{in } \Omega, \ t = 0, \end{aligned} \tag{39}$$

for some $\lambda \in \mathcal{D}$. The Cahn–Hilliard equation (39) (or Eq. (37)) is endowed with the following properties:

- Its solution ρ exists and is unique for the case of constant mobility as shown in [85] for problems in dimensions $d = 1, 2, 3$ under suitable hypothesis for the bulk function $\psi_B(\rho)$ including its smoothness; existence of solutions is discussed in [38] for the case of degenerate mobility.

- It is mass conservative in the sense that the area/volume covered by the phases in Ω is constant in time; indeed, by using the definition (11), we can easily deduce from Eq. (39) for $\phi = 1$ that:

$$\frac{dV}{dt} = 0 \qquad \Longleftrightarrow \qquad V \equiv \int_\Omega \rho_0 \, d\Omega \qquad \forall t \in [0,T). \tag{40}$$

- The total free energy functional (29) is a Liapunov functional; indeed, it is possible to show from Eq. (39) that:

$$\frac{dF}{dt}(\rho;\lambda) = -C_0 \int_\Omega M(\rho)\nabla z_F(\rho;\lambda)\cdot\nabla z_F(\rho;\lambda)\, d\Omega \leq 0 \qquad \forall t \in [0,T). \tag{41}$$

  This implies that the phase transition occurs in such a manner that the energy associated to the Cahn–Hilliard equation is decreasing or at most conserved in time; this property also holds true for the Cahn–Allen equation, since in general:

$$\frac{dF}{dt}(\rho;\lambda) = -C_0 \|\operatorname{grad} F(\rho;\lambda)\|^2_{\mathcal{Z}} \leq 0, \tag{42}$$

  in the norm induced by $\mathcal{Z}$, see [40].

- Under suitable hypothesis on the function $\psi_B(\rho)$ including its analyticity, in [85] it is proved that, for a given ρ_0, the unique solution ρ converges to an equilibrium (steady state) and $\dfrac{\partial \rho}{\partial t} \to 0$ for $t \to \infty$ in the topology of the corresponding function spaces. This implies from Eqs. (31) and (42) that the steady state solution is a critical one for the total free energy $F(\rho;\lambda)$ [37], with $\dfrac{dF}{dt}(\rho;\lambda) \to 0$ for $t \to \infty$; it follows that $F(\rho;\lambda)$ evolves to a local minimum through the phase transition from the initial solution ρ_0.

4 Topology Optimization with the Phase Field Model

We derive now the phase field model for topology optimization similarly to [114]. First, we provide the generalized Cahn–Hilliard equation based on the multiphase approach of Sec. 2.2; then, we reformulate the problem as a coupled system with phase and displacements as independent variables and, finally, we discuss the dimensionless problem highlighting its dependence on dimensionless parameters.

4.1 The generalized Cahn–Hilliard equation

In Sec. 3 we derived the Cahn–Hilliard equation starting from a total free energy functional. We have observed that this phase field model is area/volume conservative and the phase transition occurs in such a manner that the energy of the system decreases in time. These two properties are crucial to recast the multiphase approach for topology optimization of Sec. 2.2 in a phase transition model, since an area/volume constraint is set in the minimum compliance case and a penalized objective functional needs to be minimized.

The derivation of the generalized Cahn–Hilliard equation for the topology optimization problem in the minimum compliance case follows in similar manner to Sec. 3 by using the penalized objective functional (15). In particular, we have that:

$$\frac{\partial \rho}{\partial t} = -\operatorname{grad} J(\rho; \boldsymbol{\mu}) \qquad \text{in } \Omega,\ \forall t \in [0, T), \tag{43}$$

where $\rho = \rho_0$ for $t = 0$ in Ω,

$$\operatorname{grad} J(\rho; \boldsymbol{\mu}) = -\nabla \cdot \left(M(\rho) \nabla z(\rho; \boldsymbol{\mu}) \right), \tag{44}$$

and the potential $z(\rho; \boldsymbol{\mu})$ deduced from the Gâteaux derivative in $L^2(\Omega)$ of the penalized objective functional (15):

$$(z(\rho; \boldsymbol{\mu}),\, \phi)_{L^2(\Omega)} = \frac{1}{E_0} \frac{dJ}{d\rho}(\rho; \boldsymbol{\mu})[\phi] \qquad \forall \phi \in H^1(\Omega), \tag{45}$$

for some $\boldsymbol{\mu} \in \mathcal{D}$. If we assume that $\nabla \rho \cdot \hat{\mathbf{n}} = 0$ on $\partial\Omega$, we have from Eq. (16) that:

$$z(\rho; \boldsymbol{\mu}) = \frac{\gamma}{E_0} z_E(\rho) + z_B(\rho) + \lambda z_I(\rho), \tag{46}$$

where $z_B(\rho)$ and $z_I(\rho)$ are defined in Eqs. (35) and (36), respectively, and:

$$z_E(\rho) := \frac{d\psi_E}{d\rho}(\rho). \tag{47}$$

In order to evaluate $z_E(\rho)$, further elaborations are needed since $\dfrac{d\psi_E}{d\rho}(\rho) = \dfrac{d\widetilde{\psi}_E}{d\rho}(\rho, \mathbf{u}(\rho))$ from Eq. (8); in particular, we have that:

$$z_E(\rho) = \frac{\partial \widetilde{\psi}_E}{\partial \rho}(\rho, \mathbf{u}(\rho)) + \frac{\partial \widetilde{\psi}_E}{\partial \mathbf{u}}(\rho, \mathbf{u}(\rho)) \left[\frac{d\mathbf{u}}{d\rho}(\rho) \right]. \tag{48}$$

From Eq. (9) we deduce that:

$$\frac{\partial \widetilde{\psi}_E}{\partial \rho}(\rho, \mathbf{u}) = \frac{\partial \widetilde{\sigma}}{\partial \rho}(\rho, \mathbf{u}) : \varepsilon(\mathbf{u}); \tag{49}$$

similarly, by recalling that $\widetilde{\sigma}(\rho, \mathbf{u})$ depends linearly on $\mathbf{u}$ and the elastic tensor $\mathbb{C}(\rho)$ is symmetric, we have:

$$\begin{aligned} \frac{\partial \widetilde{\psi}_E}{\partial \mathbf{u}}(\rho, \mathbf{u}) \left[\frac{d\mathbf{u}}{d\rho}\right] &= \left[\widetilde{\sigma}\left(\rho, \frac{d\mathbf{u}}{d\rho}\right) : \varepsilon(\mathbf{u}) + \widetilde{\sigma}(\rho, \mathbf{u}) : \varepsilon\left(\frac{d\mathbf{u}}{d\rho}\right)\right] \\ &= 2\widetilde{\sigma}\left(\rho, \frac{d\mathbf{u}}{d\rho}\right) : \varepsilon(\mathbf{u}). \end{aligned} \tag{50}$$

In order to evaluate the term $\widetilde{\sigma}\left(\rho, \dfrac{d\mathbf{u}}{d\rho}\right)$, we need to differentiate the weak form of the elasticity equation (5) with respect to ρ; by assuming that the function $\dfrac{d\mathbf{u}}{d\rho} \in \mathcal{V}$, we obtain:

$$\int_\Omega \widetilde{\sigma}\left(\rho, \frac{d\mathbf{u}}{d\rho}\right) : \varepsilon(\mathbf{v})\, d\Omega + \int_\Omega \frac{\partial \widetilde{\sigma}}{\partial \rho}(\rho, \mathbf{u}) : \varepsilon(\mathbf{v})\, d\Omega = 0 \qquad \forall \mathbf{v} \in \mathcal{V}, \tag{51}$$

and hence for $\mathbf{v} = \mathbf{u}$:

$$\widetilde{\sigma}\left(\rho, \frac{d\mathbf{u}}{d\rho}\right) : \varepsilon(\mathbf{u}) = -\frac{\partial \widetilde{\sigma}}{\partial \rho}(\rho, \mathbf{u}) : \varepsilon(\mathbf{u}) = -\frac{\partial \widetilde{\psi}_E}{\partial \rho}(\rho, \mathbf{u}). \tag{52}$$

By replacing the result (52) in Eq. (50), and then Eqs. (49) and (50) in Eq. (48), we obtain:

$$z_E(\rho) = \widetilde{z}_E(\rho, \mathbf{u}(\rho)), \tag{53}$$

with:

$$\widetilde{z}_E(\rho, \mathbf{u}) := -\frac{\partial \widetilde{\psi}_E}{\partial \rho}(\rho, \mathbf{u}). \tag{54}$$

The potential (46) can also be written as:

$$z(\rho; \boldsymbol{\mu}) := \widetilde{z}(\rho, \mathbf{u}(\rho); \boldsymbol{\mu}), \tag{55}$$

where:

$$\widetilde{z}(\rho, \mathbf{u}; \boldsymbol{\mu}) := \frac{\gamma}{E_0} \widetilde{z}_E(\rho, \mathbf{u}) + z_B(\rho) + \lambda z_I(\rho), \tag{56}$$

and equivalently:

$$\widetilde{z}(\rho, \mathbf{u}; \boldsymbol{\mu}) := -\frac{\gamma}{E_0} \frac{\partial \widetilde{\psi}_E}{\partial \rho}(\rho, \mathbf{u}) + \frac{d\psi_B}{d\rho}(\rho) - \lambda \Delta \rho. \tag{57}$$

It is now possible to introduce the strong form of the generalized Cahn–Hilliard equation for topology optimization from Eq. (43), which reads:

$$\begin{aligned} &\frac{\partial \rho}{\partial t} = \nabla \cdot (M(\rho) \nabla z(\rho; \boldsymbol{\mu})) && \text{in } \Omega,\ \forall t \in [0, T), \\ &M(\rho) \nabla z(\rho; \boldsymbol{\mu}) \cdot \hat{\mathbf{n}} = 0 && \text{on } \partial\Omega,\ \forall t \in [0, T), \\ &\nabla \rho \cdot \hat{\mathbf{n}} = 0 && \text{on } \partial\Omega,\ \forall t \in [0, T), \\ &\rho = \rho_0, && \text{in } \Omega,\ t = 0, \end{aligned} \tag{58}$$

for some $\boldsymbol{\mu} \in \mathcal{D}$. By recalling from Sec. 3 that $\rho \in \mathcal{H}$ for all $t \in [0, T)$, with $\mathcal{H} := \left\{\phi \in H^2(\Omega) : \nabla \phi \cdot \hat{\mathbf{n}} = 0\right\}$, we introduce the residual $R_\rho(\rho; \boldsymbol{\mu})(\phi) \in \mathbb{R}$ such that:

$$R_\rho(\rho; \boldsymbol{\mu})(\phi) := \int_\Omega \frac{\partial \rho}{\partial t}\, \phi \, d\Omega + \int_\Omega M(\rho) \nabla z(\rho; \boldsymbol{\mu}) \cdot \nabla \phi \, d\Omega. \tag{59}$$

It follows that the weak form of the generalized Cahn–Hilliard equation is:

$$\begin{aligned} &\text{find } \rho \in \mathcal{W} \ : \ R_\rho(\rho(t;\boldsymbol{\mu});\boldsymbol{\mu})(\phi) = 0 \qquad \forall \phi \in \mathcal{H}, \ \forall t \in [0,T), \\ &\text{with } \rho = \rho_0 \quad \text{in } \Omega, \ t = 0, \end{aligned} \tag{60}$$

for some $\boldsymbol{\mu} \in \mathcal{D}$. We observe that Eq. (60) is obtained with the natural boundary condition $M(\rho)\nabla z(\rho;\boldsymbol{\mu})\cdot\hat{\mathbf{n}} = 0$ and the essential one $\nabla\rho\cdot\hat{\mathbf{n}} = 0$ defined on the boundary $\partial\Omega$; due to its nature, the latter is embedded in the space $\mathcal{H}$.

The generalized Cahn–Hilliard equation (60) (or Eq.(58)) represents a model for topology optimization problems in the minimum compliance case, for which the following properties hold similarly to the Cahn–Hilliard equation:

- The unique solution ρ exists by extending the result of [85] under suitable hypothesis on the bulk and strain energy functions $\psi_B(\rho)$ and $\psi_E(\rho)$, in the case of constant mobility.
- The area/volume covered by the material in the design domain Ω is constant during the phase transition; see Eq. (40).
- The penalized objective functional $J(\rho;\boldsymbol{\mu})$ (15) is a Liapunov functional which evolves in time by decreasing from the initial value corresponding to ρ_0; indeed, from Eq. (42) in analogy with Eq. (41), we have:

$$\frac{dJ}{dt}(\rho;\boldsymbol{\mu}) = -E_0 \int_\Omega M(\rho)\nabla z(\rho;\boldsymbol{\mu}) \cdot \nabla z(\rho;\boldsymbol{\mu})\, d\Omega \leq 0 \qquad \forall t \in [0,T). \tag{61}$$

- If the functions $\psi_B(\rho)$ and $\psi_E(\rho)$ satisfy the hypothesis made in [85] for the bulk energy of the Cahn–Hilliard equation, the unique solution ρ converges to a steady state which minimizes the penalized objective functional $J(\rho;\boldsymbol{\mu})$ of the multiphase approach with respect to the initial solution ρ_0; in this manner, the optimization problem is converted to a time dependent one and its optimal solution ρ^* is obtained as ρ for $t \to \infty$.
- The topology optimization problem is completely defined in the formulation by choosing the data $\mathbf{h}$, $\mathbf{f}$, $\mathbb{C}_0$ and Ω, the function $g(\rho)$ in Eq.(1), the mobility $M(\rho)$, the initial condition ρ_0 (which also introduces the area/volume constraint V) and the parameters $\boldsymbol{\mu} \in \mathcal{D}$.

In the current work we do not provide a rigorous analysis of the generalized Cahn–Hilliard equation for topology optimization problems. At this point, we only speculate on the possibility that the bulk $\psi_B(\rho)$ and especially the strain energy $\psi_E(\rho)$ functions could satisfy the hypothesis made in [85] for the existence and uniqueness of the solution ρ and its convergence to a steady state, the minimizer of $J(\rho;\boldsymbol{\mu})$; further limitations on the material interpolation model could be eventually deduced to fit such hypothesis. However, we observe that numerical tests exhibit the convergence of the solution to a steady state for any given initial solution, for which we feel that the validity of the considered phase field model could be shown also from an analytical point of view.

4.2 The coupled system

The generalized Cahn–Hilliard equation (60) (or Eq. (58) in strong form) is written in terms of the phase variable ρ. However, in order to solve the problem it is necessary to evaluate the displacement $\mathbf{u}(\rho)$ by solving the elasticity equation (5) for a given value of ρ. In practice, for each $t \in [0, T)$, there is a corresponding displacement $\mathbf{u} \in \mathcal{V}$. For this reason, it is convenient to consider the phase ρ and the displacement $\mathbf{u}$ as two independent variables and rewrite the generalized Cahn–Hilliard equation as a coupled system of equations.

By recalling Eqs. (58), (56) and (3), the strong form of the coupled system is:

$$\begin{aligned}
&\frac{\partial \rho}{\partial t} = \nabla \cdot (M(\rho) \nabla \widetilde{z}(\rho, \mathbf{u}; \boldsymbol{\mu})) && \text{in } \Omega,\ \forall t \in [0, T),\\
&-\nabla \cdot \widetilde{\sigma}(\rho, \mathbf{u}) = \mathbf{f} && \text{in } \Omega,\ \forall t \in [0, T),\\
&M(\rho) \nabla \widetilde{z}(\rho, \mathbf{u}; \boldsymbol{\mu}) \cdot \hat{\mathbf{n}} = 0 && \text{on } \partial\Omega,\ \forall t \in [0, T),\\
&\nabla \rho \cdot \hat{\mathbf{n}} = 0 && \text{on } \partial\Omega,\ \forall t \in [0, T),\\
&\mathbf{u} = \mathbf{0} && \text{on } \Gamma_D,\ \forall t \in [0, T),\\
&\widetilde{\sigma}(\rho, \mathbf{u}) \hat{\mathbf{n}} = \mathbf{h} && \text{on } \Gamma_N,\ \forall t \in [0, T),\\
&\rho = \rho_0, && \text{in } \Omega,\ t = 0,
\end{aligned} \tag{62}$$

for some $\boldsymbol{\mu} \in \mathcal{D}$. Also, for each $t \in [0, T)$, we define the residual $\widetilde{R}_\rho(\rho, \mathbf{u}; \boldsymbol{\mu})(\phi) \in \mathbb{R}$ from Eq. (59) by recalling the potential $\widetilde{z}(\rho, \mathbf{u}; \boldsymbol{\mu})$ (56):

$$\widetilde{R}_\rho(\rho, \mathbf{u}; \boldsymbol{\mu})(\phi) := \int_\Omega \frac{\partial \rho}{\partial t}\, \phi \, d\Omega + \int_\Omega M(\rho) \nabla \widetilde{z}(\rho, \mathbf{u}; \boldsymbol{\mu}) \cdot \nabla \phi \, d\Omega; \tag{63}$$

similarly, from Eq. (4), for each $t \in [0, T)$, we redefine $\widetilde{R}_{\mathbf{u}}(\rho, \mathbf{u}; \boldsymbol{\mu})(\mathbf{v}) \in \mathbb{R}$ to highlight the explicit dependency on ρ and $\mathbf{u}$ as:

$$\widetilde{R}_{\mathbf{u}}(\rho, \mathbf{u}; \boldsymbol{\mu})(\mathbf{v}) := \int_\Omega \widetilde{\sigma}(\rho, \mathbf{u}) : \varepsilon(\mathbf{v}) \, d\Omega - \int_\Omega \mathbf{f} \cdot \mathbf{v} \, d\Omega - \oint_{\Gamma_N} \mathbf{h} \cdot \mathbf{v} \, d\Gamma_N. \tag{64}$$

Then, the coupled system of generalized Cahn–Hilliard and elasticity equations in weak form, which we will indicate as $\mathrm{TO}(\boldsymbol{\mu})$, reads:

$$\mathrm{TO}(\boldsymbol{\mu}) \qquad \begin{aligned}
&\text{find } \rho \in \mathcal{W},\ \mathbf{u} \in \mathcal{V}\ : \\
&\widetilde{R}_\rho(\rho, \mathbf{u}; \boldsymbol{\mu})(\phi) = 0 && \forall \phi \in \mathcal{H},\ \forall t \in [0, T)\\
&\widetilde{R}_{\mathbf{u}}(\rho, \mathbf{u}; \boldsymbol{\mu})(\mathbf{v}) = 0 && \forall \mathbf{v} \in \mathcal{V},\ \forall t \in [0, T),\\
&\text{with } \rho = \rho_0 && \text{in } \Omega,\ t = 0,
\end{aligned} \tag{65}$$

for some $\boldsymbol{\mu} \in \mathcal{D}$ and the associated energy $\widetilde{J}(\rho, \mathbf{u}; \boldsymbol{\mu})$ defined in Eq. (22). We observe that the displacement $\mathbf{u}$ depends on the time $t \in [0, T)$ implicitly trough the variation of the phase ρ. Indeed, in the elasticity equation no time derivatives appear, meaning that the displacement adapts instantaneously to the variation of the phase.

The reformulation of the generalized Cahn–Hilliard equation (60) (or Eq. (58)) into the coupled system $\mathrm{TO}(\boldsymbol{\mu})$ (65) provides an approach to analyze the problem in terms of existence and uniqueness. Indeed, we notice that the coupled system (65) shows many analogies with the Cahn–Hilliard equation with elastic misfit, also known as the Cahn–Larchè model [62], for which the phase transition is also driven by elastic interactions of the material [42, 73]. In [42] the existence of a solution of such a system is proved as well as its uniqueness for a specific choice of the elastic energy; in [43] the corresponding discretized problem is analyzed. However, we remark that the Cahn–Larché equations and the coupled system TO($\boldsymbol{\mu}$) (65) corresponding to the generalized Cahn–Hilliard equations are derived from different concepts. Indeed, the first equations follow from thermodynamical considerations and balance laws for the species and the momentum with ρ and $\mathbf{u}$ as independent variables. Conversely, the generalized Cahn–Hilliard equation is developed by considering the displacement variable as dependent on the phase variable $\mathbf{u}(\rho)$ and only the balance of the species is taken into account; the coupled system TO($\boldsymbol{\mu}$) only represents a reformulation of such an equation.

4.3 Dimensionless form of the coupled system

We now rewrite the coupled system (65) in dimensionless form. With this aim, we introduce the dimensionless space and time coordinates:

$$\mathrm{x}_i^\star = \mathrm{x}_i/L_0,\ i=1,\dots,d, \qquad t^\star = t/T_0 \tag{66}$$

and the phase and displacement variables:

$$\rho^\star = \rho, \qquad \mathbf{u}^\star = \mathbf{u}/L_0, \tag{67}$$

where L_0 and T_0 are representative length and time scales, while the superscript $\star$ indicates dimensionless variables. Also, if we use E_0 as the representative Young modulus, we obtain:

$$\varepsilon^\star(\mathbf{u}^\star) = \varepsilon(\mathbf{u}), \qquad \widetilde{\sigma}^\star(\rho^\star,\mathbf{u}^\star) = \widetilde{\sigma}(\rho,\mathbf{u})/E_0, \tag{68}$$

and

$$\begin{aligned} \widetilde{z}_E^\star(\rho^\star,\mathbf{u}^\star) &= \widetilde{z}_E(\rho,\mathbf{u})/E_0, & \widetilde{\psi}_E^\star(\rho^\star,\mathbf{u}^\star) &= \widetilde{\psi}_E(\rho,\mathbf{u})/E_0,\\ z_B^\star(\rho^\star) &= z_B(\rho), & \psi_B^\star(\rho^\star) &= \psi_B(\rho),\\ z_I^\star(\rho^\star) &= L_0^2\, z_I(\rho), & \psi_I^\star(\rho^\star) &= L_0^2\,\psi_I(\rho), \end{aligned} \tag{69}$$

while defining the reference surface and body forces $\hbar_0$ and f_0, we have:

$$\mathbf{h}^\star = \mathbf{h}/\hbar_0, \qquad \mathbf{f}^\star = \mathbf{f}/f_0; \tag{70}$$

finally, the dimensionless mobility is:

$$M^\star(\rho^\star) = M(\rho)/M_0. \tag{71}$$

Let us define the following dimensionless parameters which we indicate with the vector $\mathbf{D} = (D_1,\dots,D_5)$ such that:

$$\begin{aligned} D_1 &:= \frac{L_0^4}{T_0\lambda M_0}, & D_2 &:= \frac{L_0^2}{\lambda}, & D_3 &:= \gamma\frac{L_0^2}{\lambda},\\ D_4 &:= \frac{E_0}{\hbar_0}, & D_5 &:= \frac{f_0 L_0}{\hbar_0}; \end{aligned} \tag{72}$$

we observe that the parameter γ is dimensionless, while the parameter λ assumes the same dimension as L_0^2. Moreover, we define the dimensionless potential:

$$\widetilde{z}^\star(\rho^\star,\mathbf{u}^\star;\mathbf{D}) := D_3\,\widetilde{z}_E^\star(\rho^\star,\mathbf{u}^\star) + D_2\, z_B^\star(\rho^\star) + z_I^\star(\rho^\star), \tag{73}$$

for which $\widetilde{z}^\star(\rho^\star, \mathbf{u}^\star; \mathbf{D}) = D_2 \widetilde{z}(\rho, \mathbf{u}; \boldsymbol{\mu})$ and the dimensionless energy function:

$$\widetilde{\psi}^\star(\rho^\star, \mathbf{u}^\star; \mathbf{D}) := D_3\, \widetilde{\psi}_E^\star(\rho^\star, \mathbf{u}^\star) + D_2\, \psi_B^\star(\rho^\star) + \psi_I^\star(\rho^\star), \tag{74}$$

for which $\widetilde{\psi}^\star(\rho^\star, \mathbf{u}^\star; \mathbf{D}) = \dfrac{D_2}{E_0} \widetilde{\psi}(\rho, \mathbf{u}; \boldsymbol{\mu})$. With these, we define from Eq. (63) the dimensionless residual $\widetilde{R}_\rho^\star(\rho^\star, \mathbf{u}^\star; \mathbf{D})(\phi^\star) \in \mathbb{R}\ \forall t \in [0, T)$:

$$\begin{aligned} \widetilde{R}_\rho^\star(\rho^\star, \mathbf{u}^\star; \mathbf{D})(\phi^\star) \quad := \quad & D_1 \int_{\Omega^\star} \frac{\partial \rho^\star}{\partial t^\star}\, \phi^\star \, d\Omega^\star \\ & + \int_{\Omega^\star} M^\star(\rho) \nabla^\star \widetilde{z}^\star(\rho^\star, \mathbf{u}^\star; D_2, D_3) \cdot \nabla^\star \phi^\star \, d\Omega^\star, \end{aligned} \tag{75}$$

for which $\widetilde{R}_\rho^\star(\rho^\star, \mathbf{u}^\star; \mathbf{D})(\phi^\star) = \dfrac{L_0^{4-d}}{\lambda M_0} \widetilde{R}_\rho(\rho, \mathbf{u}; \boldsymbol{\mu})(\phi)$; similarly, from Eq. (64) we define $\widetilde{R}_\mathbf{u}^\star(\rho^\star, \mathbf{u}^\star; \mathbf{D})(\mathbf{v}^\star) \in \mathbb{R}\ \forall t \in [0, T)$ as:

$$\begin{aligned} \widetilde{R}_\mathbf{u}^\star(\rho^\star, \mathbf{u}^\star; \mathbf{D})(\mathbf{v}^\star) \quad := \quad & D_4 \int_{\Omega^\star} \widetilde{\sigma}^\star(\rho^\star, \mathbf{u}^\star) : \varepsilon^\star(\mathbf{v}^\star) \, d\Omega^\star \\ & - D_5 \int_{\Omega^\star} \mathbf{f}^\star \cdot \mathbf{v}^\star \, d\Omega^\star - \oint_{\Gamma_N^\star} \mathbf{h}^\star \cdot \mathbf{v}^\star \, d\Gamma_N^\star, \end{aligned} \tag{76}$$

with $\widetilde{R}_\mathbf{u}^\star(\rho^\star, \mathbf{u}^\star; \mathbf{D})(\mathbf{u}^\star) = \dfrac{1}{\hbar_0 L_0^d}\, \widetilde{R}_\mathbf{u}(\rho, \mathbf{u}; \boldsymbol{\mu})(\mathbf{v})$. It follows that the dimensionless topology optimization problem in the phase field approach reads:

$$\mathrm{TO}^\star\,(\mathbf{D}) \qquad \begin{aligned} & \text{find } \rho^\star \in \mathcal{W},\ \mathbf{u}^\star \in \mathcal{V}\ : \\ & \widetilde{R}_\rho^\star(\rho^\star, \mathbf{u}^\star; \mathbf{D})(\phi^\star) = 0 && \forall \phi^\star \in \mathcal{H},\ \forall t^\star \in [0, T^\star) \\ & \widetilde{R}_\mathbf{u}^\star(\rho^\star, \mathbf{u}^\star; \mathbf{D})(\mathbf{v}^\star) = 0 && \forall \mathbf{v}^\star \in \mathcal{V},\ \forall t^\star \in [0, T^\star), \\ & \text{with } \rho^\star = \rho_0^\star && \text{in } \Omega^\star,\ t^\star = 0, \end{aligned} \tag{77}$$

with $\rho_0^\star = \rho_0$ and $T^\star = T/T_0$. The corresponding dimensionless penalized objective functional (energy) follows from Eq. (74) as:

$$\widetilde{J}^\star(\rho^\star, \mathbf{u}^\star; \mathbf{D}) = \int_{\Omega^\star} \widetilde{\psi}^\star(\rho^\star, \mathbf{u}^\star; D_2, D_3) \, d\Omega^\star, \tag{78}$$

with $\widetilde{J}^\star(\rho^\star, \mathbf{u}^\star; \mathbf{D}) = \dfrac{1}{E_0} \dfrac{L_0^{2-d}}{\lambda} \widetilde{J}(\rho, \mathbf{u}; \boldsymbol{\mu})$; the same scaling occurs for $\widetilde{J}_E^\star(\rho^\star, \mathbf{u}^\star)$, $J_B^\star(\rho^\star)$ and $J_I^\star(\rho^\star)$.

We notice that the topology optimization problem (77) fully depends on the dimensionless parameters $\mathbf{D}$ and the initial solution $\rho_0^\star$, for which the principle of dimensional similitude can be applied. Also, it is possible to reduce the parametric dependence by setting $D_1 = 1$ and hence choosing the representative time scale as $T_0 = \dfrac{L_0^4}{\lambda M_0}$; it follows that the problem $\mathrm{TO}^\star\,(\mathbf{D})$ (77) depends on $\mathbf{D} = (D_2, \ldots, D_5)$.

We observe from Eq. (76) that the dimensionless parameters D_4 and D_5 of Eq. (72) only affect the linear elasticity equation. The dimensionless parameters D_2 and D_3 are responsible for changing the optimal solution of $\mathrm{TO}^\star\,(\mathbf{D})$ once the data are set; indeed they control the balance of the strain, bulk and interfaces energies in the penalized objective functional (78). From Eq. (74), we deduce that if D_3 is very large, then the phase field solution is dominated by the minimum compliance term of the penalized objective functional. Conversely, if $D_3 \to 0$, specifically if due to $\gamma \to 0$, $\mathrm{TO}^\star(\mathbf{D})$ solves the standard Cahn–Hilliard equation for the phase problem with the displacement $\mathbf{u}^\star$ depending on the distribution of $\rho^\star$ in $\Omega^\star$. Also, since from Eq. (72) $D_3 = \gamma D_2$ and $D_2 \sim 1/\lambda$, with λ related to the control of the thickness of the interfaces, we have that D_2 and $D_3 \gg 1$, when sharp interfaces are required.

Remark 4.1 *For the sake of simplicity, we henceforth omit the superscript* $\star$ *to indicate dimensionless quantities.*

5 Numerical Approximation

In this section we discuss the numerical approximation of the topology optimization problem TO($\mathbf{D}$) (77) by using a similar approach to the one used in [46, 48] for phase field problems. In particular, for the spatial approximation we consider Isogeometric Analysis [33, 55], while for the temporal approximation we use the generalized–α method [31] with time adaptivity.

5.1 The spatial approximation

We consider design domains Ω described by a NURBS (or B–spline basis) [80], for both the two and three–dimensional cases. The use of Isogeometric Analysis for the spatial approximation of the PDEs allows us to encapsulate directly the geometry representation in the analysis, by using the same basis functions used to represent the geometry [33, 55]. In this manner, no geometrical approximations are introduced in the analysis of the topology optimization problem TO($\mathbf{D}$) (77).

Isogeometric Analysis provides a way to easily achieve high–order continuity in the approximated solution without introducing extra degrees of freedom. In particular, for the TO($\mathbf{D}$) problem, the use of globally $C^1(\Omega)$–continuous basis functions is necessary to approximate the functional space $\mathcal{H}$ of the phase variable ρ. Specifically, we consider basis functions of degree $p \geq 2$ defined by open knot vectors with equally spaced internal knots repeated at most $p-1$ times; in this manner we ensure that the basis functions are globally $C^1(\Omega)$–continuous. We consider the same basis functions for the phase ρ and the displacement $\mathbf{u}$.

We introduce the finite dimensional spaces $\mathcal{H}_h \subset \mathcal{H}$ and $\mathcal{V}_h \subset \mathcal{V}$, with the above mentioned properties, of dimensions $n_{h,\rho} := \dim(\mathcal{H}_h)$ and $n_{h,\mathbf{u}} := \dim(\mathcal{V}_h)$. Due to the properties of the NURBS basis, the essential boundary condition $\nabla\rho \cdot \hat{\mathbf{n}} = 0$ is easily introduced in the space $\mathcal{H}_h$ by imposing equality of two consecutive control values of ρ normal to the boundary. We illustrate strong imposition of the essential boundary condition in Fig. 2 for a one–dimensional B–spline basis of degree 2. This also holds for NURBS and for the multidimensional case. For each $t \in [0, T)$, $\rho_h \in \mathcal{H}_h$ and $\mathbf{u}_h \in \mathcal{V}_h$ have the representations:

$$\rho_h(t, \mathbf{x}) = \sum_{A=1}^{n_{bf}} \rho_A(t) N_A(\mathbf{x}), \qquad \mathbf{u}_h(t, \mathbf{x}) = \sum_{A=1}^{n_{bf}} \mathbf{u}_A(t) N_A(\mathbf{x}), \tag{79}$$

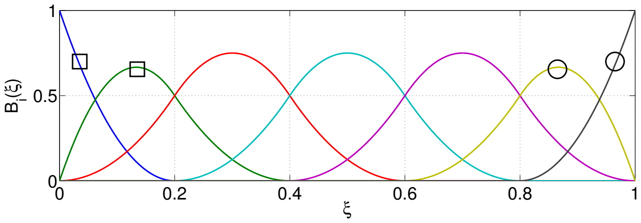

Figure 2: B–spline basis of degree 2 and knot vector $\Xi = \{\{0\}_{i=1}^{3}, 0.2, 0.4, 0.6, 0.8, \{1\}_{i=1}^{3}\}$; the two external pairs of basis functions are marked with squares and circles to indicate that the corresponding control variables need to be equal to impose the boundary condition $\nabla\rho \cdot \hat{\mathbf{n}} = 0$ on $\partial\Omega$.

with $N_A(\mathbf{x})$ the NURBS basis and n_{bf} the number of basis functions; the corresponding test functions are:

$$\phi_h(\mathbf{x}) = \sum_{A=1}^{n_{bf}} \phi_A N_A(\mathbf{x}), \qquad \mathbf{v}_h(\mathbf{x}) = \sum_{A=1}^{n_{bf}} \mathbf{v}_A N_A(\mathbf{x}). \tag{80}$$

Then the discrete $\mathrm{TO}_h(\mathbf{D})$ coupled problem for any $t \in [0, T)$ is:

$$\mathrm{TO}_h\,(\mathbf{D}) \qquad \begin{aligned} &\text{find } \rho_h \in \mathcal{H}_h,\ \mathbf{u}_h \in \mathcal{V}_h \ : \\ &\widetilde{R}_\rho(\rho_h, \mathbf{u}_h; \mathbf{D})(\phi_h) = 0 \qquad && \forall \phi_h \in \mathcal{H}_h, \\ &\widetilde{R}_{\mathbf{u}}(\rho_h, \mathbf{u}_h; \mathbf{D})(\mathbf{v}_h) = 0 \qquad && \forall \mathbf{v}_h \in \mathcal{V}_h, \end{aligned} \tag{81}$$

where the discrete initial condition $\rho_{0,h}$ is obtained as the $L^2(\Omega)$ projection of ρ_0 in the space $\mathcal{H}_h$. The total number of degrees of freedom of $\mathrm{TO}_h(\mathbf{D})$ is $n_h := n_{h,\rho} + n_{h,\mathbf{u}}$. Finally, we introduce from Eq. (79) the vectors of control variables:

$$\dot{\mathbf{P}}(t) := \{\dot{\rho}_A(t)\}_{A=1}^{n_{bf}}, \qquad \mathbf{P}(t) := \{\rho_A(t)\}_{A=1}^{n_{bf}}, \qquad \mathbf{U}(t) := \{\mathbf{u}_A(t)\}_{A=1}^{n_{bf}}, \tag{82}$$

and, from Eqs. (75) and (76), the discrete residuals:

$$\begin{aligned} \mathbf{R}_\rho\left(\dot{\mathbf{P}}(t), \mathbf{P}(t), \mathbf{U}(t)\right) &:= \left\{\widetilde{R}_\rho(\rho_h, \mathbf{u}_h; \mathbf{D})(N_A)\right\}_{A=1}^{n_{bf}}, \\ \mathbf{R}_{\mathbf{u}}\left(\dot{\mathbf{P}}(t), \mathbf{P}(t), \mathbf{U}(t)\right) &:= \left\{\left\{\widetilde{R}_{\mathbf{u}}(\rho_h, \mathbf{u}_h; \mathbf{D})(N_A \hat{\mathbf{e}}_i)\right\}_{i=1}^{d}\right\}_{A=1}^{n_{bf}}, \end{aligned} \tag{83}$$

where $\hat{\mathbf{e}}_i$, with $i = 1, \ldots, d$, represent the orthonormal basis of the space $\mathbb{R}^d$; for the sake of simplicity, we neglected the explicit dependency of the discrete residuals on $\mathbf{D}$ in Eq. (83).

5.2 The time approximation

The time approximation of the TO($\mathbf{D}$) problem (77) represents a challenge similar to that for the Cahn–Hilliard equation due to the fourth–order term and significant nonlinearities. We use the generalized–α method; see [31, 57] and also [8, 46]. Moreover, since the solution of the topology optimization problem is obtained as the steady state solution of the coupled system (77), i.e. for $t \to \infty$ (or T sufficiently large), we need an adaptive time scheme that reduces the time step size when necessary and increases it as the solution approaches the steady state. We employ the same procedure proposed in [46] for the Cahn–Hilliard equation, which is based on an accuracy criterion and reduces the computational costs of the simulation while maintaing an adequate level of accuracy.

Very recently, a new second–order accurate, provably unconditionally stable, time integration algorithm for phase field models has been developed in [47]. This would provide a viable alternative to the generalized–α method.

5.2.1 Time step scheme

Let us subdivide the time interval $[0, T)$ by introducing the discrete time vector $\{t_n\}_{n=0}^{n_{ts}}$, with $\Delta t_n := t_{n+1} - t_n$ the width of the time interval at the step t_n, for which the control variables (82) are $\dot{\mathbf{P}}_{n+1} = \dot{\mathbf{P}}(t_n)$, $\mathbf{P}_{n+1} = \mathbf{P}(t_n)$ and $\mathbf{U}_{n+1} = \mathbf{U}(t_n)$. Then, if we interpret the variables $\dot{\mathbf{P}}_{n+1}$ and $\mathbf{P}_{n+1}$ as independent, the generalized–α method for the TO$_h$($\mathbf{D}$) problem at time step t_{n+1} reads from Eq. (83):

$$\begin{aligned}
&\text{find } \dot{\mathbf{P}}_{n+1},\ \mathbf{P}_{n+1},\ \dot{\mathbf{P}}_{n+\alpha_m},\ \mathbf{P}_{n+\alpha_f},\ \mathbf{U}_{n+1}\ :\\
&\mathbf{R}_\rho\left(\dot{\mathbf{P}}_{n+\alpha_m}, \mathbf{P}_{n+\alpha_f}, \mathbf{U}_{n+1}\right) = \mathbf{0},\\
&\mathbf{R}_\mathbf{u}\left(\dot{\mathbf{P}}_{n+\alpha_m}, \mathbf{P}_{n+\alpha_f}, \mathbf{U}_{n+1}\right) = \mathbf{0},\\
&\mathbf{P}_{n+1} = \mathbf{P}_n + \Delta t_n \dot{\mathbf{P}}_n + \delta \Delta t_n \left(\dot{\mathbf{P}}_{n+1} - \dot{\mathbf{P}}_n\right),\\
&\dot{\mathbf{P}}_{n+\alpha_m} = \dot{\mathbf{P}}_n + \alpha_m \left(\dot{\mathbf{P}}_{n+1} - \dot{\mathbf{P}}_n\right),\\
&\mathbf{P}_{n+\alpha_f} = \mathbf{P}_n + \alpha_f \left(\mathbf{P}_{n+1} - \mathbf{P}_n\right),
\end{aligned} \tag{84}$$

with $\dot{\mathbf{P}}_n$ and $\mathbf{P}_n$ given; the parameters α_m, α_f and $\delta \in \mathbb{R}$, chosen on the basis of stability and accuracy considerations, define a specific generalized–α method. As described in [54, 57] we select α_m, α_f and δ as follows:

$$\alpha_m = \frac{1}{2}\left(\frac{3 - \rho_\infty}{1 + \rho_\infty}\right), \qquad \alpha_f = \frac{1}{1 + \rho_\infty}, \qquad \delta = \frac{1}{2} + \alpha_m - \alpha_f, \tag{85}$$

where $\rho_\infty \in [0, 1]$ is the spectral radius of the amplification matrix at $\Delta t \to \infty$. See [54, 57] for further details.

The nonlinear system (84) is solved for each time step t_{n+1}, for $n = 0, \ldots, n_{ts} - 1$, by means of a two stage predictor–multicorrector algorithm, for which the control variables at the time step t_{n+1} are obtained iteratively, where $\dot{\mathbf{P}}_{n+1,(i)}$, $\mathbf{P}_{n+1,(i)}$ and $\mathbf{U}_{n+1,(i)}$, for $i = 0, 1, \ldots, i_{max}$, are the iterates and where $i = 0$ indicates the predictor. At the *predictor stage* the control variables are initialized as:

$$\begin{aligned}\dot{\mathbf{P}}_{n+1,(0)} &= \frac{\delta-1}{\delta}\dot{\mathbf{P}}_n,\\ \mathbf{P}_{n+1,(0)} &= \mathbf{P}_n,\\ \mathbf{U}_{n+1,(0)} &= \mathbf{U}_n.\end{aligned} \tag{86}$$

At the *multicorrector stage* the following iteration steps are repeated for $i = 1, \ldots, i_{max}$:

1. Update the control variables following the last two relations of Eq. (84):

$$\begin{aligned}\dot{\mathbf{P}}_{n+\alpha_m,(i)} &= \dot{\mathbf{P}}_n + \alpha_m \left(\dot{\mathbf{P}}_{n+1,(i-1)} - \dot{\mathbf{P}}_n\right),\\ \mathbf{P}_{n+\alpha_f,(i)} &= \mathbf{P}_n + \alpha_f \left(\mathbf{P}_{n+1,(i-1)} - \mathbf{P}_n\right),\\ \mathbf{U}_{n+1,(i)} &= \mathbf{U}_{n+1,(i-1)}.\end{aligned} \tag{87}$$

2. Assemble the residuals:

$$\begin{aligned}\mathbf{R}_{\rho,(i)} &:= \mathbf{R}_\rho \left(\dot{\mathbf{P}}_{n+\alpha_m,(i)}, \mathbf{P}_{n+\alpha_f,(i)}, \mathbf{U}_{n+1,(i)}\right),\\ \mathbf{R}_{\mathbf{u},(i)} &:= \mathbf{R}_{\mathbf{u}} \left(\dot{\mathbf{P}}_{n+\alpha_m,(i)}, \mathbf{P}_{n+\alpha_f,(i)}, \mathbf{U}_{n+1,(i)}\right).\end{aligned} \tag{88}$$

3. If the following stopping criteria on the relative norms of the residuals:

$$\frac{\|\mathbf{R}_{\rho,(i)}\|}{\|\mathbf{R}_{\rho,(0)}\|} < tol_R \quad \text{and} \quad \frac{\|\mathbf{R}_{\mathbf{u},(i)}\|}{\|\mathbf{R}_{\mathbf{u},(0)}\|} < tol_R \tag{89}$$

   are satisfied for a prescribed tolerance tol_R, set the control variables at time step t_{n+1} as $\dot{\mathbf{P}}_{n+1} = \dot{\mathbf{P}}_{n+1,(i-1)}$, $\mathbf{P}_{n+1} = \mathbf{P}_{n+1,(i-1)}$ and $\mathbf{U}_{n+1} = \mathbf{U}_{n+1,(i-1)}$ and exit the multicorrector stage; else proceed to step 4.

4. Define the consistent tangent matrices from Eq. (83):

$$\begin{aligned}\mathbf{K}_{\rho\rho,(i)} &:= \mathbf{K}_{\rho\rho} \left(\dot{\mathbf{P}}_{n+\alpha_m,(i)}, \mathbf{P}_{n+\alpha_f,(i)}, \mathbf{U}_{n+1,(i)}\right),\\ \mathbf{K}_{\rho\mathbf{u},(i)} &:= \mathbf{K}_{\rho\mathbf{u}} \left(\dot{\mathbf{P}}_{n+\alpha_m,(i)}, \mathbf{P}_{n+\alpha_f,(i)}, \mathbf{U}_{n+1,(i)}\right),\\ \mathbf{K}_{\mathbf{u}\rho,(i)} &:= \mathbf{K}_{\mathbf{u}\rho} \left(\dot{\mathbf{P}}_{n+\alpha_m,(i)}, \mathbf{P}_{n+\alpha_f,(i)}, \mathbf{U}_{n+1,(i)}\right),\\ \mathbf{K}_{\mathbf{uu},(i)} &:= \mathbf{K}_{\mathbf{uu}} \left(\dot{\mathbf{P}}_{n+\alpha_m,(i)}, \mathbf{P}_{n+\alpha_f,(i)}, \mathbf{U}_{n+1,(i)}\right),\end{aligned} \tag{90}$$

where, by using Eq. (84), we have:

$$
\begin{aligned}
\mathbf{K}_{\rho\rho}\left(\dot{\mathbf{P}}_{n+\alpha_m},\mathbf{P}_{n+\alpha_f},\mathbf{U}_{n+1}\right) &:= \frac{\partial\mathbf{R}_\rho\left(\dot{\mathbf{P}}_{n+\alpha_m},\mathbf{P}_{n+\alpha_f},\mathbf{U}_{n+1}\right)}{\partial\dot{\mathbf{P}}_{n+\alpha_m}}\frac{\partial\dot{\mathbf{P}}_{n+\alpha_m}}{\partial\mathbf{P}_{n+1}} \\
&\quad +\frac{\partial\mathbf{R}_\rho\left(\dot{\mathbf{P}}_{n+\alpha_m},\mathbf{P}_{n+\alpha_f},\mathbf{U}_{n+1}\right)}{\partial\mathbf{P}_{n+\alpha_f}}\frac{\partial\mathbf{P}_{n+\alpha_f}}{\partial\mathbf{P}_{n+1}} \\
&= \frac{\alpha_m}{\delta\Delta t_n}\frac{\partial\mathbf{R}_\rho\left(\dot{\mathbf{P}}_{n+\alpha_m},\mathbf{P}_{n+\alpha_f},\mathbf{U}_{n+1}\right)}{\partial\dot{\mathbf{P}}_{n+\alpha_m}} \\
&\quad +\alpha_f\frac{\partial\mathbf{R}_\rho\left(\dot{\mathbf{P}}_{n+\alpha_m},\mathbf{P}_{n+\alpha_f},\mathbf{U}_{n+1}\right)}{\partial\mathbf{P}_{n+\alpha_f}}, \\
\mathbf{K}_{\rho\mathbf{u}}\left(\dot{\mathbf{P}}_{n+\alpha_m},\mathbf{P}_{n+\alpha_f},\mathbf{U}_{n+1}\right) &:= \frac{\partial\mathbf{R}_\rho\left(\dot{\mathbf{P}}_{n+\alpha_m},\mathbf{P}_{n+\alpha_f},\mathbf{U}_{n+1}\right)}{\partial\mathbf{U}_{n+1}}, \\
\mathbf{K}_{\mathbf{u}\rho}\left(\dot{\mathbf{P}}_{n+\alpha_m},\mathbf{P}_{n+\alpha_f},\mathbf{U}_{n+1}\right) &:= \frac{\partial\mathbf{R}_\mathbf{u}\left(\dot{\mathbf{P}}_{n+\alpha_m},\mathbf{P}_{n+\alpha_f},\mathbf{U}_{n+1}\right)}{\partial\dot{\mathbf{P}}_{n+\alpha_m}}\frac{\partial\dot{\mathbf{P}}_{n+\alpha_m}}{\partial\mathbf{P}_{n+1}} \\
&\quad +\frac{\partial\mathbf{R}_\mathbf{u}\left(\dot{\mathbf{P}}_{n+\alpha_m},\mathbf{P}_{n+\alpha_f},\mathbf{U}_{n+1}\right)}{\partial\mathbf{P}_{n+\alpha_f}}\frac{\partial\mathbf{P}_{n+\alpha_f}}{\partial\mathbf{P}_{n+1}} \\
&= \frac{\alpha_m}{\delta\Delta t_n}\frac{\partial\mathbf{R}_\mathbf{u}\left(\dot{\mathbf{P}}_{n+\alpha_m},\mathbf{P}_{n+\alpha_f},\mathbf{U}_{n+1}\right)}{\partial\dot{\mathbf{P}}_{n+\alpha_m}} \\
&\quad +\alpha_f\frac{\partial\mathbf{R}_\mathbf{u}\left(\dot{\mathbf{P}}_{n+\alpha_m},\mathbf{P}_{n+\alpha_f},\mathbf{U}_{n+1}\right)}{\partial\mathbf{P}_{n+\alpha_f}}, \\
\mathbf{K}_{\mathbf{u}\mathbf{u}}\left(\dot{\mathbf{P}}_{n+\alpha_m},\mathbf{P}_{n+\alpha_f},\mathbf{U}_{n+1}\right) &:= \frac{\partial\mathbf{R}_\mathbf{u}\left(\dot{\mathbf{P}}_{n+\alpha_m},\mathbf{P}_{n+\alpha_f},\mathbf{U}_{n+1}\right)}{\partial\mathbf{U}_{n+1}}.
\end{aligned}
\tag{91}
$$

5. Solve the following linear system in the variables $\Delta\mathbf{P}_{n+1,(i)}$ and $\Delta\mathbf{U}_{n+1,(i)}$:

$$
\begin{aligned}
\mathbf{K}_{\rho\rho,(i)}\Delta\mathbf{P}_{n+1,(i)}+\mathbf{K}_{\rho\mathbf{u},(i)}\Delta\mathbf{U}_{n+1,(i)} &= -\mathbf{R}_{\rho,(i)} \\
\mathbf{K}_{\mathbf{u}\rho,(i)}\Delta\mathbf{P}_{n+1,(i)}+\mathbf{K}_{\mathbf{u}\mathbf{u},(i)}\Delta\mathbf{U}_{n+1,(i)} &= -\mathbf{R}_{\mathbf{u},(i)}.
\end{aligned}
\tag{92}
$$

6. Update the control variables:

$$
\begin{aligned}
\dot{\mathbf{P}}_{n+1,(i)} &= \dot{\mathbf{P}}_{n+1,(i-1)}+\frac{1}{\delta\Delta t_n}\Delta\mathbf{P}_{n+1,(i)}, \\
\mathbf{P}_{n+1,(i)} &= \mathbf{P}_{n+1,(i-1)}+\Delta\mathbf{P}_{n+1,(i)}, \\
\mathbf{U}_{n+1,(i)} &= \mathbf{U}_{n+1,(i-1)}+\Delta\mathbf{U}_{n+1,(i)}.
\end{aligned}
\tag{93}
$$

and return to step 1.

5.2.2 Time adaptivity

We consider an adaptive scheme similar to the one proposed in [46], which is based on the comparison of the solutions obtained with the generalized–α method and the backward Euler method [82]. The backward Euler method can be obtained by setting $\alpha_m = \alpha_f = \delta = 1$ in the generalized–α method.

The adaptive time scheme starts, for each time step t_{n+1}, $n = 0, \ldots, n_{ts} - 1$, with the given control variables $\dot{\mathbf{P}}_n$, $\mathbf{P}_n$ and $\mathbf{U}_n$, and a given time step Δt_n, typically that used at the previous time step. Then, in the adaptive algorithm the following steps are repeated for $l = 1, \ldots, l_{max}$, starting with $\Delta t_{n,(0)} = \Delta t_{n-1}$ (or, if $n = 0$, with $\Delta t_{n,(0)} = \Delta t_0$):

1. Compute the control variables $\dot{\mathbf{P}}_{n+1,(l-1)}$, $\mathbf{P}_{n+1,(l-1)}$ and $\mathbf{U}_{n+1,(l-1)}$ with the generalized–α method of Sec. 5.2.1 for $\Delta t_{n,(l-1)}$.

2. Compute the control variables $\dot{\mathbf{P}}^{BE}_{n+1,(l-1)}$, $\mathbf{P}^{BE}_{n+1,(l-1)}$ and $\mathbf{U}^{BE}_{n+1,(l-1)}$ by means of the backward Euler method for $\Delta t_{n,(l-1)}$.

3. If the generalized–α or the backward Euler methods are not converging (i.e. the predictor–multicorrector algorithm of Sec. 5.2.1 is not convergent), reduce the time step by means of a safety coefficient $\chi_{NC} \in (0, 1)$, update $\Delta t_{n,(l)}$ as:

$$\Delta t_{n,(l)} = \chi_{NC}\, \Delta t_{n,(l-1)}, \tag{94}$$

   and return to step 1; else proceed to step 4.

4. Evaluate the relative error associated to $\Delta t_{n,(l-1)}$:

$$e_{n+1,(l-1)} := \frac{\|\mathbf{P}_{n+1,(l-1)} - \mathbf{P}^{BE}_{n+1,(l-1)}\|}{\|\mathbf{P}_{n+1,(l-1)}\|} + \frac{\|\mathbf{U}_{n+1,(l-1)} - \mathbf{U}^{BE}_{n+1,(l-1)}\|}{\|\mathbf{U}_{n+1,(l-1)}\|}. \tag{95}$$

5. Update the time step size according to the following formula:

$$\Delta t_{n,(l)} = \chi_{n,(l-1)} \Delta t_{n,(l-1)}, \tag{96}$$

   where:

$$\chi_{n,(l-1)} := \min \left\{ \chi_A \left(\frac{tol_A}{e_{n+1,(l-1)}} \right)^{1/2}, 1 + \chi_{GR} \right\}, \tag{97}$$

   with tol_A a prescribed tolerance, $\chi_A \in (0, 1)$ a suitable safety coefficient and $\chi_{GR} > 0$ the maximum growth rate admitted.

6. If $e_{n+1,(l-1)} \geq tol_A$, return to step 1. Otherwise, update the control variables $\dot{\mathbf{P}}_{n+1} = \dot{\mathbf{P}}_{n+1,(l-1)}$, $\mathbf{P}_{n+1} = \mathbf{P}_{n+1,(l-1)}$, $\mathbf{U}_{n+1} = \mathbf{U}_{n+1,(l-1)}$ and the time step $\Delta t_n = \Delta t_{n,(l)}$, and exit the loop.

We observe that on the basis of the previous algorithm, one of following three situations occurs after step 6:

- if $e_{n+1,(l-1)} < \chi_A^2 tol_A$, the time step size is increased, the control variables of step 1 are considered valid and the loop ends;

- if $\chi_A^2 tol_A \leq e_{n+1,(l-1)} < tol_A$, the time step size is reduced, the control variables of step 1 are still considered valid and loop terminates;

- if $e_{n+1,(l-1)} \geq tol_A$, the time step size is reduced, the control variables of step 1 are invalid and the steps 1–6 are repeated.

Since the steps 1 and 2 are computationally expensive, the occurrence of the last case should be minimum; as pointed out in [46], this is the case if good choices for the parameters tol_A and χ_A are made.

6 Selection of Parameters

In Sec. 4.3 we provided the dimensionless form of the topology optimization problem (77), which we proposed to solve numerically by means of Isogeometric Analysis and the generalized–α method in Sec. 5. However, as already pointed out, the solution of the TO($\mathbf{D}$) problem depends on the dimensionless parameters $\mathbf{D}$, which depend on parameters $\boldsymbol{\mu} \in \mathcal{D}$ introduced in Sec. 2.2. In this section we address the issue of the choice of the parameters $\boldsymbol{\mu} \in \mathcal{D}$ and the mesh dependency effect, we select the interpolation function $g(\rho)$ (13) and the bulk energy $\psi_B(\rho)$ (16), we describe the continuation method which could be used for topology optimization in the phase field approach, and we discuss the choice of the initial solution ρ_0.

6.1 The choice of the parameters $\boldsymbol{\mu} \in \mathcal{D}$ and mesh dependency

The dimensionless parameters $\mathbf{D}$ (72) depend both on the data of the problem and the parameters $\boldsymbol{\mu} = (\lambda, \gamma) \in \mathcal{D}$; in particular, only the dimensionless parameters D_2 and D_3 and the representative time scale T_0 are related to $\boldsymbol{\mu} \in \mathcal{D}$, since we set $D_1 = 1$.

For the choice of the parameter λ we adopt similar considerations to the ones made in [46, 48]. The Cahn–Hilliard equation converges for $\lambda \to 0$ (see Eq. (30)) to a thermodynamically consistent sharp–interface model, for which the representative length scale of the interface is related to $\sqrt{\lambda}$. Similarly, for the generalized Cahn–Hilliard equation for topology optimization, the value of λ should be sufficiently small in order to provide realistic results with sharp interfaces between the material and the void. Moreover, λ is responsible for the number of holes appearing in the optimal topology, since in general it is associated with the interface energy $\psi_I(\rho)$ of Eq. (17) controlling the perimeter of the interfaces.

From a numerical point of view, we observe that the computational mesh used for the spatial approximation should be fine enough to capture the thin layers between the material and void. For these reasons, following from the dimensional considerations of Sec. 4.3, we assume that the thickness of the interfaces depends on the computational mesh and the parameter λ is chosen as [46]:

$$\lambda = \overline{\lambda}\, h^2, \tag{98}$$

where h is the characteristic length of the computational mesh, defined as:

$$h := \max_{i=1,\ldots,n_{el}} V_i^{1/d}, \tag{99}$$

with V_i the area/volume of the i–th element of the mesh composed by n_{el} elements. The parameter $\overline{\lambda}$ is dimensionless and it is chosen by the user. Indeed, it is difficult to specify at this point what value $\overline{\lambda}$ should assume since it depends in general on the data of the topology optimization problem; for example, in [46] it is shown that for the Cahn–Hilliard equation $\overline{\lambda}$ should depend on the area/volume V covered by the material in Ω.

According to this choice, the thickness of the interfaces is roughly equal to $\sqrt{\lambda} = \sqrt{\overline{\lambda}}h$, with shaper interfaces for finer meshes, which in turn allow more detailed topologies to be obtained. On the other hand, the parameter λ introduces a mesh dependency in the topology optimization problem through D_2, D_3 and T_0; this represents an undesired issue in topology optimization since the optimal distribution of the material in the design domain Ω changes with the spatial approximation used. However, in the phase field and multiphase approaches, the mesh dependency of the optimal topology could be eliminated by using a fixed value of h, say h_0, for the evaluation of the parameter λ for all the computational meshes having $h \leq h_0$.

The choice of the parameter γ is important. A value of γ that is too small will cause the objective functional to be dominated by the interface and bulk energy terms; if γ is too large, divergence may occur. The role of γ is to properly balance the strain energy function $\psi_E(\rho)$ with respect to the bulk and interface energy functions, $\psi_B(\rho)$ and $\psi_I(\rho)$, in Eq. (16). However, it is difficult to determine a priori a suitable value for γ by means of dimensional analysis; this is due to the fact that the strain energy strongly depends on data of the topology optimization problem, which are not represented by the dimensionless parameters, such as the shape of the design domain Ω and the direction of the body and surface forces $\mathbf{f}$ and $\mathbf{h}$. In [114, 115], the values differ from one test case to another; in [23, 102] the choice of γ appears to be arbitrary, while in [20] it is made by trial and error. In order to ensure a proper balance of the strain energy with respect to the other energies in (22), we propose to decompose the dimensionless parameter γ as:

$$\gamma = \overline{\gamma}\,\gamma_E, \tag{100}$$

where $\overline{\gamma}$ is a positive parameter chosen by the user and γ_E is computed from Eqs. (72) and (74) as:

$$\gamma_E = \frac{\displaystyle\int_\Omega \left(\overline{D}_2 \psi_B(\rho_0) + \psi_I(\rho_0)\right)\, d\Omega}{\displaystyle\int_\Omega \overline{D}_2 \widetilde{\psi}_E(\rho_0, \mathbf{u}(\rho_0))\, d\Omega}, \tag{101}$$

with ρ_0 the initial density, $\psi_E(\rho_0) = \widetilde{\psi}_E(\rho_0, \mathbf{u}(\rho_0))$ from Eq. (69) and, in order to make γ_E independent of $\overline{\lambda}$, from Eqs. (72) and (98) we set

$$\overline{D}_2 := \overline{\lambda} D_2 = \frac{L_o^2}{h^2}. \tag{102}$$

Finally, from Eqs. (98) and (101), we obtain from Eq. (72) that the dimensionless parameters D_2 and D_3 are:

$$D_2 = \frac{L_0^2}{\overline{\lambda} h^2}, \qquad D_3 = \overline{\gamma}\gamma_E D_2 = \overline{\gamma}\gamma_E \frac{L_0^2}{\overline{\lambda} h^2}, \tag{103}$$

while $T_0 = \dfrac{L_0^4}{\overline{\lambda} h^2 M_0}$, since we have set $D_1 = 1$.

At this point, the topology optimization problem TO($\mathbf{D}$) still depends on the arbitrary choices made for the parameters $\overline{\lambda}$ and $\overline{\gamma}$. However, numerical tests reveal that these dimensionless parameters vary in a limited range of values for different topology optimization problems; indeed, we typically select $\overline{\lambda} \in [0.5, 6.0]$ and $\overline{\gamma} \in [0.5, 4.0]$. On the other hand, these parameters allow the user to modify the outcome of the topology optimization results. In particular, the number of holes of the optimal topology can be increased or decreased by decreasing or increasing $\overline{\lambda}$, respectively.

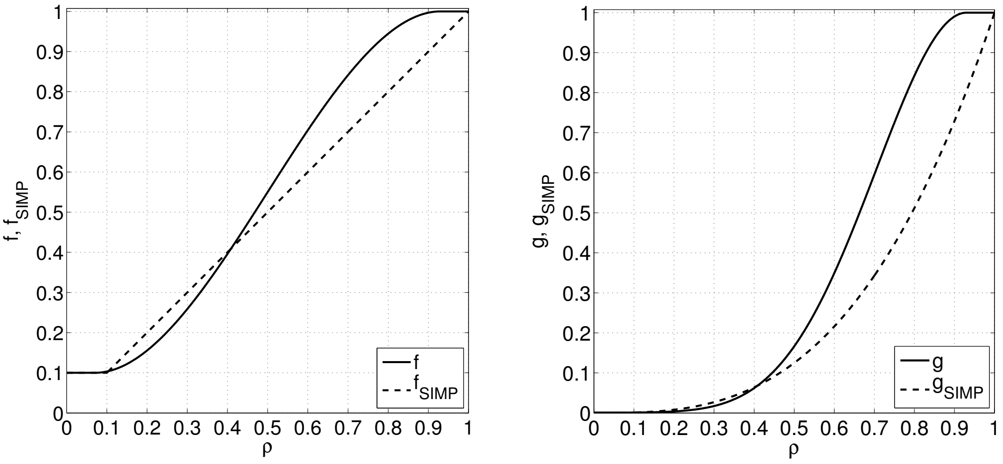

Figure 3: Functions $f(\rho)$ (—) and $f_{SIMP}(\rho)$ (- -) (left) and interpolation functions $g(\rho)$ (—) and $g_{SIMP}(\rho)$ (- -) (right).

6.2 The choice of the interpolation function $g(\rho)$ and the bulk energy function $\psi_B(\rho)$

As anticipated in Sec. 2.1 the interpolation function $g(\rho)$ is typically chosen as $g(\rho) = \rho^P$ (see Eq. (13)), with $P \geq 3$ for an isotropic material with $\nu_0 = 1/3$. We consider a similar interpolation rule which ensures that ρ exceeds a minimum value ρ_{min} and, to avoid numerical issues, the condition that the first and second derivatives of such interpolation function are zero at the pure phases 0 and 1. In particular, we consider:

$$g(\rho) = f(\rho)^P, \tag{104}$$

with $f(\rho)$ the following C^2–continuous function:

$$f(\rho) := \begin{cases} \rho_{min} & \text{if } \rho < \rho_1, \\ \rho_{min} + (1 - \rho_{min})b(\rho) & \text{if } \rho_1 \leq \rho < \rho_6, \\ 1 & \text{if } \rho \geq \rho_6, \end{cases} \tag{105}$$

and $b(\rho)$ a C^2–continuous third–degree B–spline in ρ obtained with the open knot vector $\mathcal{S} = \{\{\rho_1\}_{i=1}^4, \rho_2, \ldots, \rho_5, \{\rho_6\}_{i=1}^4\}$ and the control points $\mathcal{P} = \{0, 0, 0, 0, 1, 1, 1, 1\}$; see [80]. In Fig. 3 we compare the function $f(\rho)$ with the typical SIMP function, $f_{SIMP}(\rho)$, which is only C^0–continuous in $[0, 1]$, where:

$$f_{SIMP}(\rho) := \begin{cases} \rho_{min} & \text{if } \rho < \rho_{min}, \\ \rho & \text{if } \rho \geq \rho_{min}; \end{cases} \tag{106}$$

also, we compare the interpolation function $g(\rho)$ (104) with the SIMP function say $g_{SIMP}(\rho) = f_{SIMP}(\rho)^P$ for $P = 3$; in particular, we choose $\rho_{min} = 0.1$ and $\mathcal{S} = \{\{0.055\}_{i=1}^4, 0.065, 0.075, 0.925, 0.935, \{0.945\}_{i=1}^4\}$.

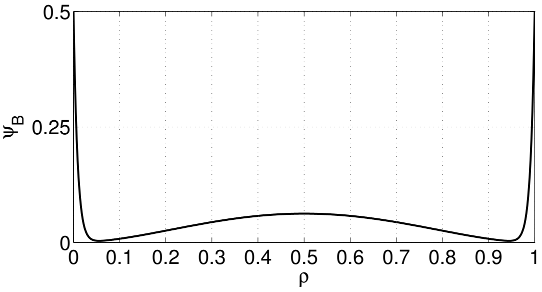

Figure 4: Bulk energy function $\psi_B(\rho)$.

For the bulk energy function $\psi_B(\rho)$ we select the following C^∞–continuous function in ρ:

$$\psi_B(\rho) = \rho^2 (1-\rho)^2 + \beta_1 \left[10^{-\beta_2 \rho} + 10^{\beta_2(\rho-1)}\right], \tag{107}$$

with β_1, $\beta_2 \in \mathbb{R}_0^+$. This choice allows naturally steep bounds on the pure phases 0 and 1 but avoids any singularities. In Fig. 4 we plot $\psi_B(\rho)$ for ρ in $[0,1]$ corresponding to the values $\beta_1 = 0.5$ and $\beta_2 = 50$, which we will select for the numerical tests.

6.3 The continuation method

In Remark 2.1 we introduced the parameter κ in view of the use of the continuation method to solve topology optimization problems in the multiphase approach as done for example in [20, 23]. This procedure can be extended to the case of the topology optimization problem in the phase field approach by following the formulation outlined in Sec. 4 with the penalized objective functional $J_\kappa(\rho;\boldsymbol{\mu}_k)$ (27). The dimensionless parameters D_1, D_2 and D_3 of Eq. (72) are modified as:

$$D_{\kappa,1} := \frac{1}{\kappa} D_1 \qquad D_{\kappa,2} := \frac{1}{\kappa^2} D_2, \qquad D_{\kappa,3} := \frac{1}{\kappa} D_3^\kappa, \tag{108}$$

for which $\mathbf{D}_\kappa := (D_{\kappa,1}, D_{\kappa,2}, D_{\kappa,3}, D_4, D_5)$ and D_3^κ can be chosen as:

$$D_3^\kappa := \gamma_\kappa D_2, \tag{109}$$

for some γ_κ, similar to Eq. (103). The characteristic time is $T_{\kappa,0} := \frac{1}{\kappa} T_0$, corresponding to the choice $D_{\kappa,1} = 1$, while the penalized objective functional scales with the quantity $\frac{1}{E_0} \frac{L_0^{2-d}}{\kappa\lambda}$.

We propose the following procedure for the continuation method:

1. set the data for the topology optimization problem;
2. choose an initial solution ρ_0 such that $\int_\Omega \rho_0 \, d\Omega = V$;
3. select the parameters $\overline{\lambda}$ and $\overline{\gamma}$ of Eqs. (98) and (100), respectively;

4. choose the computational mesh for the spatial approximation and compute h as in Eq. (103);
5. compute the parameter λ from Eq. (98) and the dimensionless parameter D_2 from Eq. (72);
6. select a discrete set $\mathbb{K}$ of values for the parameter κ, where $\mathbb{K} := \{\kappa_m\}_{m=1}^{M}$, with $\kappa_1 > \ldots > \kappa_M > 0$ and M the number of continuation levels;
7. repeat the following operations for the $m = 1, \ldots, M$ continuation levels:
    1. if $m = 1$ set $\rho_{0,h,(1)} = \rho_{0,h}$, otherwise, for $m \geq 2$, set $\rho_{0,h,(m)} = \rho_{h,(m-1)}$ for $t = T$, where $\rho_{h,(m-1)}$ is the steady state solution obtained at the continuation level $m - 1$;
    2. set $\kappa = \kappa_m$ and compute the dimensionless parameters $\mathbf{D}_{\kappa,(m)}$ from Eqs. (72), (108) and (109) for $\gamma_\kappa = \overline{\gamma}\,\gamma_{E,\kappa}$, where $\gamma_{E,\kappa}$ is computed from Eq. (101) by replacing ρ_0 with $\rho_{0,h,(m)}$ [4]; also compute $T_{\kappa,0,(m)}$;
    3. solve the $\mathrm{TO}_h(\mathbf{D}_{\kappa,(m)})$ problem (81) by using Isogeometric Analysis and the generalized–α method with the adaptive scheme outlined in Sec. 5 to obtain the steady state solution $\rho_{h,(m)}$ for $t = T$.

The choice of the set $\mathbb{K}$ is arbitrary as well as are the choices of the parameters $\overline{\lambda}$ and $\overline{\gamma}$. As a general indication, if the number of continuation levels M is too large, high computational cost is associated with the solution of the topology optimization problem with this approach. On the other hand, if M is too small or the ratios $\kappa_{m-1}/\kappa_m \gg 1$, then convergence may not occur.

The use of the continuation method allows, for a proper selection of the set $\mathbb{K}$, to use smaller values for $\overline{\lambda}$ than typically used when the $\mathrm{TO}_h(\mathbf{D})$ problem (81) is solved as a single simulation; this is due to the property of the continuation method to approach the optimal solution as a sequence of intermediate optimal results.

6.4 The choice of the initial solution ρ_0

In the phase field approach the topology optimization problem allows one to obtain the optimal solution as the steady state of the phase field model which minimizes a penalized objective functional starting from an initial solution ρ_0. In the previous sections we only required that ρ_0 satisfy the area/volume constraint, $\int_\Omega \rho_0 \, d\Omega = V$. It follows that, even with this constraint satisfied, the choice of ρ_0 is arbitrary.

Different strategies for the choice of ρ_0 have been considered in the literature, since the initial distribution of the material could largely influence the optimal topology in the minimum compliance case depending on the approach used. In general, the more ρ_0 is similar to the optimal solution, the more rapid will be the convergence of the topology optimization method; however, this situation prefigures an a priori knowledge of the optimal solution. For the SIMP approach [12] the initial solution is chosen as $\rho_0 = \rho_V$, with $\rho_V := V/|\Omega|$, even if ρ_0 often is allowed to violate the area/volume constraint, which is later restored during the optimization procedure. In the level set approach [5, 35] ρ_0 is chosen as a 0–1 distribution of material with holes such that the area/volume constraints is satisfied; the initial number of holes affects the number

---

[4] This choice allows a proper balance between the strain energy function ψ_E and the bulk and interface energies ψ_B and ψ_I through all the continuation levels.

of holes in the optimal topology and plays a crucial role in the definition of the final topology. However, it is shown in [112] by means of numerical examples that when the capability of hole nucleation is introduced in the level set method, the dependence of the optimal solution on the initial one is reduced. Initial solutions in the 0–1 configurations are also chosen in [102] for topology optimization problems formulated with the Cahn–Allen equation, which shows a strong dependence of the optimal solution on the initial one. For the phase field approach of [114, 115] using the generalized Cahn–Hilliard equation, ρ_0 is a random distribution around the average value ρ_V.

In this work, we typically choose $\rho_0 = \rho_V$. However, the continuation method of Sec. 6.2 can be effectively used to provide a suitable initial solution ρ_0 without any a priori knowledge of the optimal solution.

7 Numerical Tests

In this section we solve and discuss numerical problems in two and three–dimensions; we also highlight the features of the proposed method by means of two–dimensional tests. The numerical values considered for the numerical simulations and the implementation aspects are also reported.

7.1 Numerical values and implementation aspects

For all the simulations reported the following numerical values are considered:

- for the tensor $\mathbb{C}_0$ (see Eq. (1)), we choose $E_0 = 200 \cdot 10^9\, J/m$ and $\nu_0 = 1/3$ for the plane strain two–dimensional problems and the three–dimensional problems;
- for the representative quantities of Sec. 4.3, we choose $L_0 = 1\, m$, T_0 such that $D_1 = 1$, $M_0 = 1\, m^2/s$, $\hbar_0 = 200 \cdot 10^6\, Pa$ (for which $D_4 = 1000$) and $f_0 = 0\, N/m^3$ (no body force is considered for which $D_5 = 0$);
- the interpolation $g(\rho)$ and the bulk energy $\psi_B(\rho)$ functions are chosen as in Sec. 6.2 with $P = 3$ and the mobility is assumed constant, $M(\rho) = M_0$.

For the numerical approximation we consider:

- for the Isogeometric spatial approximation of Sec. 5.1, we choose a NURBS (or B–splines) basis of degree $p = 2$ and numerical integration is performed using 3×3 Gauss quadrature ($3 \times 3 \times 3$ in three–dimensional problems); this represents a very conservative approach. The study of more efficient quadrature schemes for NURBS was initiated in [56]; further investigations are ongoing;
- for the time step scheme of Sec. 5.2.1 we choose $\rho_\infty = 1/2$ (for which $\alpha_m = 5/6$, $\alpha_f = 2/3$ and $\delta = 2/3$ from Eq. (85)), with the tolerance for the stopping criterion (89) $tol_R = 10^{-4}$ and the maximum number of steps set equal to $i_{max} = 7$;
- for the time adaptivity of Sec. 5.2.2 we select the initial time step $\Delta t_0 = 10^{-12}$ and the final time $T = 10^2$, $\chi_{NC} = 0.5$ in Eq. (94) to reduce the time step in case of divergence of the generalized–α or backward Euler methods, and $\chi_A = 0.85$, $\chi_{GR} = 1.2$ and $tol_A = 10^{-3}$ in Eq. (97) for the time update and stopping criterion;

- the numerical solution of the spatial approximation is obtained by using the Bézier extraction methods presented in [17] (Bézier extraction provides a localized representation of the globally smooth basis that can be implemented in shape function routines in existing finite element codes);

- the problem is solved using a parallel C++ code based on Trilinos [53] and MPI;

- the linear system (92) is solved with the "monolithic" approach by means of the GMRES method preconditioned by an Algebraic Multigrid strategy with Smoothed Aggregation [44]; the dimension of the Krilov space is set equal to 700–1,000 and the stopping criterion is based on the relative residual with tolerance equal to 10^{-6} [5].

Remark 7.1 *The solution of the linear system (92) is particularly challenging for fine meshes, especially for three–dimensional problems; this is due to the nature of the block matrices involved in the global matrix. Indeed, the matrix* $\mathbf{K}_{\rho\rho,(i)}$ *radically changes behavior as time evolves: when* Δt *is small, far from the steady state, the mass matrix dominates over the fourth–order stiffness matrix in* $\mathbf{K}_{\rho\rho,(i)}$ *and convergence occurs in a relatively small number of GMRES steps. On the contrary, when* Δt *is large, many more steps are required. The block matrix* $\mathbf{K}_{\mathbf{uu},(i)}$ *represents the stiffness matrix of the linear elastic problem, with elastic properties depending on the distribution of the phase variable* ρ*; see Eqs. (1) and (104). The properties of such a matrix abruptly change when passing through the interfaces and GMRES could suffer divergence issues when sharp interfaces are generated, especially in the parallel setting. If necessary, a way to partially overcome this inconvenience consists of enforcing the development of the interfaces over a sufficiently high number of mesh elements by suitably tuning the parameter* $\overline{\lambda}$ *(98). Additionally, the off–diagonal block matrices* $\mathbf{K}_{\rho\mathbf{u},(i)}$ *and* $\mathbf{K}_{\mathbf{u}\rho,(i)}$ *could further degrade the conditioning properties by rendering the full matrix "less symmetric." We believe that an ad hoc preconditioner should be developed to take into account all these features while solving the linear system in the "monolithic" approach; we notice that this could be required even if the system (92) is eventually solved with a "staggered" approach. This was not pursued in the present work.*

On the basis of the parameters above mentioned, a typical two–dimensional simulation with a mesh with 320 × 160 elements converges in about $n_{ts} = 1,000$–$1,200$ time steps; time adaptivity converges in one iteration with few exceptions for a limited number of time steps (typically only 1–10). In each time step the generalized–α method typically converges in one to four Newton iterations (likewise for the backward Euler method) and no, or a few, restarts with forced reduction of the time step are required due to divergence. For the same simulation, the solution of the linear system (92) requires a number of GMRES iterations comprised between 7 and 500 depending on the time step Δt and time t. In general, the smaller is the thickness of the interface for a given mesh (related to the parameter $\overline{\lambda}$ of Eq. (98)) and/or the larger the parameter $\overline{\gamma}$ of Eq. (100), the slower is the convergence of the simulation to the steady state solution; indeed, in these cases, we could incur a large number of time steps and time step

---

[5] When the norm of the residual associated to the solution of the linear system is below the 10^{-5} threshold, we progressively increase the tolerance on the relative residual. This situation occurs for "large" Δt, which in turn occurs in proximity of the steady state solution, i.e. when the solution of the problem at the previous time step yields a very small residual in the linear system at the current time step. In this case, a fixed tolerance on the relative residual would be too restrictive and would lead to an unnecessary large number of GMRES iterations.

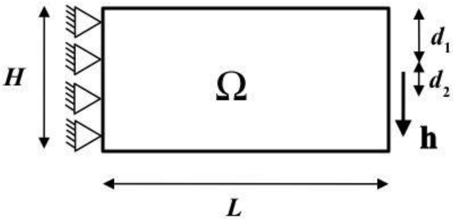

Figure 5: Test 1. Design domain Ω, surface force $\mathbf{h}$ and displacement constraints.

adaptions, and a large number of Newton iterations in the generalized–α and backward Euler methods and, consequently, slow convergence of the GMRES linear solver.

7.2 Two–dimensional problems

We discuss two–dimensional topology optimization problems in order to highlight the features and properties of the method. We consider design domains represented by B–splines and NURBS bases.

7.2.1 Test 1

The topology optimization problem for Test 1 is represented in Fig. 5. We consider a rectangular design domain Ω with zero displacement boundary conditions on the left edge and the vertical traction $\mathbf{h} = -\hbar_0 \hat{\mathbf{n}}$ acting on the d_2–part of the right edge. We assume $L = 2.00\,m$, $H = 1.00\,m$, $d_1 = 0.45\,m$ and $d_2 = 0.10\,m$. The fraction of the volume of Ω to be covered by the material is $V/|\Omega| = 0.35$. The design domain Ω is represented with a B–spline basis with the control points such that there is a linear mapping between the parametric domain and Ω.

For the numerical solution of the problem we consider a mesh with 320×160 elements, for which the dimensionless mesh size is $h = 0.00625$. Also, we select the parameters $\overline{\lambda} = 6.0$ and $\overline{\gamma} = 1.0$ for the definition of the dimensionless parameters D_2 and D_3 (see Eqs. (98), (100) and (103)); the parameter $\gamma_E = 1.247 \cdot 10^4$ is selected from Eq. (101). The dimensionless parameters are $D_2 = 4.267 \cdot 10^3$ and $D_3 = 5.322 \cdot 10^7$, with the characteristic time $T_0 = 4.267 \cdot 10^3$. We indicate this problem as Test 1.1. In Fig. 6 we present the evolution of the phase (material density) variable ρ by showing it at significant time steps; the initial solution is set as $\rho_0 = \rho_V = V/|\Omega|$. The color scale is from blue to red for values of ρ from 0 to 1. As we can deduce from Fig. 7(left), the distribution of the material is driven at the initial steps by the above–average values of the strain energy function ψ_E; in this case, the material is distributed around the Γ_D boundary and where the load $\mathbf{h}$ is applied. The phase separation occurring in these areas of the design domain is due to the generalized Cahn–Hilliard model which is mass/volume conservative. As time evolves, the separation of the phases is mostly completed and the structure tends to simplify; this is due to the fact that the bulk, interface and strain energies (i.e., J_B, J_I and J_E, respectively) are all contributing to the minimization of the objective functional J (see Eqs. (18) and (24)). The steady state represents the optimal topology in terms of the objective functional J, which reaches its minimum with respect to the initial value (for $\rho = \rho_0$ at $t = 0$); it is also possible

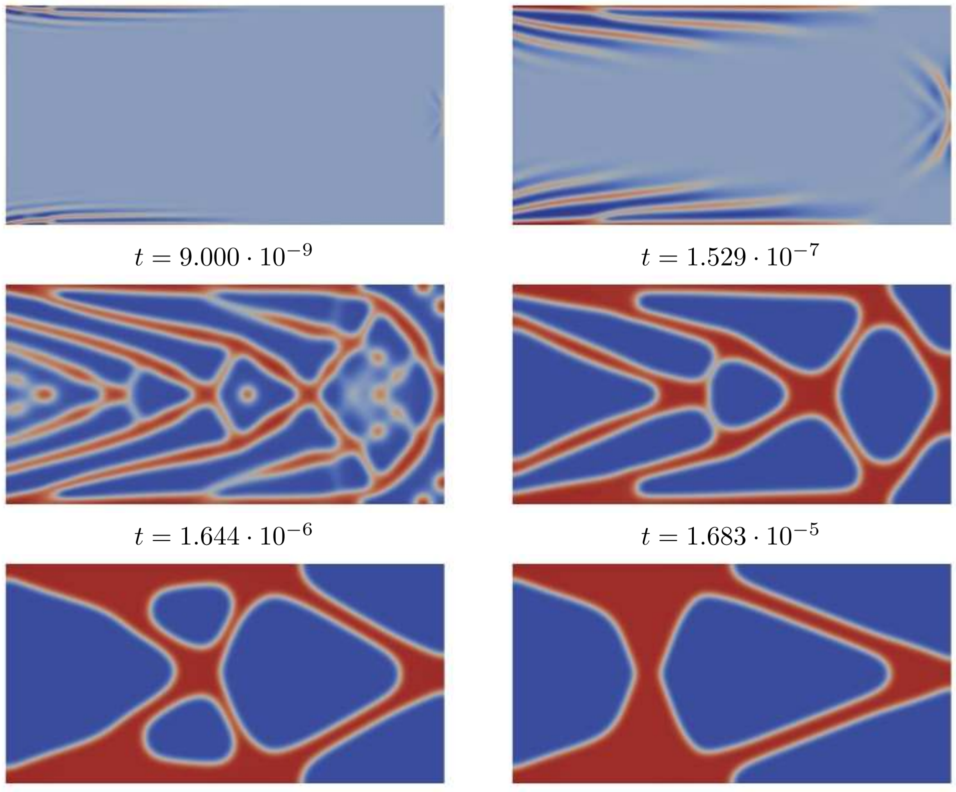

$t = 9.000 \cdot 10^{-9}$ $t = 1.529 \cdot 10^{-7}$

$t = 1.644 \cdot 10^{-6}$ $t = 1.683 \cdot 10^{-5}$

$t = 6.528 \cdot 10^{-4}$ (minimum J_E) steady state

Figure 6: Test 1.1. Evolution of the phase (material density) variable ρ in time for mesh size 320×160 with $\overline{\lambda} = 6.0$ and $\overline{\gamma} = 1.0$.

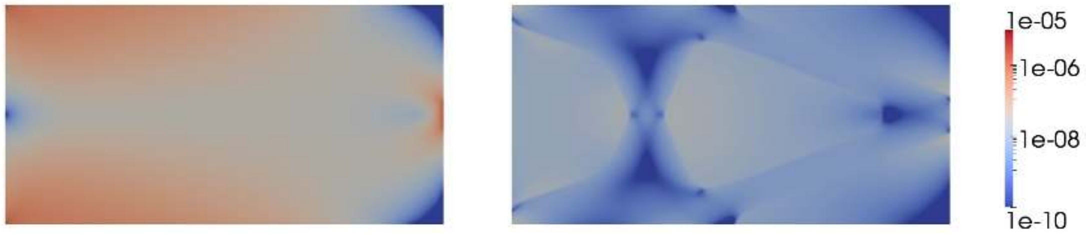

$t = 0$ steady state

Figure 7: Test 1.1. Distribution of the strain energy function ψ_E (dimensionless) in the design domain Ω (initial and at the steady state); logarithm scale.

to see from Fig. 7(right) that the average value of the strain energy function ψ_E is also much lower at the steady state. However, the optimal topology at the steady state does not necessarily represents the stiffest structure with the specified data; indeed, as is occurring in this case, the minimum value of J_E is obtained at an intermediate step and before the steady state is reached. This fact is highlighted in Fig. 8 where the

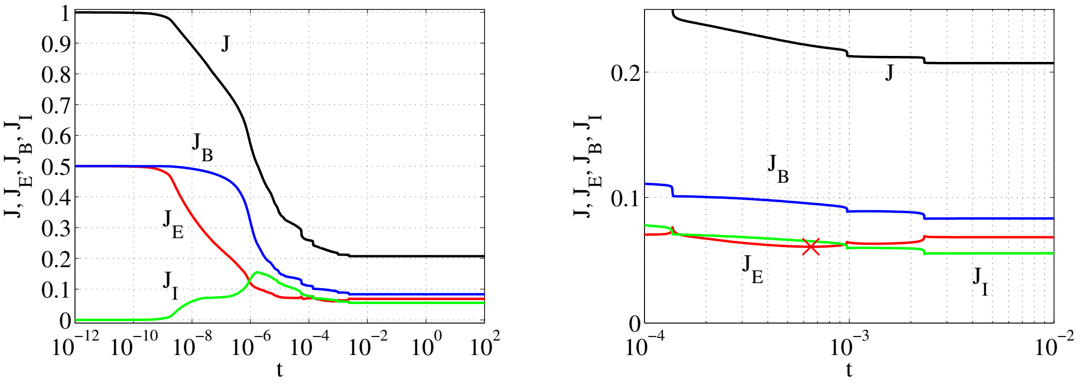

Figure 8: Test 1.1. Normalized energies J (black), J_E (red), J_B (blue) and J_I (green) vs. time t (left) and detail (right); the minimum value of J_E is indicated by an ×.

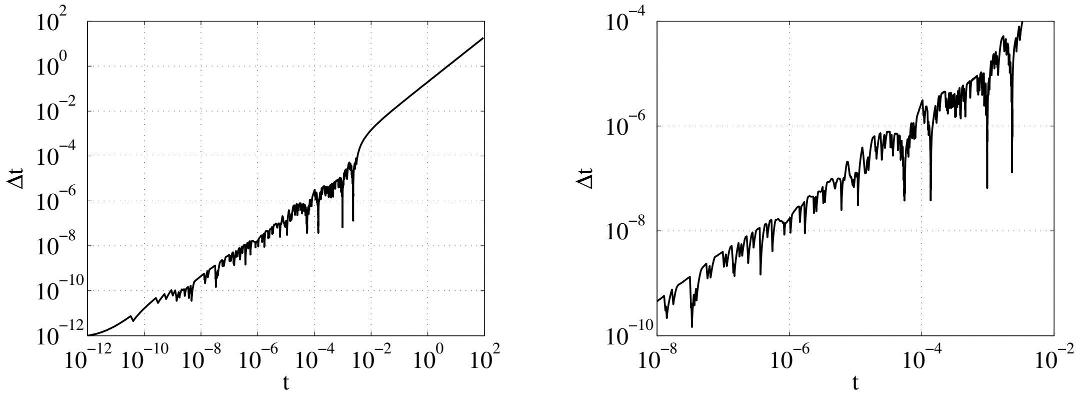

Figure 9: Test 1.1. Time step Δt vs. time t (dimensionless) as selected by the adaptive time scheme (left) and detail (right).

behavior of the objective functional J and the energies J_E, J_B and J_I is plotted vs. the dimensionless time t. The objective functional J is monotonically decreasing in time as expected since it is a Liapunov functional (see Eq. (61)), even if this property does not hold for the energies J_E, J_B and J_I. The large drop of J_B is due to the phase separation and the evolution of J_I to the creation of the interfaces and the following simplification of the topology during the evolution in time. The strain energy J_E is also subject to a large and desired drop, even if its minimum value is reached at an intermediate step. In particular, we obtain that the initial value of the objective functional J decreases by 79.29% at the steady state, while J_E decreases by 86.33%; the minimum value of J_E, representing the real goal of the topology optimization is obtained at $t = 6.528 \cdot 10^{-4}$ with a drop of 87.84%; this represents a significant value smaller by 11.05% with respect to the one reached at the steady state. The topologies of these configurations are radically different; consequently, we can select the configuration for which J_E is minimum as the optimal topology from a design point of view. The geometrical information can be

$\overline{\lambda} = 12.0$, $\overline{\gamma} = 1.0$ $\overline{\lambda} = 6.0$, $\overline{\gamma} = 0.2$

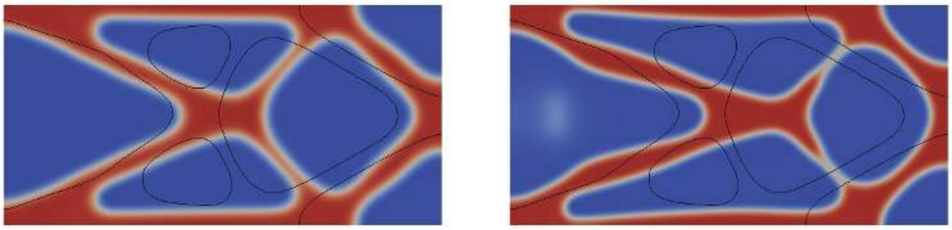

minimum J_E minimum J_E

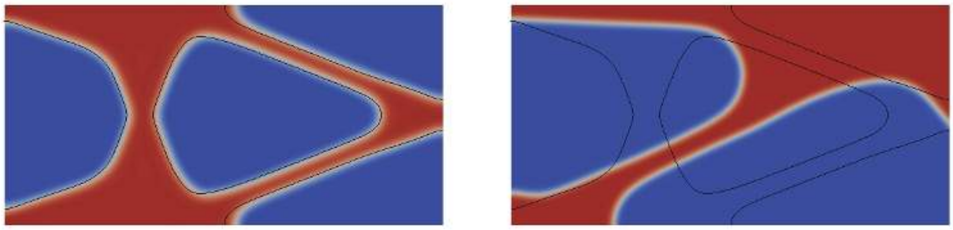

steady state steady state

Figure 10: Test 1.2. Phase (material density) variable ρ for mesh size 320×160 with $\overline{\lambda} = 12.0$ and $\overline{\gamma} = 1.0$ (left) and $\overline{\lambda} = 6.0$ and $\overline{\gamma} = 0.2$ (right); solutions for minimum value of J_E (top) and at the steady state (bottom). The contour lines represent the topologies obtained in Test 1.1 for $\overline{\lambda} = 6.0$ and $\overline{\gamma} = 1.0$.

extracted from the solution by the contour lines corresponding to the value $\rho = 0.5$. In Fig. 9 we show the evolution of the time step Δt_n vs. time t, which is chosen adaptively according to the scheme presented in Sec. 5.2.2. We observe the large change in the value of Δt_n from 10^{-12} to 18.8 occurring in a relatively small number of time steps, 1, 198 in this case; also, we observe how the intermittent nature of the phase field model is apparent in the drop of the value of Δt_n required at some times steps. As a final consideration regarding the numerical scheme, we observe that the mass/volume constraint is adequately satisfied during the evolution in time, since the relative error with respect to the initial value of the volume fraction is practically negligible and below the $4.90 \cdot 10^{-6}\%$ threshold for all the time steps.

Finally, we discuss the results of the topology optimization for different values of the parameters $\overline{\lambda}$ and $\overline{\gamma}$ with respect to the ones previously selected; this test is referred to as Test 1.2. The goal is to show that a large value of $\overline{\lambda}$ leads to optimal topologies with large interfaces and eventually to reduced minimizations of the strain energy J_E. Similarly, if the value of $\overline{\gamma}$ is too small, the phase transition leads to solutions principally driven by the Cahn–Hilliard terms, the reduction of J_E would be limited in this case and the topology would have few or no holes. Ideally, as discussed in Sec. 6.1, one would select the smallest possible value of $\overline{\lambda}$ and the largest of $\overline{\gamma}$ which would lead to the steady state without the occurrence of divergence issues [6]. In Fig. 10(left) we present the topologies corresponding to the minimum value of J_E (top) and to the steady state (bottom) for the parameters $\overline{\lambda} = 12.0$ (twice that for Test 1.1) and $\overline{\gamma} = 1.0$; the contour lines for

---

[6] Divergence issues are revealed in the current numerical setting by increasing values in time of the Liapunov objective functional J or by the recursive selection of excessively small values of the adaptive time step Δt_n.

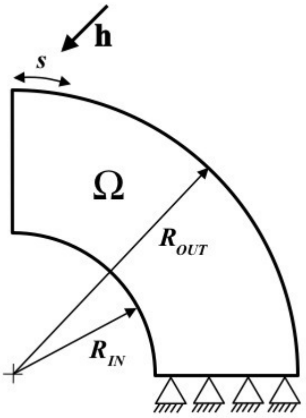

Figure 11: Test 2. Design domain Ω, surface force $\mathbf{h}$ and displacement constraints.

$\rho = 0.5$ of the solutions of Test 1.1 are highlighted. We can observe larger interfaces with respect to the previous case (about $\sqrt{2}$ larger) and, even if the configuration at the steady state is very similar to the one of Test 1.1, the decrease in the values of J and J_E is significantly different. Indeed, the drops of J and J_E at the steady state are 74.71% and 85.27%, respectively (for Test 1.1 they were 79.29% and 86.33%); at its minimum, the drop of the strain energy J_E is 86.61%, a value larger by 10.12% with respect to the one obtained in Test 1.1. Even more significant differences can be obtained for larger values of the parameter $\overline{\lambda}$. In Fig. 10(right) we highlight the topologies obtained with the parameters $\overline{\lambda} = 6.0$ and $\overline{\gamma} = 0.2$ (1/5 of Test 1.1); the configurations corresponding to the minimum value of J_E and at the steady state are presented together with the contour lines for $\rho = 0.5$ corresponding to Test 1.1. The thickness of the interfaces between the phases is the same as in Test 1.1, even if the topologies exhibit significant changes. Also, the relatively "small" value of $\overline{\gamma}$ leads to a nonsymmetric solution at the steady state since the symmetric configuration is unstable from the point of view of the phase field problem (a bifurcation from a symmetric configuration occurs during the phase transition). The decrease of J and J_E at the steady state are 79.62% and 80.21%, respectively, with the value of J_E being 34.35% larger than in Test 1.1; similarly, the drop of J_E at its minimum is 83.05%, 39.39% larger than in Test 1.1. Notice that in the limit case $\overline{\gamma} = 0.0$, the solution coincides with the Cahn–Hilliard one, which in this case exhibits a topology with a vertical rectangle.

7.2.2 Test 2

For Test 2, we consider a quarter ring with inner radius $R_{IN} = 1.00\,m$ and outer radius $R_{OUT} = 2.00\,m$ as shown in Fig. 11. The surface force $\mathbf{h}$ is applied at the top–left tip of the design domain Ω along a boundary segment of length $s = \pi/10\,m$; no displacement boundary conditions are applied at the bottom of Ω. The volume fraction of Ω to be occupied by the material is set equal to $V/|\Omega| = 0.35$. We represent the design domain Ω by means of a NURBS basis of degree 2 [80] for which, by using Isogeometric Analysis, the exact representation of the geometry is maintained through the analysis and the topology optimization procedure.

We solve the topology optimization problem with a mesh composed by 320×160

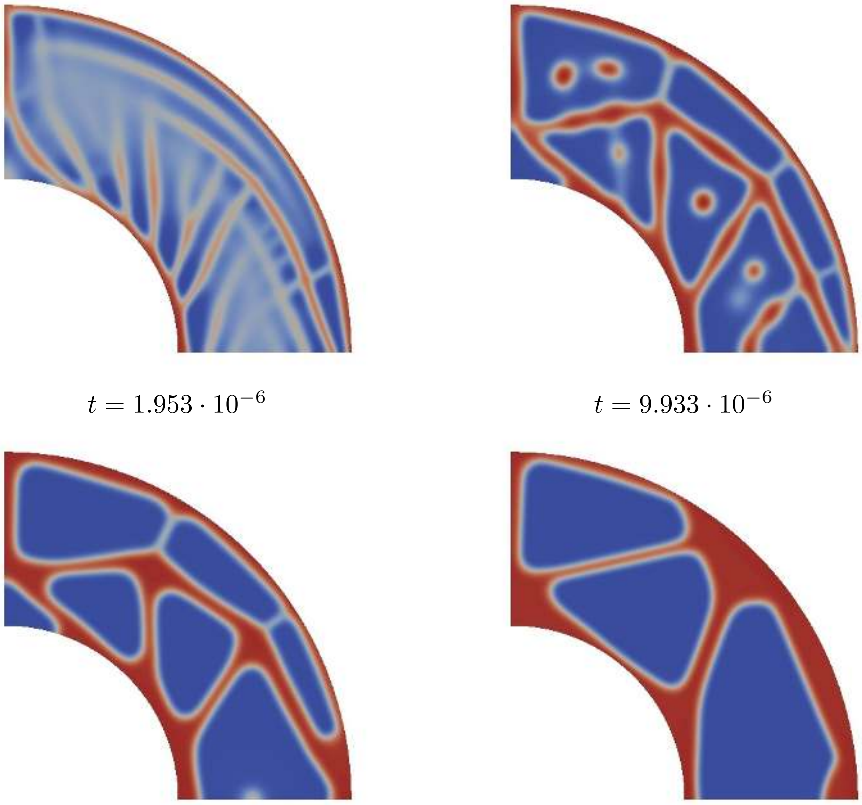

$t = 1.953 \cdot 10^{-6}$

$t = 9.933 \cdot 10^{-6}$

$t = 5.420 \cdot 10^{-5}$ (minimum J_E)

steady state

Figure 12: Test 2.1. Evolution of the phase (material density) variable ρ in time for mesh size 320×160 with $\overline{\lambda} = 5.0$ and $\overline{\gamma} = 1.5$.

elements with the larger number along the circumferential direction; the dimensionless mesh dimension is $h = 9.818 \cdot 10^{-3}$. We select the parameters $\overline{\lambda} = 5.0$ and $\overline{\gamma} = 1.5$, for which we have $D_2 = 2.075 \cdot 10^3$ and $D_3 = 2.275 \cdot 10^7$ with the computed $\gamma_E = 7.309 \cdot 10^3$. We indicate this test as Test 2.1. In Fig. 12 we present the evolution in time of the material density starting from the initial solution $\rho_0 = \rho_V = V/|\Omega|$ toward the steady state; intermediate significant solutions are presented, including the one corresponding to the minimum value of the strain energy J_E. We observe that, even if such solution does not exhibit a complete phase separation, useful topological information can still be obtained and the configuration can be used for further design investigation. In Fig. 13 we highlight the behavior of the objective functional J and the energies J_E, J_B and J_I vs. the time; a detailed view around the minimum value of J_E is also presented. The decrease of the value of J is 75.56% at the steady state, while for J_E it is 84.35%; at its minimum, which occurs at $t = 5.420 \cdot 10^{-5}$ (dimensionless), the decrease of J_E is 86.25%, 12.12% smaller than at the steady state.

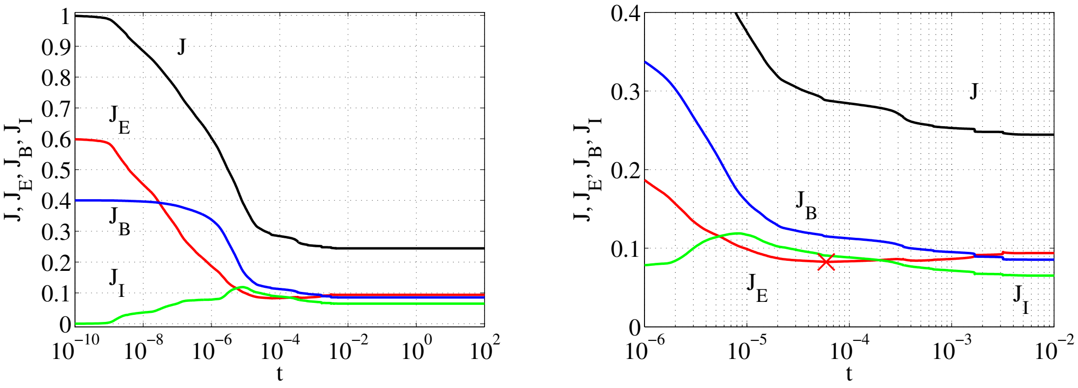

Figure 13: Test 2.1. Normalized energies J (black), J_E (red), J_B (blue) and J_I (green) vs. time t (left) and detail (right); the minimum value of J_E is indicated by an $\times$.

We now discuss the mesh dependency effect in Test 2.2. With this aim, we solve the same problem discussed previously with different mesh sizes and values of the parameter λ affecting the dimensionless parameters D_2 and D_3 (see Eq. (72)). If the goal of the topology optimization is to obtain sharp interfaces and detailed optimal topologies, fine meshes need to be used since, from Eq. (98), the parameter λ is selected as $\lambda = \overline{\lambda} h^2$, with h indicative of the mesh size. However, as already mentioned in Sec. 6.1, this introduces a mesh dependency effect on the solution, since the dimensionless parameters D_2 and D_3 vary with the mesh. On the other hand, the mesh dependency issue can be quickly eliminated in the phase field approach by using a fixed value of $h = h_0$ for all the meshes having $h \leq h_0$. In Fig. 14(right) we show the optimal topologies obtained at the steady states for different mesh sizes (80×40, 160×80 and 320×160) for $\overline{\lambda} = 5.0$ and $\overline{\gamma} = 1.5$; once h_0 is set to be the representative dimensionless size of the mesh 80×40 ($h_0 = 0.03927$), we select $h = h_0, h_0/2, h_0/4$ for the three meshes, respectively. In this case, we observe that, not only does the thickness of the interfaces change from one mesh to the other, but also the optimal topologies significantly vary. Conversely, if we assume a constant value of $h = h_0$ for all the meshes, the thickness of the interfaces between the phases and the optimal topologies remain the same; see Fig. 14(left) where we considered $\overline{\lambda} = 1.0$ and $\overline{\gamma} = 2.0$ to show shaper interfaces (the same result of Fig. 14(top–right) would have been obtained for all three meshes with $\overline{\lambda} = 5.0$ and $\overline{\gamma} = 1.5$). These facts are better highlighted in Fig. 15 in terms of the behavior of the objective functional J and strain energy J_E for the three meshes with and without a fixed value of h. As we can observe in Fig. 15(left) the choice of a fixed $h = h_0$ leads to a good match between the energies for all the meshes, with only minor differences; at the steady state the maximum discrepancy on J with respect to the finer mesh is 0.03630%, and 0.4021% for J_E. On the contrary, the mesh dependency effect is clearly visible in Fig. 15(right) with the mesh dependent $h = h_0, h_0/2, h_0/4$. Additionally, we observe that the finer meshes allow a more significant reduction of the objective functional J and strain energy J_E with respect to the coarse one, due to the ability to deal with sharper interfaces. In particular, the reduction of J at the steady state is 51.56%, 67.93% and 75.56% for the three meshes, while for J_E it is 77.73%, 83.63% and 84.35%; at their minimum the reductions of J_E are 78.46%, 83.79% and 86.25%, with the maximum stiffness obtained

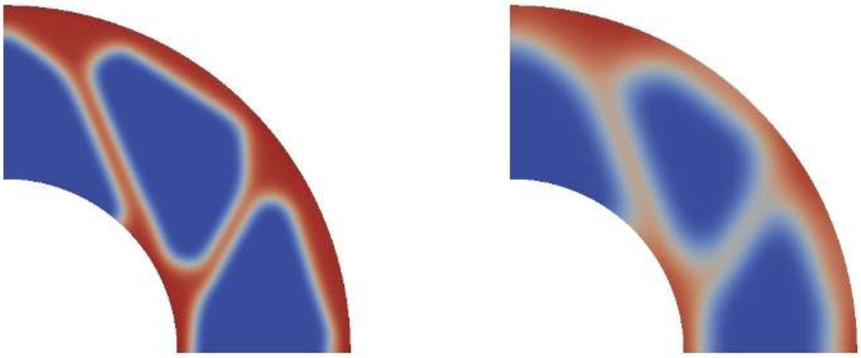

mesh 80×40, $h = h_0$ mesh 80×40, $h = h_0$

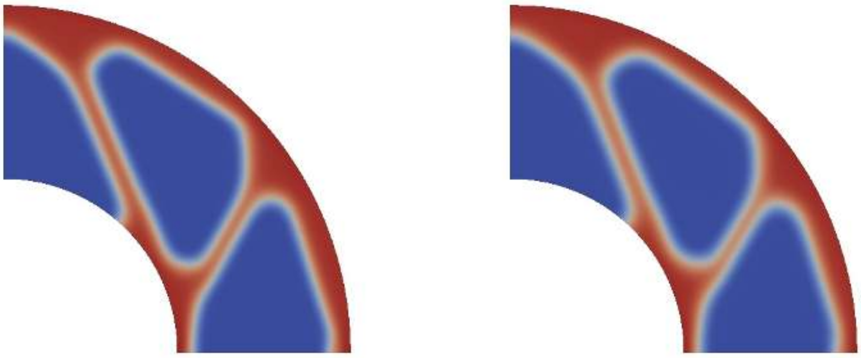

mesh 160×80, $h = h_0$ mesh 160×80, $h = h_0/2$

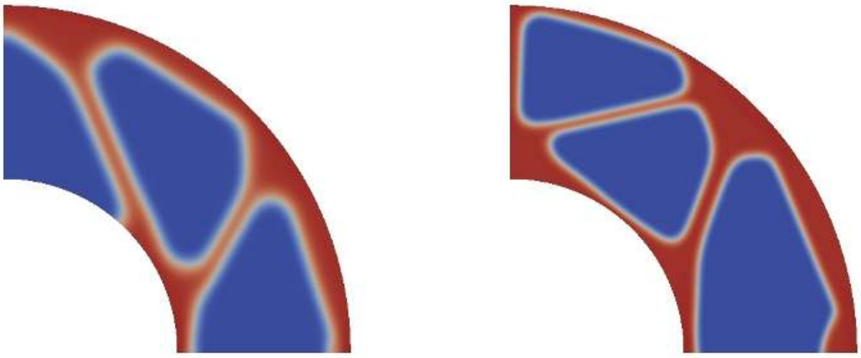

mesh 320×160, $h = h_0$ mesh 320×160, $h = h_0/4$

Figure 14: Test 2.2. Steady states of the phase (material density) variable ρ for the mesh sizes 80×40, 160×80 and 320×160 with fixed $h = h_0$ ($\overline{\lambda} = 1.0$, $\overline{\gamma} = 2.0$) (left) and with mesh dependent $h = h_0$, $h_0/2$ and $h_0/4$ ($\overline{\lambda} = 5.0$, $\overline{\gamma} = 1.5$) (right); $h_0 = 0.03925$.

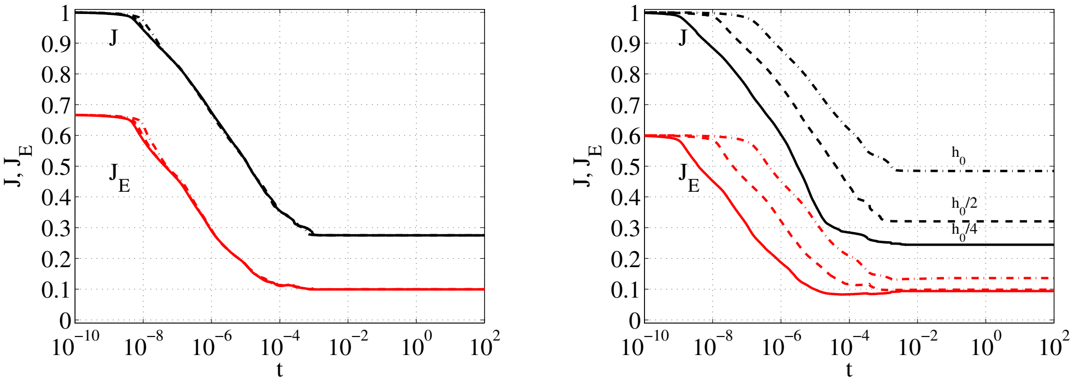

Figure 15: Test 2.2. Normalized energies J (black) and J_E (red) vs. time t for the mesh sizes 80×40 (− ·), 160×80 (− −) and 320×160 (—) for fixed $h = h_0$ ($\overline{\lambda} = 1.0$, $\overline{\gamma} = 2.0$) (left) and mesh dependent $h = h_0$, $h_0/2$ and $h_0/4$ ($\overline{\lambda} = 5.0$, $\overline{\gamma} = 1.5$) (right).

with the finer mesh.

Finally, we solve the topology optimization problem by means of the continuation method described in Sec. 6.3; the goal is to show that this approach can be conveniently used to generate solutions with sharp interfaces even if a coarse mesh is used. We refer to this problem as Test 2.3. With this aim, we consider a mesh of size 80×40 (dimensionless $h = 0.03927$ from Eq. (99)) with a two–level continuation procedure for which the parameters κ are chosen as $\kappa \in \mathbb{K} = \{4.0, 1.0\}$; additionally, we select $\overline{\lambda} = 1.0$ and $\overline{\gamma} = 4.0$ (see Eqs. (98) and (100)). The resulting dimensionless parameters (108) are: $D_{\kappa,2} = 4.053 \cdot 10^1$ and $D_{\kappa,3} = 4.742 \cdot 10^6$, with $\gamma_{E,\kappa} = 7.313 \cdot 10^3$, for continuation level 1, and $D_{\kappa,2} = 6.485 \cdot 10^2$ and $D_{\kappa,3} = 7.544 \cdot 10^7$, with $\gamma_{E,\kappa} = 2.907 \cdot 10^4$, for level 2. In Fig. 16 we present the result of the topology optimization with the two–level continuation method in which we highlight the steady states as well as the solution at significant time steps for levels 1 and 2; the optimal topology is represented by the steady state of level 2. The evolution of the normalized energy J in time t (dimensionless) is presented in Fig. 17 for the two levels. The total and elastic energies decrease 72.16% and 82.09% for continuation level 1, and 27.68% and 35.64% for level 2; for the whole procedure, the decrease of J and J_E with respect to the values corresponding to the initial solution $\rho_0 = \rho_V$ is 79.87% and 88.47%, respectively. For comparison, we observe that divergence issues appear for the topology optimization of the current test without the continuation method for $\overline{\lambda} = 1.0$ and $\overline{\gamma} = 4.0$ (the same values used for the continuation method with $D_2 = D_{\kappa,2}$ for $\kappa = 1.0$). It follows that in order to maintain the same thickness of the interfaces of the solution as for the continuation method, the value of $\overline{\gamma}$ would need to be lowered (the value $\overline{\gamma} = 2.0$ would suffice for the current mesh), even if the reduction of J_E would be smaller than with the continuation method.

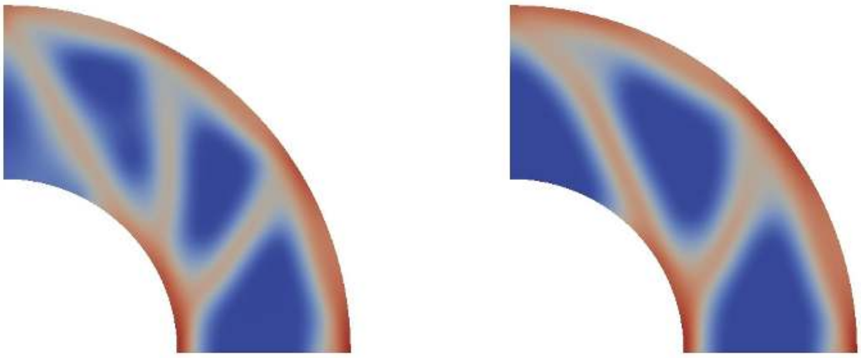

Level 1, $t = 2.935 \cdot 10^{-3}$

Level 1, steady state

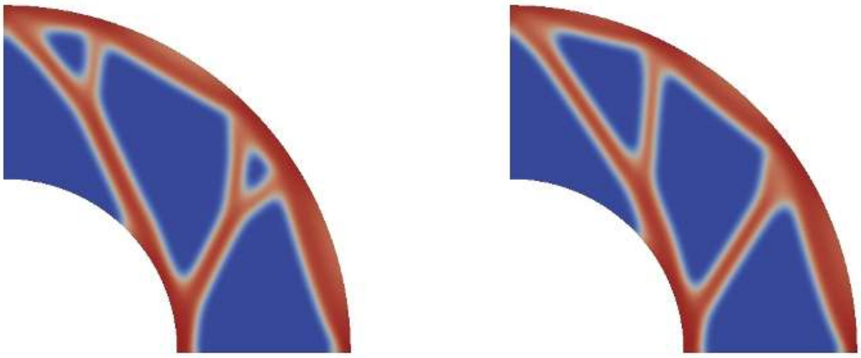

Level 2, $t = 2.070 \cdot 10^{-5}$

Level 2, steady state

Figure 16: Test 2.3. Evolution of the phase (material density) variable ρ in time t for mesh size 80×40 with the continuation method for $\mathbb{K} = \{4.0, 1.0\}$, $\overline{\lambda} = 1.0$ and $\overline{\gamma} = 4.0$; continuation levels 1 (top) and 2 (bottom) with steady states (right).

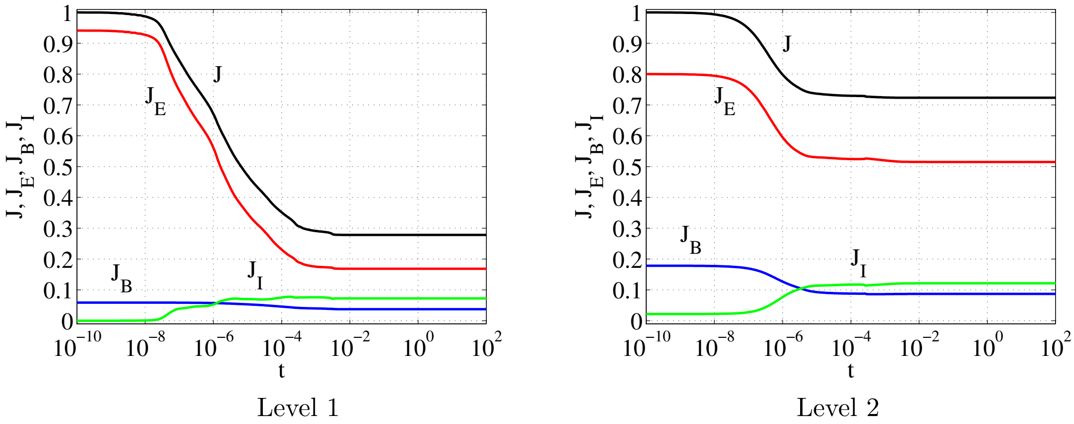

Figure 17: Test 2.3. Normalized energies J (black), J_E (red), J_B (blue) and J_I (green) vs. time t for the continuation method at levels 1 (left) and 2 (right).

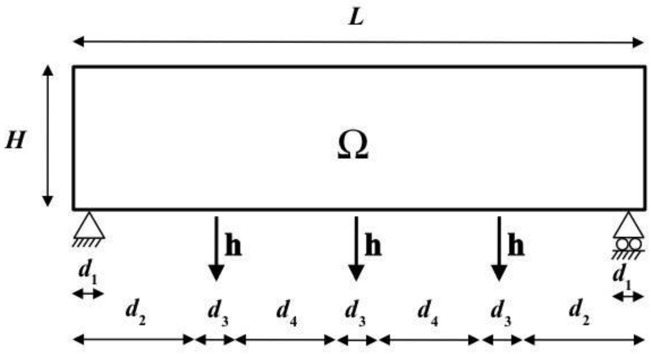

Figure 18: Test 3. Design domain Ω, surface force $\mathbf{h}$ and displacement constraints.

7.2.3 Test 3

For this test case, we consider the topology optimization problem depicted in Fig. 18. The surface forces, $\mathbf{h}$, are applied over segments of the boundary of length d_3. We enforce zero displacement condition on a segment of the boundary on the left end of the bottom edge and we fix the vertical displacement over a segment on the right end of the bottom edge [7]. We assume $L = 4.00\,m$, $H = 1.00\,m$, $d_1 = 0.125\,m$, $d_2 = 0.9375\,m$, $d_3 = 0.125\,m$ and $d_4 = 0.875\,m$; the volume fraction to be occupied by the material is $V/|\Omega| = 0.40$. The design domain Ω is represented by means of a B–spline basis of degree 2 with a linear mapping.

With this test problem, we discuss the solution of topology optimization problems in the presence of local peak values of the strain energy function ψ_E inside the design

---

[7] In the framework of Isogeometric analysis, we impose the displacement constraints on the degrees of freedom corresponding to the control points on the Dirichlet boundary segments Γ_D.

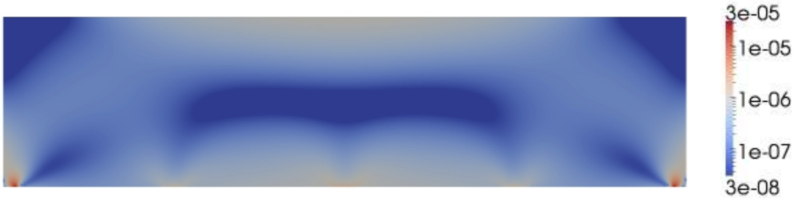

Figure 19: Test 3. Distribution of the strain energy function ψ_E (dimensionless) in the design domain Ω at $t = 0$ for $\rho_0 = \rho_V$ with mesh size 128×80; logarithm scale.

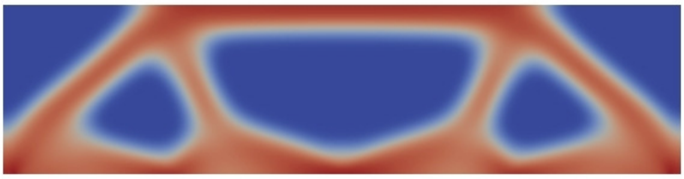

Level 1, steady state

Level 2, steady state

Figure 20: Test 3.1. Evolution of the phase (material density) variable ρ in time t with the continuation method for $\mathbb{K} = \{8.0, 1.0\}$, $\overline{\lambda} = 2.0$ and $\overline{\gamma} = 1.0$; continuation levels 1 (top) and 2 (bottom) at the steady states.

domain. An example is highlighted in Fig. 19, where the distribution of ψ_E is shown for this test problem at the initial step ($\rho_0 = \rho_V = V/|\Omega|$). In such cases, the phase separation is rapid and locally driven by such peak values and convergence may not occur if the values of the parameter $\overline{\gamma}$ are too "large" and/or those of the parameter $\overline{\lambda}$ are too "small." However, since the goal is to obtain a significant reduction of the strain energy J_E with sharp interfaces, the choice of the parameters cannot be excessively limited by such issues. In practice, "small" values of $\overline{\gamma}$ and "large" values of $\overline{\lambda}$ should be chosen at the early stages of the phase transition and modified during its evolution. However, we realize that this procedure needs to be calibrated for each topology optimization problem. In order to overcome this deficiency, we propose two approaches. The first one consists in using the continuation method, while the second one considers an initial phase (material) distribution ρ_0 in which "bubbles" of material are located ab initio in correspondence with peak values of the strain energy function ψ_E. The mesh size chosen for the simulations is 512×128 and $h = 0.007813$.

In Fig. 20 we present the solution of the topology optimization problem using the continuation method; the two steady state solutions, corresponding to the values $\kappa =$

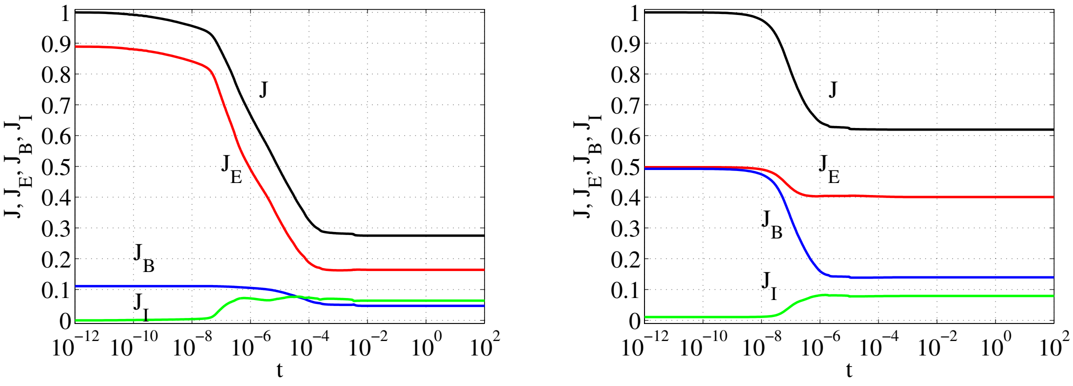

Level 1

Level 2

Figure 21: Test 3.1. Normalized energies J (black), J_E (red), J_B (blue) and J_I (green) vs. time t for the continuation method at levels 1 (left) and 2 (right).

$\{8.0, 1.0\}$, are presented. For this simulation, which we indicate as Test 3.1, we choose $\overline{\lambda} = 2.0$ and $\overline{\gamma} = 1.0$. We obtain the following dimensionless parameters from Eq. (108): $D_{\kappa,2} = 1.280 \cdot 10^2$ and $D_{\kappa,3} = 1.074 \cdot 10^7$, with $\gamma_{E,\kappa} = 1.049 \cdot 10^4$, for continuation level 1, and $D_{\kappa,2} = 8.192 \cdot 10^3$ and $D_{\kappa,3} = 1.989 \cdot 10^8$, with $\gamma_{E,\kappa} = 2.428 \cdot 10^4$, for level 2. In Fig. 21 we present the normalized energies vs. the dimensionless time t. The overall decrease of the total and strain energies with respect to the initial solution $\rho_0 = \rho_V$ is 81.31% and 85.14%, respectively (the decrease of J and J_E at the continuation level 1 is 72.49% and 81.54%, while at level 2 it is 38.07% and 19.48%). The minimum value of J_E is obtained at the steady state of continuation level 2.

In Fig. 22(bottom) we present the steady state of the phase (material) variable obtained by solving the topology optimization problem starting from the initial solution ρ_0 depicted in Fig. 22(top); notice the "bubbles" of material distributed in correspondence of the peak values of the strain energy function ψ_E (see Fig. 19). This test is referred as Test 3.2. The volume fraction of this case is $V/|\Omega| = 0.4067$ due to the presence of the initial "bubbles"; also, we choose $\overline{\lambda} = 6.00$ and $\overline{\gamma} = 1.00$. The dimensionless parameters of Eq. (72) are $D_2 = 2.731 \cdot 10^3$ and $D_3 = 3.452 \cdot 10^7$ with $\gamma_E = 1.264 \cdot 10^4$. In Fig. 23 we present the behavior of the normalized energies with respect the dimensionless time t. The overall reductions of J and J_E at the steady state are 77.58% and 80.85%, respectively. The maximum reduction of J_E (82.03%) is obtained at $t = 1.818 \cdot 10^{-4}$; the corresponding solution is shown in Fig. 22 together with another significant topology obtained during the phase transition (at $t = 9.217 \cdot 10^{-5}$ the reduction of J_E is 81.74%, 4.650% smaller than at the steady state), which can be selected for further design and analysis investigation.

$t = 0$

$t = 9.217 \cdot 10^{-5}$

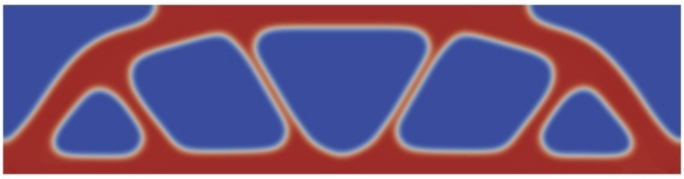

$t = 1.818 \cdot 10^{-4}$ (minimum J_E)

steady state

Figure 22: Test 3.2. Evolution of the phase (material density) variable ρ in time t with $\overline{\lambda} = 6.0$ and $\overline{\gamma} = 1.0$; prescribed initial solution ρ_0 with "bubbles" (top) and steady state (bottom).

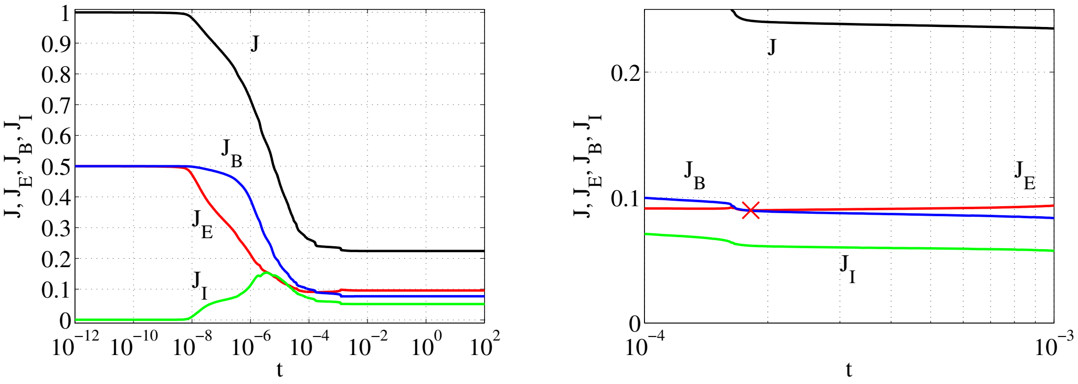

Figure 23: Test 3.2. Normalized energies J (black), J_E (red), J_B (blue) and J_I (green) vs. time t (left) and detail (right); the minimum value of J_E is indicated by an ×.

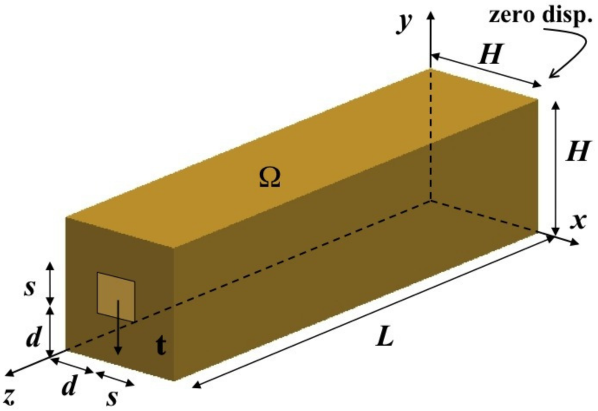

Figure 24: Test 4. Design domain Ω, surface force **h** and displacement constraints.

7.3 Three–dimensional problems

In this section, we solve topology optimization problems defined in three–dimensional design domains Ω.

7.3.1 Test 4

We consider the topology optimization problem represented in Fig. 24 in which the design domain Ω is a solid beam of size $H\times H\times L$, the surface force $\mathbf{h} = -\hbar_0\hat{\mathbf{y}}$ is applied on a subdomain of the front face and zero displacements are imposed on the back face (the plane $z = 0$). We assume $L = 4.00\,m$, $H = 1.00\,m$, $d = 0.375\,m$ and $s = 0.250\,m$; the volume fraction to be occupied by the material is set equal to $V/|\Omega| = 0.35$. By using symmetry properties, only half of the domain Ω (whose size is $H/2\times H\times L$) is considered for the computations. The design domain is represented by a B–splines basis of degree 2 composed of $10\times20\times80$ elements. To enforce the symmetry of the solution

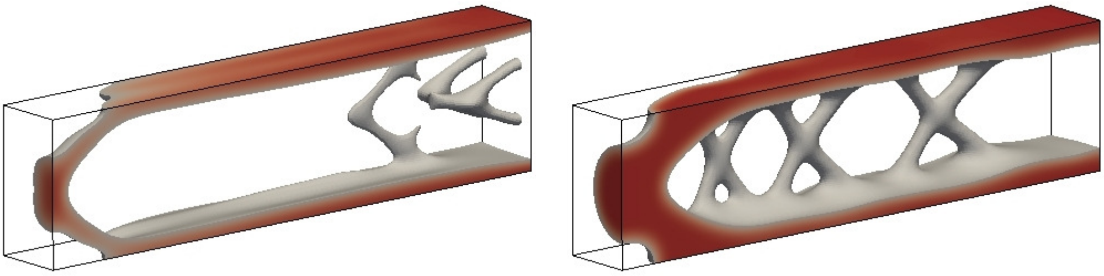

$t = 4.401 \cdot 10^{-5}$ $t = 2.577 \cdot 10^{-4}$

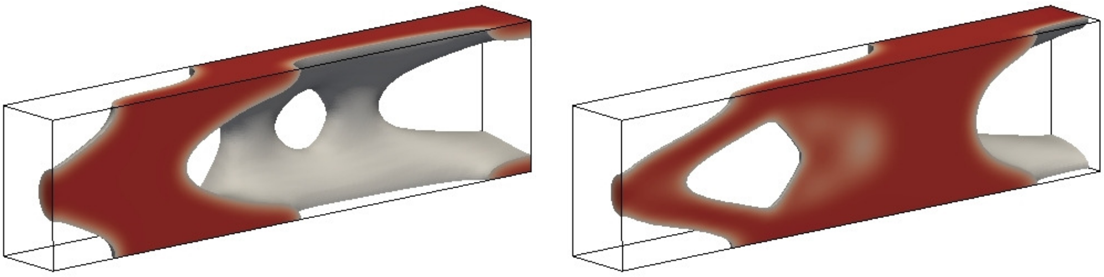

$t = 5.760 \cdot 10^{-3}$ (minimum J_E) $t = 1.940 \cdot 10^{-1}$

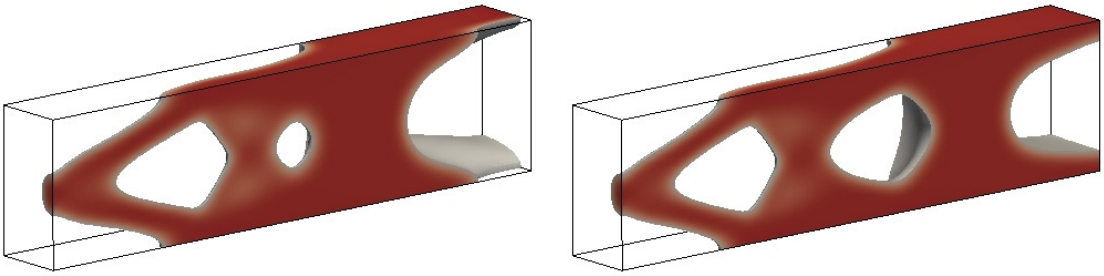

$t = 1.946 \cdot 10^{-1}$ steady state

Figure 25: Test 4.1. Evolution of the phase (material density) variable ρ in time t for mesh size $10 \times 20 \times 80$ with $\overline{\lambda} = 1.0$ and $\overline{\gamma} = 1.5$; the volume to be occupied by the material (for $\rho \geq 0.5$) is displayed; the color gray indicates $\rho = 0.5$.

with respect to the plane $y = H/2$ and prevent the detection of a nonsymmetric local minimum, we impose the same values of the phase variable on the planes $y = 0$ and $y = H$.

We solve the problem by considering $\overline{\lambda} = 1.0$ and $\overline{\gamma} = 1.5$ with the dimensionless size of the mesh $h = 0.05$ (Test 4.1); the computed parameter γ_E takes the value $\gamma_E = 2.040 \cdot 10^4$. The corresponding values of the dimensionless parameters are $D_2 = 4.000 \cdot 10^2$ and $D_3 = 1.224 \cdot 10^7$ with the characteristic time $T_0 = 4.000 \cdot 10^2$. In Fig. 25 we depict the phase variable ρ at significant time steps (dimensionless), including the steady state solution and the solution corresponding to the minimum value of J_E; the regions of the design domain Ω occupied by material, which are obtained for $\rho \geq 0.5$, are highlighted.

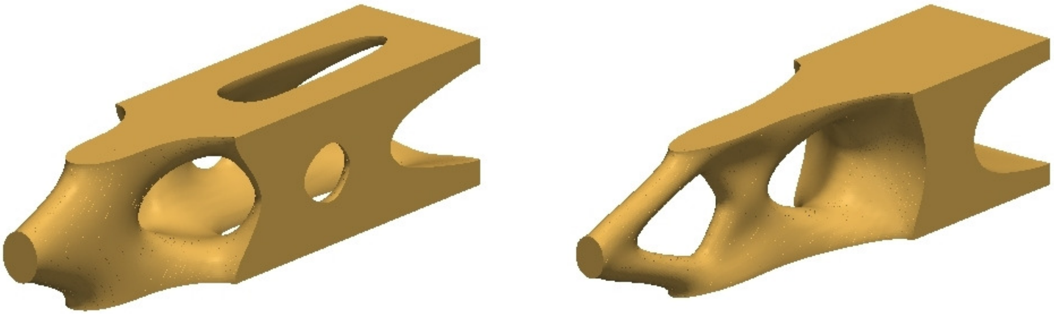

minimum J_E

steady state

Figure 26: Test 4.1. Optimal topologies corresponding to the minimum value of J_E (left) and to the steady state (right) obtained for $\overline{\lambda} = 1.0$ and $\overline{\gamma} = 1.5$.

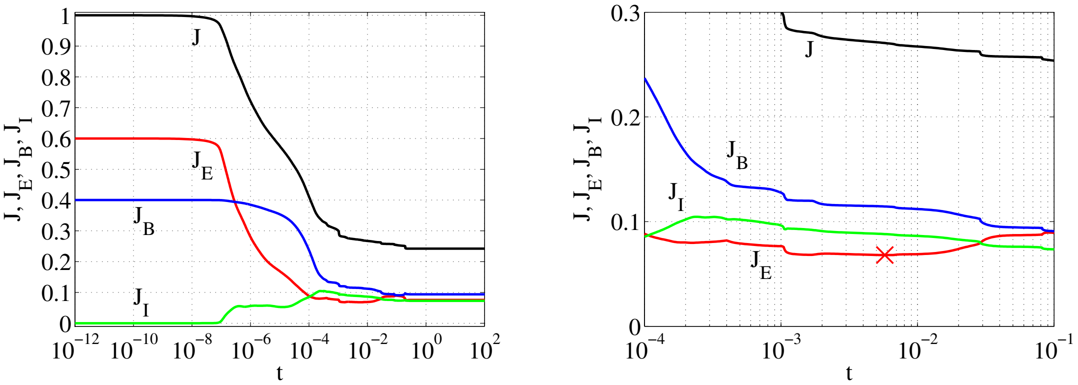

Figure 27: Test 4.1. Normalized energies J (black), J_E (red), J_B (blue) and J_I (green) vs. time t (left) and detail (right); the minimum value of J_E is indicated by an ×.

The capability of the method to handle hole nucleation is highlighted in Fig. 25 for the solutions at the time steps $t = 1.940 \cdot 10^{-1}$ and $t = 1.946 \cdot 10^{-1}$, in which a hole (specific volume of the design domain with $\rho < 0.5$) is generated. In Fig. 26(left) we show the optimal configuration for which the value of J_E is minimum; in Fig. 26(right) the configuration at the steady state is shown for comparison. The evolution of the objective functional J and the energies J_E, J_B and J_I vs. the dimensionless time are shown in Fig. 27(left); in Fig. 27(right) a detail around the minimum value of J_E is presented. At the steady state, the drops of the values of J and J_E with respect to the initial solution $\rho_0 = \rho_V$ are 75.78% and 87.38%, respectively. The minimum compliance is obtained at $t = 5.760 \cdot 10^{-3}$ with an 88.66% decrease; at its minimum, the value of J_E is 10.13% smaller than at the steady state. In general, all the topologies obtained in the range $t = 1.200 \cdot 10^{-3}$ – 10^{-2} could be eventually considered for further analysis and design investigation since the values of J_E are close to the minimum (less than 2.00% difference).

For comparison, we solve the same problem with different parameters $\overline{\lambda}$ and $\overline{\gamma}$.

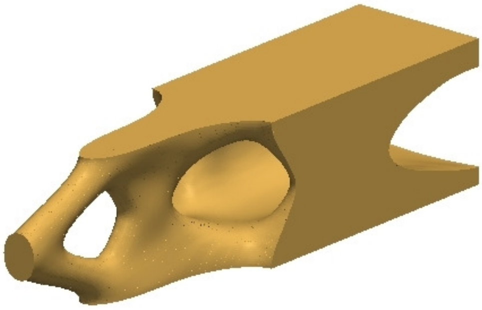

Figure 28: Test 4.2. Optimal topology corresponding to the minimum value of J_E for $\overline{\lambda} = 0.75$ and $\overline{\gamma} = 2.0$.

For this test, which we indicate as Test 4.2, we consider $\overline{\lambda} = 0.75$ and $\overline{\gamma} = 2.0$; the dimensionless parameters are $D_2 = 5.333 \cdot 10^2$ and $D_3 = 2.176 \cdot 10^7$. Due to the larger value of $\overline{\gamma}$ and the smaller value of $\overline{\lambda}$, we expect a more significant reduction of the strain energy J_E with slightly thinner interfaces. In Fig. 28 we present the optimal configuration corresponding to the minimum value of J_E, which is 14.16% less than the one obtained for Test 4.1.

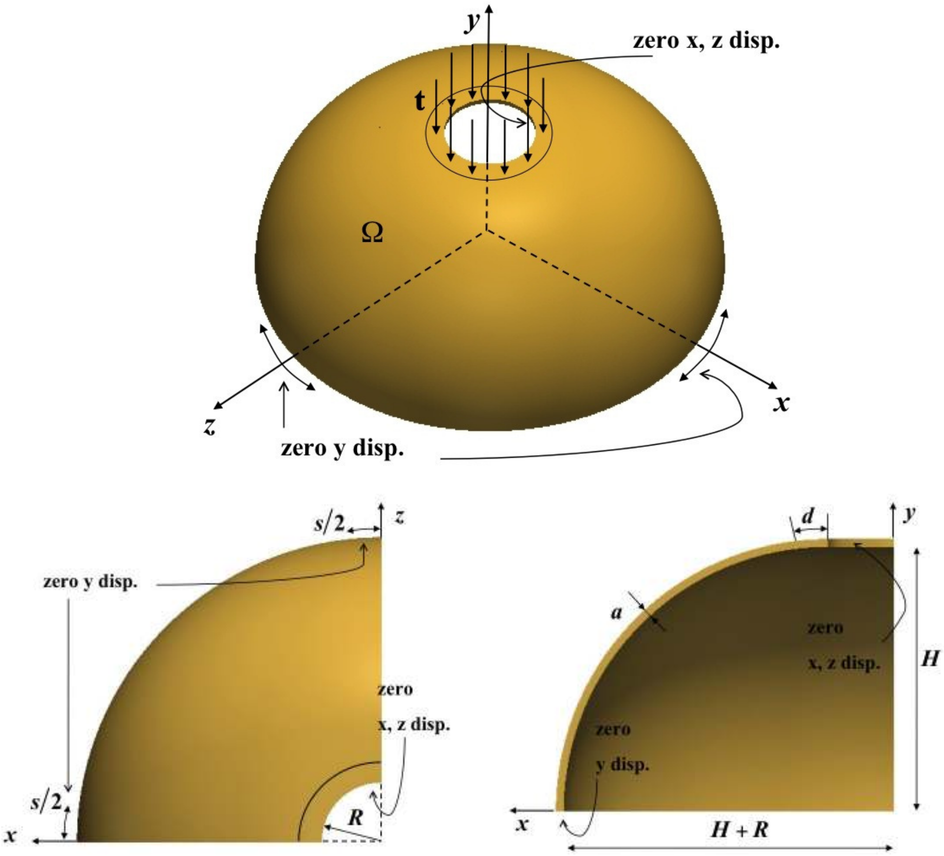

Figure 29: Test 5. Design domain Ω, surface force **h** and displacement constraints.

7.3.2 Test 5

This problem is defined in a design domain Ω represented by an hemispherical thin shell as shown in Fig. 29. The surface force $\mathbf{h} = -\hbar_0\hat{\mathbf{y}}$ and the displacement constraints are also shown. We assume $R = 0.250\,m$, $H = 1.00\,m$, $d = 0.0314\,m$ (arc length), $s = 0.200\,m$ (arc length) and thickness $a = 0.0200\,m$; the inner radius of the shell is constant and equal to H for all the planes through the axis $\hat{\mathbf{y}}$. The thin shell is described by a single NURBS patch with basis of degree $p = 2$ [80]; by virtue of the symmetry properties, only a quarter of the shell is considered as the domain for the computations. The volume fraction to be occupied by the material is $V/|\Omega| = 0.35$.

The shell is modelled as a three–dimensional linear elasticity problem. For the computations we consider a mesh composed of $128^2\times1$ elements. In this manner, since we consider a basis of degree $p = 2$, the bending modes are properly taken into account by the three–dimensional linear elastic model [13]; indeed, three control points exist through the thickness. An additional consequence of this choice is that the distribution of the phase variable ρ is constant throughout the thickness due to the conditions $\nabla\rho\cdot\hat{\mathbf{n}} = 0$ on the opposite faces. In order to enforce the symmetry of the solution in the quarter of the shell, we impose the same values of the phase variable at the $x = 0$ and $z = 0$ planes.

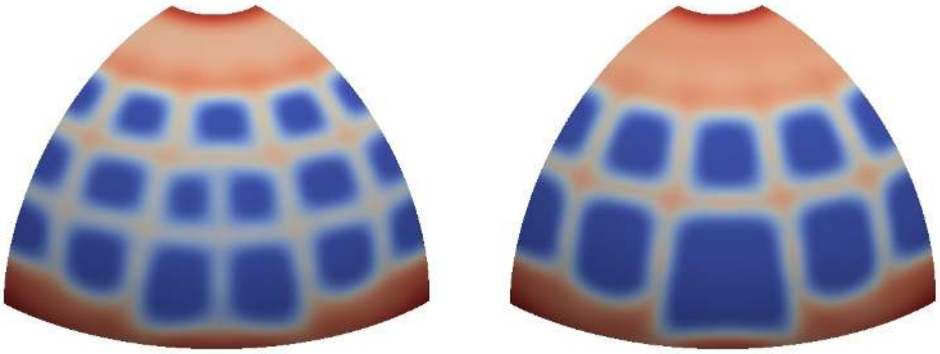

Level 1, $t = 2.445 \cdot 10^{-4}$ Level 1, steady state

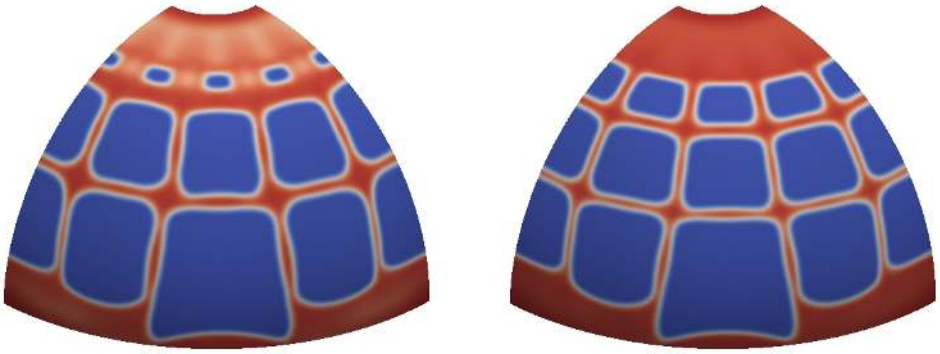

Level 2, $t = 1.596 \cdot 10^{-6}$ Level 2, steady state

Figure 30: Test 5. Evolution of the phase (material density) variable ρ in time t for mesh size $128^2 \times 1$ with the continuation method for $\mathbb{K} = \{5.0, 1.0\}$, $\overline{\lambda} = 1.0$ and $\overline{\gamma} = 2.5$; continuation levels 1 (top) and 2 (bottom) with steady states (right).

We solve the topology optimization problem by means of the continuation method with two levels; see Sec. 6.3. In particular, we assume $\kappa \in \mathbb{K} = \{5.0, 1.0\}$, $\overline{\lambda} = 1.0$ and $\overline{\gamma} = 2.5$; the dimensionless element size is chosen as $h = 0.01535$. The resulting dimensionless parameters are: $D_{\kappa,2} = 1.698 \cdot 10^2$, $D_{\kappa,3} = 9.770 \cdot 10^5$, $\gamma_{E,\kappa} = 4.604 \cdot 10^2$ for continuation level 1, and $D_{\kappa,2} = 4.244 \cdot 10^3$, $D_{\kappa,3} = 1.404 \cdot 10^7$, $\gamma_{E,\kappa} = 1.323 \cdot 10^3$ for level 2. In Fig. 30 we present the evolution of the material density in time throughout the two continuation levels. The final and optimal topology is the steady state of the second continuation level. In Fig. 31 we show the optimal configuration on the whole design domain obtained by placing the material where $\rho \geq 0.5$. In Fig. 32 we show the evolution of the objective functional J and the energies J_E, J_B and J_I vs. the dimensionless time for both continuation levels. Specifically, we obtain drops of 71.83% and 79.50% for J and J_E for level 1, and 27.17% and 28.83% for level 2, respectively. The overall decreases of J and J_E throughout the whole continuation level procedure are 79.48% and 85.41%, respectively; the minimum compliance is obtained at the steady state of continuation level 2.

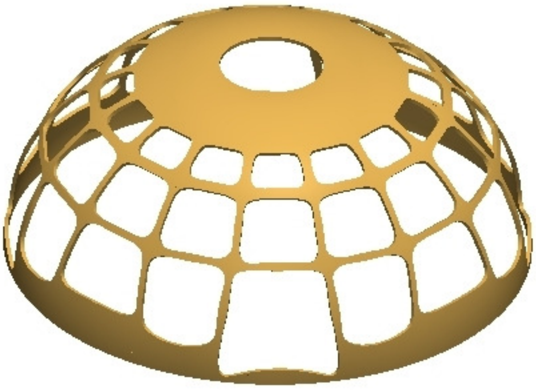

Figure 31: Test 5. Optimal topology obtained at the steady state of continuation level 2.

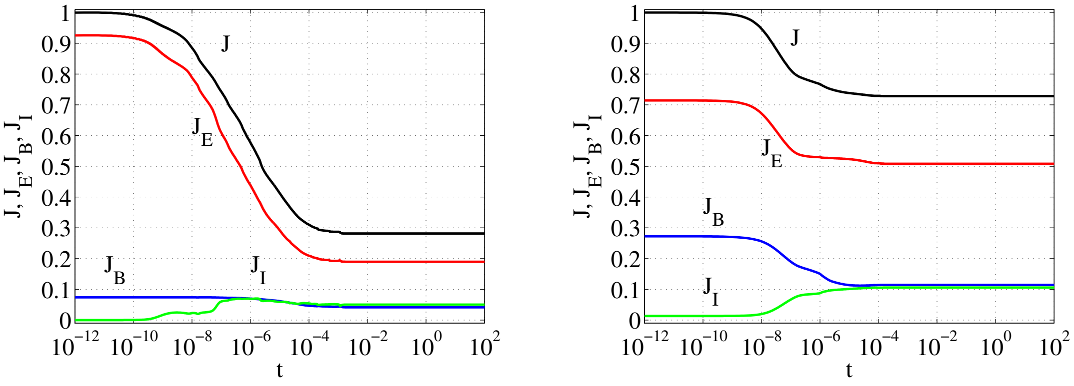

Level 1

Level 2

Figure 32: Test 5. Normalized energies J (black), J_E (red), J_B (blue) and J_I (green) vs. time t for the continuation method at levels 1 (left) and 2 (right).

8 Conclusions

In this work we solved minimum compliance topology optimization problems with a phase field model based on the generalized Cahn–Hilliard equation. With this approach, the interfaces between the phases, material and void, are represented by sharp, but smooth, layers and the optimal solution is obtained as the steady state of the phase transition problem, eliminating the need of an optimizer. The ability to deal with topological changes and hole nucleation is naturally embedded in the model as well as the constraint on the total amount of material to be distributed in the design domain. With this formulation, the topology optimization problem is completely defined at the continuous level and the optimal solution depends on dimensionless parameters specified by the user. Additionally, the mesh dependency effect, which typically affects the optimal topologies, can be eliminated by a suitable choice of the parameters controlling the thickness of the interfaces and the number of holes in the topology. The continuation method, a multilevel optimization strategy often used for the solution of the topology optimization problems, is extended to the phase field approach.

For the numerical approximation we used Isogeometric Analysis, which is particularly suitable for phase field problems and allows exact CAD geometry to be used to describe the design domain and to also be used in the optimization procedure. For the time approximation we used the generalized–α method in combination with a time–adaptive scheme which allowed to efficiently capture the fast and intermitted variations in time typically occuring in the phase field model.

We solved both two and three–dimensional problems to illustrate the validity of the approach, which we believe is a promising one for topology optimization problems.

Acknowledgements

L. Dedè and T.J.R. Hughes were partially supported by the Office of Naval Research under contract number N00014-08-0992. M.J. Borden and T.J.R. Hughes were partially supported by the Army Research Office under contract number W911NF-10-1-0216. M.J. Borden was partially supported by Sandia National Laboratories; Sandia is a multiprogram laboratory operated by Sandia Corporation, a Lockheed Martin Company, for the United States Department of Energy's National Nuclear Security Administration under contract DE-AC04-94AL85000.

The authors also acknowledge the Texas Advanced Computing Center (TACC) at The University of Texas at Austin for providing HPC resources that have contributed to the research results reported within this paper (URL: http://www.tacc.utexas.edu).

References

[1] N. Aage, T.H. Poulsen, A. Gersborg–Hansen and O. Sigmund, Topology optimization of large scale Stokes flow problems, *Struct. Multidisc. Optim.* **35** (2008), 175–180.

[2] R.A. Adams, Sobolev Spaces, Academic Press, New York, 1975.

[3] G. Allaire, F. de Gournay, F. Jouve and A.M. Toader, Structural optimization using topological and shape sensitivity via a level set method, *Control Cybern.* **34** (2005), 59–81.

[4] G. Allaire, F. Jouve and H. Maillot. Topology optimization for minimum stress design with the homogenization method, *Struct. Multidisc. Optim.* **28** (2004), 87–98.

[5] G. Allaire, F. Jouve and A. Toader, Structural optimization using sensitivity analysis and level set–method, *J. Comput. Phys.* **194** (2004), 363–393.

[6] S.M. Allen and J.W. Cahn, A microscopic theory for antiphase boundary motion and its application to antiphase domain coarsening, *Acta. Metall.* **27** (1979), 1085–1095.

[7] L. Ambrosio and G. Buttazzo, An optimal design problem with perimeter penalization, *Calc. Var. Partial Differential Equations* **1** (1993), 55–69.

[8] Y. Bazilevs, V.M. Calo, J.A. Cottrell, T.J.R. Hughes, A. Reali and G. Scovazzi, Variational multiscale residual–based turbulence modeling for large eddy simulation of incompressible flows, *Comput. Methods Appl. Mech. Engrg.* **197** (2007), 173–201.

[9] M.P. Bendsøe, On obtaining a solution to optimization problems for solid, elastic plates by restriction of the design space, *J. Struct. Mech.* **11** (1983), 501–521.

[10] M.P. Bendsøe and N. Kikuchi, Generating optimal topologies in structural design using a homogenization method. *Comput. Methods Appl. Mech. Engrg.* **71** (1988), 197–224.

[11] M.P. Bendsøe and O. Sigmund, Material interpolations schemes in topology optimization, *Arch. Appl. Mech.* **69** (1999), 635–654.

[12] M.P. Bendsøe and O. Sigmund, Topology Optimization: Theory, Methods and Applications, Springer–Verlag, Berlin, 2003.

[13] M. Bischoff, W.A. Wall, K.U. Bletzinger, E. Ramm, Models and finite elements for thin–walled structures, in: Encyclopedia of Computational Mechanics, E. Stein, R. de Borst, T.J.R. Hughes (Eds.), **2**, 59–137, *Solids Struct. Coupled Prob.* **3**, Wiley, 2004.

[14] K.U. Bletzinger and K. Maute, Towards generalized shape and topology optimization, *Eng. Optim.* **29** (1997), 201–216.

[15] K.U. Bletzinger and E. Ramm, Form finding of shells by structural optimization, *Engng. with Comp.* **9** (1993), 27–35.

[16] K.U. Bletzinger, R. Reitnger, S. Kimmich and E. Ramm, Shape optimization with program CARAT, in: Software Systems for Structural Optimization, H. Hörnlein and K. Schittkowski (Eds.), 97–124, *Internat. Ser. Numer. Math.* **110**, Birkhäuser, Basel, 1993.

[17] M.J. Borden, M.A. Scott, J.A. Evans and T.J.R. Hughes, Isogeometric finite element data structures based on Bézier extraction of NURBS, *Internat. J. Numer. Meth. Engng.* **87** (2011), 15–47.

[18] M.J. Borden, C.V. Verhoosel, M.A. Scott, T.J.R. Hughes and C. M. Landis, A phase–field description of dynamic brittle fracture, *ICES report* **11–14** (2011), submitted to *Comput. Methods Appl. Mech. Engrg.*

[19] B. Bourdin, Filters in topology optimization, *Internat. J. Numer. Methods Engng.* **50** (2001), 2143–2158.

[20] B. Bourdin and S. Chambolle, Design–dependent loads in topology optimization, *Contr. Optim. Calc. Var.* **9** (2003), 19–48.

[21] B. Bourdin and S. Chambolle, The phase field method in optimal design, in: IUTAM Symposium on Topological Design Optimization of Structures, M.P. Bendsøe, N. Olhoff and O. Sigmund (Eds.), 207–215, *Solid Mech. Appl.* **137**, Springer, Dordrecht, 2006.

[22] F. Brezzi and M. Fortin, Mixed and Hybrid Finite Element Methods, Springer–Verlag, New York, 1991.

[23] M. Burger and R. Stainko, Phase–field relaxation of topology optimization with local stress constraints, *SIAM J. Control. Optim.* **45** (2006), 1447–1466.

[24] L.A. Caffarelli and N.E. Muler, An L^∞ bound for solutions of the Cahn–Hilliard equation. *Arch. Rational Mech. Anal.* **133** (1995), 129-144.

[25] J.W. Cahn, On spinodal decomposition, *Acta Metall.* **9** (1961), 795–801.

[26] J.W. Cahn and J.E. Hilliard, Free energy of a non–uniform system. I. Interfacial free energy, *J. Chem. Phys.* **28** (1958), 258–267.

[27] J.W. Cahn and J.E. Hilliard, Free energy of a non–uniform system. III. Nucleation in a two–component incompressible fluid, *J. Chem. Phys.* **31** (1959), 688–699.

[28] W. Carter, J. Taylor and J. Cahn, Variational methods for microstructural–evolution theories, *J. Min. Metals Mater. Soc.* **49** (1997), 30–36.

[29] S. Cho and S.H. Ha, Isogeometric shape design optimization: exact geometry and enhanced sensitivity, *Struct. Multidisc. Optim.* **38** (2008), 53–70.

[30] J.S. Choi, T. Yamada, K. Izui, S. Nishiwaki and J. Yoo, Topology optimization using a reaction–diffusion equation, *Comput. Methods Appl. Mech. Engrg.* **200** (2011), 2407–2420.

[31] J. Chung and G.M. Hulbert, A time integration algorithm for structural dynamics with improved numerical dissipation: the generalized α–method, *J. Appl. Mech.* **60** (1993), 371–375.

[32] P. Ciarlet, The Finite Element Method for Elliptic Problems. NorthHolland, Amsterdam, 1978.

[33] J.A. Cottrell, T.J.R. Hughes and Y. Bazilevs, Isogeometric Analysis; Towards Integration of CAD and FEA, John Wiley & Sons, 2009.

[34] J.A. Cottrell, T.J.R. Hughes and A. Reali, Studies of refinement and continuity in isogeometric structural analysis, *Comput. Methods Appl. Mech. Engrg.* **196** (2007), 4160–4183.

[35] F. de Gournay, G. Allaire and F. Jouve, Shape and topology optimization of the robust compliance via the level set method, *Control Optim. Calc. Var.*~~~~**14** (2008), 43–70.

[36] P. Duysinx and M.P. Bendsøe, Topology optimization of continuum structures with local stress constraints, *Internat. J. Numer. Methods Engng.* **43** (1998), 1453–1478.

[37] C.M. Elliott, The Cahn–Hilliard model for the kinetics of phase separation, in: Mathematical Models for Phase Change Problems, J.F. Rodrigues (Eds.), 35–73, *Internat. Ser. Numer. Math.* **88**, Birkhäuser, Basel, 1989.

[38] C.M. Elliott and H. Garcke, On the Cahn–Hilliard equation with degenerate mobility, *SIAM J. Math. Anal.* **27** (1996), 404–423.

[39] J.A. Evans, Y. Bazilevs, I. Babuška and T.J.R. Hughes, n–widths, supinfs, and optimality ratios for the k–version of the isogeometric finite element method, *Comput. Methods Appl. Mech. Engrg.* **198** (2009), 1726–1741.

[40] P.C. Fife, Models for phase separation and their mathematics, *Electron. J. Diff. Eqns.* **48** (2000), 1–26.

[41] H.B. Frieboes, J.S. Lowengrub, S. Wise, X. Zheng, P. Macklin, E.L. Bearer and V. Cristini, Computer simulation of glioma growth and morphology, *NeuroImage* **37** (2007), 59–70.

[42] H. Garcke, On a Cahn–Hilliard model for phase separation with elastic misfit, *Ann. I. H. Poincaré – AN* **22** (2005), 165–185.

[43] H. Garcke and U. Weikard, Numerical approximation of the Cahn–Larché equation, *Numer. Math.* **100** (2005), 639–662.

[44] M.W. Gee, C.M. Siefert, J.J. Hu, R.S. Tuminaro and M.G. Sala, ML 5.0 smoothed aggregation user's guide, *Sandia National Laboratories* SAND2006–2649 (2006).

[45] A. Gersborg–Hansen, M.P. Bendsøe and O. Sigmund, Topology optimization of heat conduction problems using the finite volume method, *Struct. Multidisc. Optim.* **31** (2006), 251–259.

[46] H. Gomez, V.M. Calo, Y. Bazilevs and T.J.R. Hughes, Isogeometric analysis of the Cahn–Hilliard phase–field model, *Comput. Methods Appl. Mech. Engrg.* **197** (2008), 4333–4352.

[47] H. Gomez and T.J.R. Hughes, Provably unconditionally stable, second-order time accurate, mixed variational methods for phase-field models, *J. Comput. Phys.* **230** (2011), 5310–5327.

[48] H. Gomez, T.J.R. Hughes, X. Nogueira and V.M. Calo, Isogeometric analysis of the Navier–Stokes–Korteweg equations, *Comput. Methods Appl. Mech. Engrg.* **199** (2010), 1828–1840.

[49] J.K. Guest, Topology optimization with multiple phase projection, *Comput. Methods Appl. Mech. Engrg.* **199** (2009), 123–135.

[50] S.H. Ha, K.K. Choi and S. Cho, Numerical method for shape optimization using T–spline based isogeometric method, *Struct. Multidisc. Optim.* **42** (2010), 417–428.

[51] R.B. Haber, C.S. Jog and M.P. Bendsøe, A new approach to variable–topology shape design using a constraint on the perimeter, *Struct. Optim.* **11** (1996), 1–12.

[52] R.T. Haftka and R.V. Grandhi, Structural shape optimization – a survey, *Comput. Meth. Appl. Mech. Engrg.* **57** (1986), 91–106.

[53] M. Heroux, R. Bartlett, V.H.R. Hoekstra, J. Hu, T. Kolda, R. Lehoucq, K. Long, R. Pawlowski, E. Phipps, A. Salinger, H. Thornquist, R. Tuminaro, J. Willenbring and A. Williams, An overview of Trilinos, *Sandia National Laboratories* SAND2003–2927 (2003).

[54] T.J.R. Hughes, The Finite Element Method: Linear Static and Dynamic Finite Element Analysis, Dover Publications, Mineola, NY, 2000.

[55] T.J.R. Hughes, J.A. Cottrell and Y. Bazilevs, Isogeometric analysis: CAD, finite elements, NURBS, exact geometry and mesh refinement, *Comput. Methods Appl. Mech. Engrg.*, **194** (2005): 4135–4195.

[56] T.J.R. Hughes, A. Reali and G. Sangalli, Efficient quadrature for NURBS–based isogeometric analysis, *Comput. Methods Appl. Mech. Engrg.*,**199** (2010):301–313.

[57] K.E. Jansen, C.H. Whiting, G.M. Hulbert, A generalized–α method for integrating the filtered Navier–Stokes equations with a stabilized finite element method, *Comput. Methods Appl. Mech. Engrg.* **190** (2000), 305–319.

[58] J.S. Jensen and O. Sigmund, Topology optimization of photonic crystal structures: a high–bandwidth low–loss T–junction waveguide, *J. Opt. Soc. Am. B* **22** (2005), 1191–1198.

[59] C.S. Jog and R.B. Haber, Stability of finite element models for distributed–parameter optimization and topology design, *Comput. Methods Appl. Mech. Engrg.* **130** (1996), 203–226.

[60] R.V. Kohn and G. Strang, Optimal design and relaxation of variational problems. II, *Comm. Pure Appl. Math.* **39** (1986), 139–182.

[61] A.V. Kumar and A. Parthasarathy, Topology optimization using B–spline finite elements, *Struct. Multidisc. Optim.* (2011), DOI: 10.1007/s00158-011-0650-y.

[62] F.C. Larché and J.W. Cahn, Thermochemical equilibrium of multiphase solids under stress, *Acta Metall.* **26** (1978), 1579–1589.

[63] S. Lee, B.M. Kwak and I.Y. Kim, Smooth boundary topology optimization using B–spline and hole generation, *Internat. J. CAD/CAM* **7** (2007).

[64] R. Lipton, A saddle–point theorem with application to structural optimization, *J. Optim. Theory Appl.* **81** (1994), 549–568.

[65] K. Maute and E. Ramm, Adaptive topology optimization of shell structures, *AIAA J.* **35** (1997), 1767–1773.

[66] C. Miehe, F. Welschinger and M. Hofacker, Thermodynamically consistent phase–field models of fracture: variational principles and multi–field FE implementations, *Internat. J. Numer. Methods Engng.* **83** (2010), 1273–1311.

[67] H. Mlejnek and R. Schirrmacher, An engineering approach to optimal material distribution and shape finding, *Comput. Methods Appl. Mech. Engrg.* **106** (1993), 1–26.

[68] L. Modica and S. Mortola. Un esempio di Γ^{-}–convergenza, *Boll. Un. Mat. Ital. B (5)*, **14** (1977), 285–299.

[69] B. Mohammadi and O. Pironneau, Applied Shape Optimzation for Fuilds, Oxford University Press, Oxford, 2010.

[70] A.P. Nagy, M.M. Abdalla and Z. Gürdal, Isogeometric sizing and shape optimisation of beam structures, *Comput. Methods Appl. Mech. Engrg.* **199** (2010), 1216–1230.

[71] J.A. Norato, M.P. Bendsøe, R.B. Haber and D.A. Tortorelli, A topological derivative method for topology optimization, *Struct. Multidisc. Optim.* **33** (2007), 375–386.

[72] J.T. Oden, A. Hawkins and S. Prudhomme, General diffuse–interface theories and an approach to predictive tumor growth modeling, *Math. Models Methods Appl. Sci.* **20** (2010), 477–517.

[73] A. Onuki, Ginzburg–Landau approach to elastic effects in the phase separation of solids, *J. Phys. Soc. Jpn.* **58** (1989), 965–985.

[74] S. Osher and J.A. Sethian, Front propagating with curvature dependent speed: algorithms based on Hamilton–Jacobi formulations, *J. Comp. Phys.* **78** (1988), 12–49.

[75] J. París, F. Navarrina, I. Colominas and M. Casteleiro, Topology optimization of structures with local and global stress constraints, *Struct. Multidisc. Optim.* **39** (2009), 419–437.

[76] K.S. Park and S.K. Youn, Topology optimization of shell structures using adaptive inner–front (AIF) level set method, *Struct. Multidisc. Optim.* **36** (2008), 43–58.

[77] N.L. Pedersen, Topology optimization of laminated plates with prestress, *Comput. Struct.* **80** (2002), 559–570.

[78] J. Petersson, Some convergence results in perimeter–controlled topology optimization, *Comput. Methods Appl. Mech. Engrg.* **171** (1999), 123–140.

[79] J. Petersson and O. Sigmund, Slope constrained topology optimization, *Internat. J. Numer. Methods Engng.* **41** (1998), 1417–1434.

[80] L. Piegl and W. Tiller, The NURBS Book, Springer–Verlag, New York, 1997.

[81] T.A. Poulsen, A new scheme for imposing a minimum length scale on topology optimization, *Internat. J. Numer. Methods Engng.* **57** (2003), 741–760.

[82] A. Quarteroni, R. Sacco and F. Saleri, Numerical Mathematics, Springer–Verlag, Berlin, 2007.

[83] A. Quarteroni and A. Valli, Numerical Approximation of Partial Differential Equations,. Springer–Verlag, Berlin and Heidelberg, 1994.

[84] E. Ramm, K. Maute and S. Schwarz, Adaptive topology and shape optimization, in: Computational Mechanics, New Trends and Applications, S. Idelsohn, E. Oñate and E. Dvorkin (Eds.), CIMNE, Barcelona, 1998.

[85] P. Rybka and K.H. Hoffmann, Convergence of solutions to Cahn–Hilliard equation, *Comm. Part. Diff. Eq.* **24** (1999), 1055–1077.

[86] G.I.N. Rozvany, Aims, scope, methods, history and unified terminology of computer aided topology optimization in structural mechanics, *Struct. Multidiscip. Optim.* **21** (2001), 90–108.

[87] G.I.N. Rozvany and T. Birker, On singular topologies in exact layout optimization, *Struct. Optim.* **8** (1994), 228–235.

[88] S. Schwarz, K. Maute and E. Ramm, Topology and shape optimization for elastoplastic structural response, *Comput. Methods Appl. Mech. engrg.* **190** (2001), 2135–2155.

[89] T.W. Sederberg, J.M. Zhengs, J.M. Bakenov and A. Nasri, T–splines and T–NURCCSs, *ACM Trans. Graph.* **22** (2003), 477–484.

[90] Y.D. Seo, H.J. Kim and S.K. Youn, Isogeometric topology optimization using trimmed spline surfaces, *Comput. Methods Appl. Mech. Engrg.* (2010), in press.

[91] Y.D. Seo, H.J. Kim and S.K. Youn, Shape optimization and its extension to topological design based on isogeometric analysis, *Internat. J. Solids Struct.* **47** (2010), 1618–1640.

[92] O. Sigmund, Design of multiphysics actuators using topology optimization – Part I: one–material structures, *Comput. Methods Appl. Mech. Engrg.* **190** (2001), 6577–6604.

[93] O. Sigmund, Morphology–based black and white filters for topology optimization, *Struct. Multidiscip. Optim.* **61** (2004), 238–254.

[94] O. Sigmund, On the design of compliant mechanisms using topology optimization, *Mech. Struct. Machines* **25** (1997), 493–524.

[95] O. Sigmund and J. Petersson, Numerical instabilities in topology optimization: a survey on procedures dealing with checkerboards, mesh–dependencies and local minima, *Struct. Optim.* **16** (1998), 68–75.

[96] J. Sokolowski and J.P. Zolésio, Introduction to Shape Optimization: Shape Sensitivity Analysis, Springer–Verlag, Berlin, 2003.

[97] R. Spatschek, C. Müller–Gugenberger, E. Brener and B. Nestler, Phase field modeling of fracture and stress–induced phase transitions, *Phys. Rev. E* **75** (2007).

[98] M. Stolpe and K. Svanberg, Modeling topology optimization problems as linear mixed 0–1 programs, *Internat. J. Numer. Methods Engng.* **57** (2003), 723–739.

[99] M. Stolpe and K. Svanberg, On the trajectories of penalization methods for topology optimization, *Struct. Multidisc. Optim.* **21** (2001), 128–139.

[100] K. Svanberg, A class of globally convergent optimization methods based on conservative convex separable approximations, *SIAM J. Optim.* **12** (2002), 555–573.

[101] K. Svanberg, The method of moving asymptotes – a new method for structural optimization. *Internat. J. Numer. Methods Engng.* **24** (1987), 359–373.

[102] A. Takezawa, S. Nishiwaki and M. Kitamura, Shape and topology optimization based on the phase field method and sensitivity analysis, *J. Comput. Phys.* **229** (2010), 2697–2718.

[103] K.G. van der Zee, J.T. Oden, S. Prudhomme and A.J. Hawkins, Goal–oriented error estimation for Cahn–Hilliard models of binary phase transition, *Numer. Methods Partial Diff. Eq.* **27** (2011), 160–196.

[104] L.A. Vese and T.F. Chan, A multiphase level set framework for image segmentation using the Mumford and Shah model, *Internat. J. Comput. Vis.* **50** (2002), 271–293.

[105] W.A. Wall, M.A. Frenzel and C. Cyron, Isogeometric structural shape optimization, *Comput. Methods Appl. Mech. Engrg.* **197** (2008), 2976–2988.

[106] M.Y. Wang, X. Wang and D. Guo, A level set method for structural topology optimization, *Comput. Methods Appl. Mech. Engrg.* **192** (2003), 227–246.

[107] M.Y. Wang and S. Zhou, Phase field: a variational method for structural topology optimization, *Comput. Model. Eng. Sci.* **6** (2004), 227–246.

[108] D. Wang, W.H. Zhang and J.S. Jiang, Combined shape and sizing optimization of truss structures, *Comput. Mech.* **29** (2002), 307–312.

[109] D. Weiss, Feature–based spline optimization in CAD; a step towards geometry-based structure creation, *Struct. Multidisc. Optim.* **42** (2010), 619–631

[110] W. Wu, D.Z. Yang, Y.Y. Huang, M. Qi, W.Q. Wang, Topology optimization of a novel stent platform with drug reservoirs, *Med. Eng. Phys.* **30** (2008), 1177–1185.

[111] Y.M. Xie and G.P. Steven, Evolutionary Structural Optimization, Springer–Verlag, London, 1997.

[112] T. Yamada, K. Izui, S. Nishiwaki and A. Takezawa, A topology optimization method based on the level set method incorporating a fictitious interface energy, *Comput. Methods Appl. Mech. Engrg.* **199** (2010), 2876–2891.

[113] V. Young, O.M. Querin, G.P. Steven and Y.M. Xie, 3D and multiple load case bi–directional evolutionary optimization (BESO), *Struct. Optim.* **18** (1999), 183–192.

[114] S. Zhou and M.Y. Wang, Multimaterial structural topology optimization with a generalized Cahn–Hilliard model of multiphase transition, *Struct. Multidisc. Optim.* **33** (2007), 89–111.

[115] S. Zhou and M.Y. Wang, 3D Multi–material structural topology optimization with the generalized Cahn–Hilliard equations, *Comput. Model. Eng. Sci.* **16** (2006), 69–82.